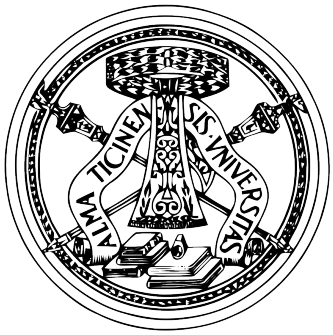

UNIVERSITÀ DEGLI STUDI DI PAVIA

DIPARTIMENTO DI FISICA A. VOLTA

CORSO DI LAUREA MAGISTRALE IN SCIENZE FISICHE

In-Beam PET-based validation of an analytical approach to predict 3D positron emitter distribution in carbon ion therapy

Tesi di laurea magistrale di:

Giulia Vallari

Matr. n. 544151

Relatore:

Prof.ssa Francesca Ballarini

Co-relatori:

Prof.ssa Katia Parodi

Dott. Tianxue Du

Anno Accademico 2024/2025

Master's Thesis

In-Beam PET-based validation of an analytical approach to predict 3D positron emitter distribution in carbon ion therapy

Faculty of Physics
Ludwig-Maximilians-Universität München

Giulia Vallari

Submitted in partial fulfillment of the requirements for the degree of M. Sc.
Supervised by Prof. Dr. Katia Parodi and Dr. Tianxue Du

Contents

List of Figures

List of Tables

List of Acronyms

1D one-dimensional.

2D two-dimensional.

3D three-dimensional.

AS axial-shift.

BGO Bismuth Germanate.

CIRT Carbon ion radiation theraphy.

CT computed tomography.

DAQ data acquisition.

DOI depth-of-interaction.

DROP dual-ring OpenPET.

DSBs double-strand breaks.

EC Electron capture.

FBP Filtered Back Projection.

FOV field of view.

FWHM full width at half maximum.

GOSZ Zr-doped gadolinium oxorthosilicate.

HIMAC Heavy Ion Medical Accelerator.

IARC Agency for Research on Cancer.

IC Internal conversion.

IDD laterally integrated depth-dose.

IDPED Laterally integrated depth positron emitter distribution.

IGRT image-guided radiotherapy.

IMRT intensity-modulated radiotherapy.

IR Ionizing radiation.

LBNL Lawrence Berkeley National Laboratory.

LET linear energy transfer.

LM-MLEM List-Mode Maximum Likelihood Expectation Maximization.

LMU Ludwig-Maximilians-Universität München.

LOR line of response.

LSO Lutetium Oxyorthosilicate.

MC Monte Carlo.

MCNP Monte Carlo N-Particle.

MIP minimum ionizing particle.

NIRS National Institute of Radiological Sciences.

NRMSE normalized root mean square error.

OER oxygen enhancement ratio.

OSEM Ordered Subsets Expectation Maximization.

PBA pencil beam algorithm.

PE positron emitter.

PED positron emitter distribution.

PET positron emission tomography.

PMMA Polymethyl Methacrylate.

PMT photomultiplier tube.

PTCOG Particle Therapy Co-Operative Group.

QGSP_BIC Quark-Gluon String Precompound with Binary Cascade for light ions.

QST National Institutes for Quantum Science and Technology.

RBE relative biological effectiveness.

ROS reactive oxygen species.

SE slant-ellipsoid.

SOBP spread-out Bragg peak.

SPR stopping power ratio.

SROP single-ring OpenPET.

SSBs single-strand breaks.

TOF Time-of-Flight.

Abstract

Cancer is one of the greatest health, social, and economic challenges of the 21st century. In 2022, there were about 20 million new cases and 9.7 million deaths, with lung, breast, colorectal, prostate, and stomach cancers most prevalent. The incidence of cancer is expected to increase by 77% between 2022 and 2050, underscoring the urgent need for effective, precise, and accessible therapeutic strategies.

Among conventional cancer treatments, radiotherapy plays a central role, being used in over half of patients for curative or palliative purposes, either alone or in combination with other therapies. Besides photon-based radiotherapy, particle therapies such as proton and carbon ion radiotherapy (CIRT) have emerged as promising alternatives due to their superior dose localization and potential biological advantages.

A critical aspect of particle therapy is range verification, which is essential to ensure a proper dose delivery. CIRT may benefit from such verification due to its sensitivity to range uncertainties. Positron emission tomography (PET) is commonly employed for *in-vivo* range verification by exploiting the distribution of positron emitters generated during irradiation. However, because the PET signal is not directly proportional to the delivered dose, the measured activity cannot be directly compared with dose distribution. Instead, predicted positron emitter distributions (PED) are required, and treatment verification is achieved by comparing them with the measured signal. Monte Carlo (MC) simulations are typically employed for PED prediction, providing high accuracy but at the cost of substantial computational time. To overcome these challenges, alternative analytical approaches have been proposed, offering a significant reduction in computation time without compromising reliability.

This thesis work aims to validate a novel analytical framework, developed at Ludwig-Maximilians-Universität München, for predicting three-dimensional PED in CIRT, offering a computationally efficient alternative to MC simulations. Validation was performed

in two stages: first, by comparing analytical predictions with MC simulations for a ^{12}C-ion pencil beam in a PMMA phantom; second, by converting the analytical PED into an activity distribution for direct comparison with in-beam PET measurements provided by the National Institutes for Quantum and Radiological Science and Technology in Japan.
The thesis begins with an introduction outlining its objectives and relevance, followed by a review of key concepts in radiation interaction, CIRT, PET imaging, and MC simulations. Afterwards, it presents the analytical framework for PED and activity prediction and it reports the validation results, and finally it concludes with a discussion of the main findings and future perspectives.
The results demonstrate that the proposed analytical method provides accurate PED predictions with substantially reduced computation times, supporting its potential integration into treatment planning systems. This work contributes to advancing range verification strategies in CIRT, thereby promoting greater treatment precision and improving patient outcomes in next-generation radiotherapy.

Abstract

Il cancro rappresenta una delle maggiori sfide sanitarie, sociali ed economiche del XXI secolo. Nel 2022 sono stati registrati circa 20 milioni di nuovi casi e 9,7 milioni di decessi, con i tumori più diffusi che riguardano polmoni, seno, colon-retto, prostata e stomaco. Si prevede che l'incidenza del cancro aumenterà del 77% tra il 2022 e il 2050, evidenziando l'urgente necessità di strategie terapeutiche efficaci, precise e accessibili.

Tra i trattamenti convenzionali, la radioterapia riveste un ruolo centrale, essendo impiegata in oltre la metà dei pazienti a scopo curativo o palliativo, sia da sola sia in combinazione con altre terapie. Oltre alla radioterapia basata su fotoni, le terapie con particelle, come la radioterapia con protoni e ioni di carbonio (CIRT), si sono affermate come alternative promettenti grazie alla loro superiore capacità di localizzazione della dose e ai potenziali vantaggi biologici.

Un aspetto cruciale della terapia con particelle è la verifica della profondità di penetrazione (*range verification*), fondamentale per garantire una corretta somministrazione della dose. La CIRT può trarre beneficio da questa verifica, data la sua sensibilità alle incertezze nel range. La tomografia a emissione di positroni (PET) è comunemente utilizzata per la verifica *in-vivo* sfruttando la distribuzione degli emettitori di positroni generati durante l'irradiazione. Tuttavia, poiché il segnale PET non è direttamente proporzionale alla dose somministrata, l'attività misurata non può essere confrontata direttamente con la distribuzione della dose. È quindi necessario prevedere la distribuzione degli emettitori di positroni (PED) e confrontarla con il segnale misurato per la verifica del trattamento. Le simulazioni Monte Carlo (MC) sono generalmente utilizzate per la previsione della PED, garantendo alta accuratezza ma con tempi computazionali rilevanti. Per superare questi limiti sono stati proposti approcci analitici alternativi, che riducono significativamente i tempi di calcolo senza compromettere l'affidabilità.

Questo lavoro di tesi si propone di validare un nuovo framework analitico, sviluppato presso

la Ludwig-Maximilians-Universität München, per la previsione tridimensionale della PED nella CIRT, offrendo un'alternativa computazionalmente efficiente alle simulazioni MC. La validazione è stata condotta in due fasi: prima, confrontando le previsioni analitiche con le simulazioni MC per un fascio a matita (*pencil beam*) di ioni ^{12}C in un fantoccio di PMMA; successivamente, convertendo la PED analitica in una distribuzione di attività per un confronto diretto con le misure PET *in-beam* fornite dal National Institutes for Quantum and Radiological Science and Technology, in Giappone.

La tesi inizia con un'introduzione agli obiettivi e alla rilevanza dello studio, seguita da una revisione dei concetti chiave sull'interazione delle radiazioni, sulla CIRT, sull'imaging PET e sulle simulazioni MC. Successivamente viene presentato il framework analitico per la previsione della PED e dell'attività, vengono riportati i risultati della validazione e, concluse le osservazioni, si riporta una discussione delle prospettive future.

I risultati mostrano che il metodo analitico proposto consente previsioni accurate della PED con tempi di calcolo significativamente ridotti, supportandone l'integrazione nei piani di trattamento. Questo lavoro contribuisce a migliorare le strategie di *range verification* nella CIRT, favorendo una maggiore precisione terapeutica e migliorando gli esiti clinici nella radioterapia di nuova generazione.

1

Introduction

Cancer represents one of the greatest health, social, and economic challenges of the 21st century. According to the most recent estimates from the GLOBOCAN project of the International Agency for Research on Cancer (IARC), in 2022 there were approximately 20 million new cancer cases and 9.7 million cancer deaths worldwide. Cancer is also among the leading causes of premature mortality in individuals aged 30 to 69 years, and it remains a major barrier to increasing global life expectancy. Beyond its direct impact on health, the disease carries profound societal and economic consequences, which vary considerably across cancer types, geographic regions, and between genders [1].

The global burden of cancer is not evenly distributed across regions. Nearly half of all cases and over half of all deaths occur in Asia, where around 60% of the world's population lives. Africa and Asia face especially high mortality relative to incidence, partly due to late-stage diagnoses. Europe, despite having less than 10% of the global population, accounts for over one-fifth of cases and deaths, highlighting a substantial burden in high-income regions [1].

Current estimates indicate that about one in five people will develop cancer during their lifetime, while approximately one in nine men and one in twelve women will die from it. The ten most common cancer types alone account for more than 60% of all new cases and deaths. Lung cancer is the most frequently diagnosed cancer worldwide and the leading cause of cancer-related mortality, followed by breast, colorectal, prostate, and stomach cancers. Marked gender differences also emerge: in women, breast cancer is both the most common and the leading cause of cancer death, followed by lung and colorectal cancers. In men, lung cancer ranks first for both incidence and mortality, while prostate and colorectal cancers are among the most frequently diagnosed, and liver and colorectal cancers among

the leading causes of death [1].

Looking forward, demographic trends suggest that the global cancer burden will grow significantly in the coming decades. Based on projections of population growth and aging, assuming overall cancer rates remain unchanged, it is estimated that by 2050 there will be over 35 million new cancer cases worldwide, representing a 77% increase compared to 2022. This rise will be driven largely by the ongoing demographic transition, with the global population expected to increase from approximately 8 billion in 2022 to 9.7 billion by 2050 [1].

This growing burden underscores the critical importance of effective treatments and equitable access to care, as timely and appropriate therapy can significantly improve patient outcomes and reduce the societal impact of cancer.

Cancer therapy has undergone remarkable advances in recent decades, yet clinical practice continues to rely on a few core treatment modalities. The main approaches are surgery, chemotherapy, hormone-based systemic therapies and radiotherapy, often used alone or in multimodal combinations depending on tumor type, stage, and patient condition [2].

Among these strategies, radiotherapy plays a pivotal role, being employed in more than half of all cancer patients during the course of their disease, either with curative or palliative intent [3]. Its therapeutic effect relies on the ability of ionizing radiation to induce lethal damage in tumor cells while preserving surrounding healthy tissues. At cellular level, this occurs through two main mechanisms: direct ionization of the DNA molecule and indirect effects. Both pathways lead to complex DNA lesions, particularly double-strand breaks, which, if irreparably damaged, compromise genomic integrity and result in cell death [4]. By combining effective local tumor control with the possibility of organ preservation, radiotherapy has become an indispensable component of multidisciplinary cancer care [2].

Conventional radiotherapy relies mainly on X-rays to deliver ionizing radiation to tumors. Over the years, technological progress has greatly improved the precision of photon-based techniques, from two-dimensional approaches to advanced modalities such as intensity-modulated radiotherapy (IMRT) and image-guided radiotherapy (IGRT). These methods allow dose escalation to the tumor while sparing surrounding healthy tissue. Nevertheless, photons deposit energy along their entire path through the body, which can result in

significant dose exposure to normal tissues and associated side effects [2, 3].

To overcome the limitations of photon therapy, particle-based treatments have been developed. Proton therapy exploits the physical advantage of the Bragg peak, a sharp increase in energy deposition at the end of the particle's range. This allows a more localized delivery of the therapeutic dose, reducing exposure to surrounding organs. Proton therapy has been successfully applied to pediatric tumors, tumors of the central nervous system, and other cases where sparing normal tissues is of particular importance [3].

Carbon ion radiation theraphy (CIRT) represents another type of particle therapy, combining both physical and biological benefits. Like protons, carbon ions exhibit a pronounced Bragg peak that enables precise dose localization. In addition, they possess a higher linear energy transfer (LET) and a greater relative biological effectiveness (RBE) compared to protons, leading to enhanced tumor cell killing, particularly in radioresistant tumors such as sarcomas, head and neck tumors, and certain central nervous system tumors. These biological properties also reduce the dependence of CIRT efficacy on tumor oxygenation and cell cycle phase, factors that often reduce the effectiveness of photon and proton treatments [3, 5].

Despite these advantages, the clinical implementation of CIRT remains limited. The technology requires highly specialized facilities, large particle accelerators, and substantial financial investment, which has confined its availability to a relatively limited number of centers worldwide. Moreover, long-term clinical data are still relatively scarce compared to those available for photons and protons. For this reason, ongoing research is focusing not only on accumulating clinical evidence but also on enhancing treatment efficacy [5].

Photon-based radiotherapy remains the global standard, but proton and carbon ion therapies represent promising frontiers for achieving greater tumor control with reduced side effects. The unique properties of carbon ions, in particular, highlight their potential to address clinical challenges in radioresistant and complex tumors [5].

A critical requirement for the clinical success of particle therapy is the range verification. Accurate determination of the ion range is essential to fully exploit the precision of these modalities, as uncertainties can compromise dose delivery to tumors and increase the risk of unnecessary dose to surrounding healthy tissues. Such uncertainties may arise from patient positioning errors, anatomical changes during treatment, variations in tissue

density, and limitations in treatment planning imaging [6, 7].

Several approaches have been developed for range verification, including prompt gamma detection and positron emission tomography (PET). PET-based methods allow non-invasive *in-vivo* measurement of the distribution of positron emitters (PEs) generated during irradiation, thereby enabling indirect assessment of the particle range. Offline (measurement after irradiation in adjacent PET imaging rooms), in-room (measurement after irradiation in the treatment room) and in-beam (measurement during or immediately after irradiation) PET approaches have been investigated, each offering specific advantages and challenges. Together, they represent a key focus of current research aimed at developing reliable, real-time range verification techniques for CIRT [8].

However, the electromagnetic processes underlying the dose distribution differ fundamentally from the nuclear mechanisms in positron emissions. As a result, the measured PET activity cannot be directly compared to the dose distribution [9].

The PET-based range verification entails a comparison of the measured positron emissions with predicted PET images which can be obtained through two main computational strategies. Monte Carlo (MC) simulations provide a physics-based and detailed description of particle interactions and PEs production, enabling precise prediction of the expected PET activity. However, their high computational cost still limits their applicability for real-time range verification. Analytical methods, on the other hand, offer a faster and more computationally efficient alternative by describing the underlying processes through mathematical models, while maintaining a satisfactory level of accuracy.

The aim of this thesis work is to validate, using in-beam PET data, a novel analytical framework which predicts the three-dimensional (3D) positron emitter distribution (PED) in CIRT, developed at Ludwig-Maximilians-Universität München (LMU) and proposed in [10]. This framework extends a previous one-dimensional (1D) approach [11], later improved by incorporating additional PE channels and refined modeling functions, and expanded into a full three-dimensional model by a pencil beam algorithm (PBA).

The validation is conducted in two stages. First, the analytical PED predictions are compared with those obtained from MC simulations using the Geant4 toolkit for a ^{12}C-ion pencil beam with an initial nominal energy of 200 MeV/n in a PMMA phantom. Second, a computational procedure is introduced to convert the analytical PED into an activity

distribution, enabling direct comparison with experimental PET data. These data were acquired at the National Institutes for Quantum Science and Technology (QST) in Chiba, Japan, using their in-beam OpenPET system. In the experiments, a PMMA phantom was irradiated by ^{12}C-ion beams with an initial nominal energy of 255.7 MeV/n, and the measurement was performed immediately after irradiation. Three beam configurations were considered, each delivering doses of 1.5 Gy and 3 Gy: a single spot, and 2×2 cm^2 and 4×4 cm^2 irradiation fields. For each configuration, the signal was reconstructed for three time frames after the end of irradiation: 0-60 s, 0-600 s, and 300-600 s.

In this manuscript chapter 1 is this introduction, outlining the objectives, scope, and relevance of the work in the context of CIRT and PET-based range verification.
Chapter 2 introduces the fundamental concepts underlying this work. It covers the interaction of ionizing radiation with matter, radioactive decays, and the principles of CIRT, including physical, biological, and facility aspects. The chapter also presents the main aspects of PET, focusing on system parameters, image reconstruction, range verification in CIRT, and the OpenPET system, and it concludes with an overview of MC methods for PED and activity prediction.
Chapter 3 provides a detailed description of the analytical framework for three-dimensional PED prediction. It covers database generation with MC simulations, determination of PEs, lateral and longitudinal modeling, ray casting, and the calculation of full 3D PED. Particular attention is given to the methodological development of the activity prediction process. This includes a detailed presentation of the method for converting PED into activity distributions, covering its formulation, implementation, and culminating in a thorough comparison between predicted and experimental PET data.
Chapter 4 presents the outcomes of the validation process, including comparisons between analytical predictions and experimental PET measurements.
Chapter 5 summarizes the main findings, discusses their implications for CIRT verification, and outlines perspectives for future developments.

2

Theoretical background

In this chapter, the main physical concepts, quantities, and processes relevant to this thesis work are presented. Section (2.1) provides an overview of the interactions between radiation and matter, with focus on heavy charged particles and their dose deposition. Section (2.2) outlines the key features of radioactivity, while Sections (2.3) and (2.4) describe in detail Carbon ion radiation theraphy and positron emission tomography, respectively. Section (2.5) gives an introduction to Monte Carlo methods and their application in particle therapy, and Section (2.6) discusses computational algorithms for predicting positron emitter distributions and activity.

2.1 Interaction of ionizing radiation with matter

2.1.1 Ionizing and non-ionizing radiation

In physics, radiation is commonly classified according to two broad categories, ionizing (IR) and non-ionizing radiation. The key difference between them is that IR is able to excite and ionize atoms in the medium it interacts with, as its energy is within or exceeds the range of 4-5 eV [12]. In fact, the minimum energy required to ionize an atom, i.e. to remove a valence electron, ranges from a few eV for alkali elements up to 24.6 eV for helium [13]. On the other hand, non-ionizing radiation does not have sufficient energy to cause ionizations.

Excitation and ionization are fundamental interactions through which radiation transfers energy to matter. In biological tissues, these processes can lead to DNA damage, which may result in cell dysfunction or cell death. This potential for harmful biological effects underlines the importance of studying ionizing radiation and its interactions with matter [12].

Ionizing radiation can be further divided into two groups:

- Directly ionizing radiations: these are charged particles that deposit energy directly in the medium through many small interactions with orbital electrons, via the Coulomb force [13, 14].

  These particles are:

  - Heavy charged particles: including protons, deuterons, tritons, α-particles (also emitted by radioactive nuclei), heavier atomic nuclei and pions. Particle beams are produced in Coulomb force fields using Van de Graaff generators, cyclotrons, synchrotrons, or heavy-particle linear accelerators.
  - Light charged particles: including electrons and their antiparticles, positrons, which carry a positive charge. Intense continuous electron beams up to 12 MeV are produced by Van de Graaff generators, while pulsed electron beams of much higher energies are generated using linear accelerators, betatrons, and microtrons.

    Electrons or positrons emitted from a nucleus are referred to as β-rays, whereas high-energy secondary electrons are known as δ-rays [12].

- Indirectly ionizing radiations: these are uncharged particles that do not directly interact via the Coulomb force. Instead, they deposit energy in a two-step process. First, they transfer full or partial energy to charged particles in the medium through a small number of high-energy collisions, such as Compton scattering for photons or elastic scattering for neutrons, producing secondary charged particles. Then, these secondary particles undergo many subsequent collisions, depositing energy continuously in the medium. [12, 14].

  Indirectly ionizing radiations are:

  - X-rays: electromagnetic radiation emitted either from atomic electron transitions or from the deceleration of electrons in a Coulomb field.
  - γ-rays: electromagnetic radiation emitted from atomic nuclei or during matter–antimatter annihilation.
  - Neutrons: neutral particles whose beams are typically produced in nuclear reactions, as they cannot be electrostatically accelerated [12].

2.1.2 Heavy charged particles interactions

Passing through matter, heavy charged particles, being surrounded by their Coulomb force field, interact continuously with atoms along their trajectory [12]. This interaction can occur in many different ways:

- Inelastic collisions with the atomic electrons;
- Elastic scattering from nuclei;
- Emission of Cherenkov radiation;
- Nuclear reactions;
- Bremsstrahlung.

Among these, inelastic collisions and elastic scattering are the most frequent interactions and their effects are particle energy loss and deflection from the initial direction. Respectively, inelastic collisions are mostly responsible for the energy loss that causes two different outcomes on atoms in the material. In soft collisions, where the particle passes at a relatively large distance, the atom is excited. In hard collisions, where the particle passes closer to the atom, the energy transferred is sufficient to ionize it [12, 15]. The occurrence of soft or hard collisions depends on both the incident particle energy and its proximity to atomic electrons or nuclei. Instead, elastic scattering occurs when the incident particle passes very close to the nucleus, with the main result being a small angular deflection [12]. While some energy loss may occur in elastic collisions, for heavy charged particles, it is less significant than in inelastic ones [15].

In this context, multiple Coulomb scattering is a specific form of elastic scattering from nuclei. It results from the cumulative effect of many small-angle deflections due to successive Coulomb interactions with atomic nuclei. This process becomes more relevant as the mass of the particle decreases, meaning that lighter charged particles experience significantly more angular deviation than heavy ones when traversing matter [12, 15].

Another type of interaction in which charged particles lose energy is the radiative interaction or Bremsstrahlung. In this process, the incident particle scatters in the electric field of a nucleus and transfers energy to the atom with the emission of a photon. The emission probability is proportional to the inverse square of the incident particle mass and depends on both its energy and the absorbing material [12].

In all cases, the energy deposited is a small fraction of the particle kinetic energy, while the number of interactions per unit path length is large and statistical. Therefore, the total energy loss is relatively stable, allowing the approximation that particles lose energy gradually in a process analogous to friction [12]. This is described by the stopping power quantity $\frac{dE}{dx}$, defined as the average energy loss per unit path length and generally measured in MeV/cm. Specifically, it can be decomposed into three contributions: electronic stopping power, nuclear stopping power, and radiative stopping power:

$$\left(\frac{dE}{dx}\right)_{tot} = \left(\frac{dE}{dx}\right)_{coll,e} + \left(\frac{dE}{dx}\right)_{coll,n} + \left(\frac{dE}{dx}\right)_{rad} \tag{2.1}$$

The first term in Eq. (2.1) refers to energy loss by inelastic collisions with electrons. The second term corresponds to energy loss in elastic collisions with nuclei, which dominates at low energies (below ∼10 keV/n). The third term refers to energy loss by radiation, or Bremsstrahlung, which is negligible for heavy charged particles [12].

A first classical estimation of inelastic collision stopping power was provided by Niels Bohr in 1913 [16], whose formulation is sufficiently accurate for very heavy particles. However, for lighter particles such as protons, quantum effects must be taken into account. To this end, the classical expression was later corrected by Bethe and Bloch, resulting into a quantum-mechanical formulation of stopping power [17, 18]. Later developments introduced two corrections: the density effect correction δ and the shell correction C [15]. The final formula becomes:

$$-\frac{dE}{dx} = 2\pi N_a r_e^2 m_e c^2 \rho \frac{Z}{A}\frac{z^2}{\beta^2}\left[\ln\left(\frac{2m_e\gamma^2 v^2 W_{max}}{I^2}\right) - 2\beta^2 - \delta - 2\frac{C}{Z}\right] \tag{2.2}$$

Where:

- $2\pi N_a r_e^2 m_e c^2 = 0.1535$ MeVcm^2/g
- r_e: classical electron radius
- m_e: electron mass
- N_a: Avogadro's number
- I: mean excitation potential
- Z: atomic number of absorbing material
- A: atomic weight of absorbing material
- ρ: density of absorbing material
- z: charge of incident particle
- $\beta = v/c$ of the incident particle

- $\gamma = 1/\sqrt{1-\beta^2}$
- δ: density correction
- C: shell correction
- W_{max}: maximum energy transfer in a single collision.

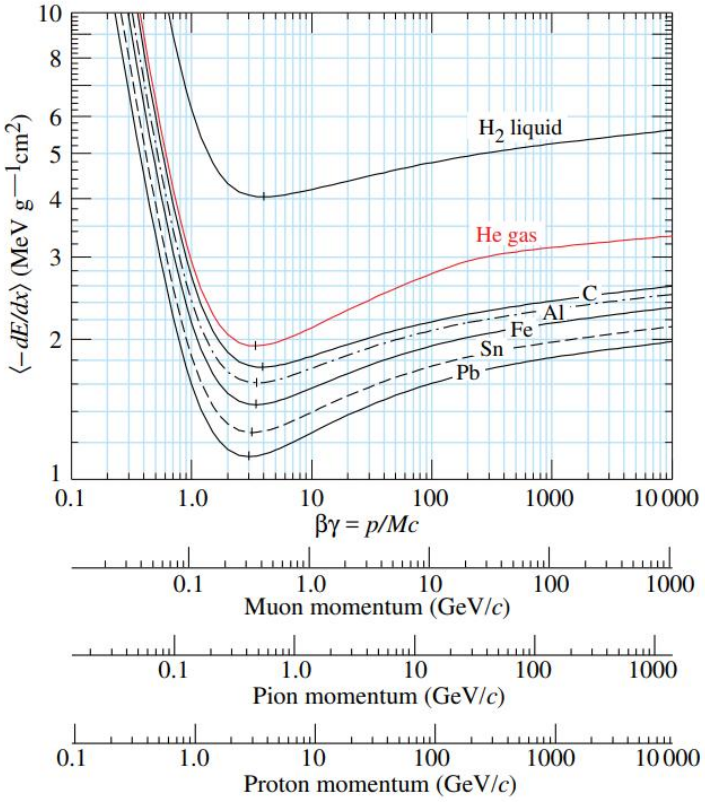

Figure 2.1: Mean mass stopping power in different materials for muon, pion and proton particles [19].

Regarding the velocity dependence, the most significant term is $1/\beta^2$ outside the logarithm ($\beta = v/c$) [12]. As shown in Fig. (2.1), at low (non-relativistic) velocities, stopping power is inversely proportional to β^2, thus decreasing with increasing velocity until it reaches a minimum. A particle at this point is called minimum ionizing particle (MIP), as it deposits the least energy per unit length. Beyond this point, the $1/\beta^2$ factor remains nearly constant and the stopping power increases again due to the increase of the logarithmic term. This relativistic rise is eventually compensated by the density correction. At very low energies, comparable to the orbital electron velocities, the Bethe–Bloch formula breaks down due to additional effects such as shell corrections. In this regime, the stopping power no longer follows the $1/\beta^2$ dependence and decreases with further reduction of the particle energy [15].

From this behavior, it follows that heavy charged particles slow down as they traverse matter, with their energy loss rate increasing toward the end of their path, and then dropping to zero. This results in the Bragg curve, which has a pronounced peak near the end of the range where most energy is deposited, the Bragg peak [15] (see Fig. (2.2)). The significance and applications of the Bragg curve will be discussed in the next sections.

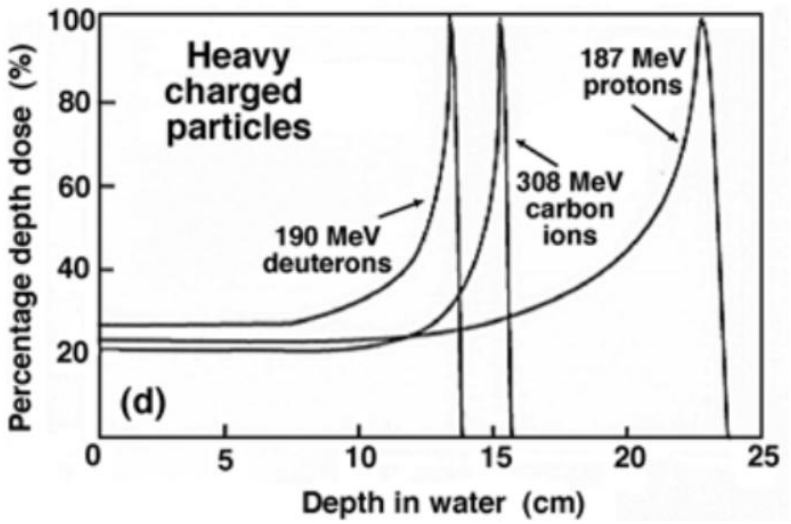

Figure 2.2: Energy deposition in water for different heavy charged particles [13].

A physically distinct interaction channel for heavy charged particles is through nuclear reactions, which become increasingly relevant at energies above several hundred MeV/n. When they occur, these processes dominate the type of interaction, since they proceed via the strong nuclear force rather than electromagnetic mechanisms. However, their contribution to the overall energy loss remains minor compared to ionization [20].
When energetic heavy charged particles interact with target nuclei, they can induce two different types of nuclear reactions: elastic and inelastic collisions. The former are similar to multiple Coulomb scattering but mediated by the strong force; in these collisions, kinetic energy is conserved, and the target nucleus remains intact. In inelastic collisions, kinetic energy is not conserved, and the nucleus undergoes excitation and fragmentation, resulting in a wide variety of final products and secondary particles [8].

Among these processes, nuclear fragmentation (i.e., inelastic nuclear collisions) plays a particularly important role, not because of its direct contribution to the total energy loss, which is relatively small, but due to its influence on the spatial distribution of energy deposition through the production of lighter fragments along the particle's trajectory.

This process can be described as a two-step mechanism: initially, the high-energy collision produces a set of excited nuclear remnants (pre-fragments), typically via abrasion of nucleons from the projectile and/or target nuclei. This is followed by a de-excitation phase during which the pre-fragments release energy through nucleon evaporation, light particle emission, such as protons, neutrons, α-particles and other ions with atomic numbers lower than that of the projectile, ultimately resulting in stable or metastable final fragments [20, 21]. A key difference between protons and heavy ions is that, in heavy-ion collisions, both the projectile and the target can fragment. This leads to projectile fragments that continue traveling forward with velocities close to those of the primary ion. Since at the same velocity the range scales roughly with A/Z^2, these fragments of lower charge than the primary will have longer ranges than the primary particles. Target fragments, on the other hand, have shorter ranges and higher stopping powers, and their evaporation products are emitted isotropically in the fragment's rest frame [8].
For the purposes of this thesis, the nuclear reactions of interest involve ^{12}C ions as projectile particles. These ions can undergo projectile fragmentation, producing isotopes such as ^{10}C and ^{11}C, or they can induce fragmentation of target nuclei, producing ^{14}O, ^{15}O, ^{13}N, as well as ^{10}C and ^{11}C inside the medium [22, 23].

An important parameter in the description of interactions is the range, defined as the expectation value of the thickness of penetrated material until the particle stops [12]. The range depends on the particle type, its initial energy, and the medium [15]. Assuming continuous energy loss, the range is given by:

$$R = \int_0^{E_0} \left(\frac{dE}{dx}\right)^{-1} dE \tag{2.3}$$

Where E_0 is the particle initial energy. For heavy charged particles R corresponds to the mean path-length, as their trajectory is almost rectilinear [13].
Since the nature of the underlying interactions is statistical, the number of collisions required to bring a radiation particle to rest within the medium will vary slightly for each particle (i.e., some may travel further and undergo fewer collisions than others). Hence, there will be a small variation in the range, known as straggling. For heavy charged particles, this effect typically represents only a few percent of the mean range [14].

2.1.3 Light charged particles interactions

Light charged particles, i.e., electrons and positrons, still undergo electromagnetic interactions. However their energy loss in matter differs significantly from that of heavy charged particles [12]. For the collision term in Eq. (2.1), the classical Bethe-Bloch formula must be modified to account for two phenomena. Firstly, due to the low mass of light charged particles the assumption that their trajectory is not deflected during inelastic collisions is no more valid. Secondly, the formula has to address the fact that incident and target particles are indistinguishable after collision due to their equal mass and identical properties [15]. In this context Eq. (2.2) becomes:

$$-\frac{dE}{dx} = 2\pi N_a r_e^2 m_e c^2 \rho \frac{Z}{A}\frac{1}{\beta^2}\left[\ln\left(\frac{\tau^2(\tau+2)}{2(I/m_e c^2)^2}\right) + F(\tau) - \delta - 2\frac{C}{Z}\right] \tag{2.4}$$

Where τ is the kinetic energy of particles in unit of $m_e c^2$ and

$$\begin{aligned} F(\tau) &= 1 - \beta^2 + \frac{\frac{\tau^2}{8} - (2r+1)ln2}{(\tau+1)^2} && \text{for } e^- \\ F(\tau) &= 2ln2 - \frac{\beta^2}{12}\left(23 + \frac{14}{\tau+2} + \frac{10}{(\tau+2)^2} + \frac{4}{(\tau+2)^3}\right) && \text{for } e^+ \end{aligned} \tag{2.5}$$

Furthermore, for electrons and positrons, collision energy loss dominates at low energies, while at energies higher than a few tens of MeV, the second term of Eq. (2.1) is no longer negligible, as it describes the radiative interaction or Bremsstrahlung [15].
For these reasons, the energy deposition profile of light charged particles does not exhibit a Bragg peak, but rather it presents a large and broad peak near the beginning of their path through matter, as shown in Fig. (2.3).

In addition, the low mass of electrons and positrons results into an increased probability of angular deflections through multiple Coulomb scattering compared to heavy charged particles. This leads to substantial lateral spread and unpredictable trajectories, so that the range defined in Eq. (2.3) is up to twice the depth traveled by the particle [13, 14].

Regarding light charged particles, it is important to mention the positron-electron annihilation process. In addition to Coulomb interactions with electrons and nuclei, a positron can annihilate upon encountering an atomic electron. This process results in the conversion of the total mass-energy of the two particles into one, two, or three photons.

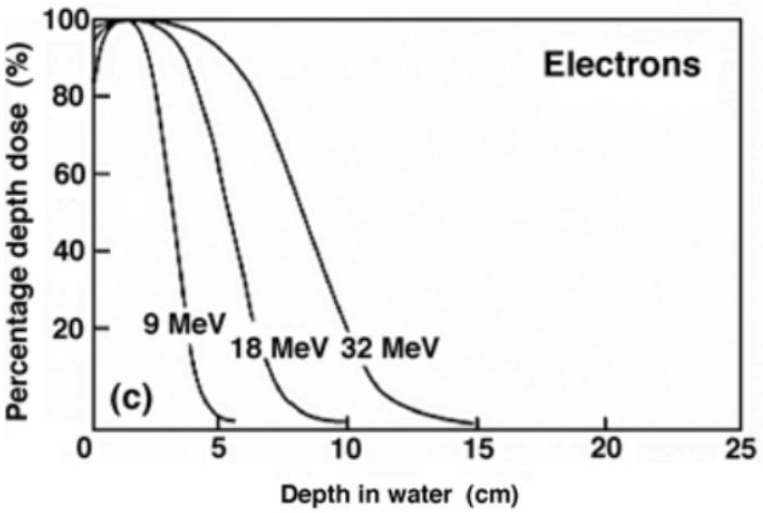

Figure 2.3: Energy deposition in water for electrons with different energy [13].

In the vast majority of cases, the positron first loses all its kinetic energy through interactions with the surrounding medium, and then annihilates with a stationary and essentially free electron. This interaction typically produces two 511 keV photons, which are emitted approximately 180° apart to conserve both energy and momentum.

In about 2% of cases, the positron annihilates while still in motion, a phenomenon known as *annihilation in flight*. If the electron is tightly bound to an atom, the nucleus may absorb the recoil momentum, and in rare cases, a single photon may be emitted carrying nearly the full energy of the positron. However, if the electron is essentially free, two photons are still emitted, though with unequal energies due to the non-negligible momentum of the positron at the time of annihilation [13].

2.1.4 Photons and neutrons interactions

As discussed in the previous sections, charged particles gradually lose energy as they travel through matter, coming to rest due to their continuous interactions. In contrast, photons and neutrons do not slow down as charged particles since they interact with matter with different interaction mechanisms [14]. Specifically, uncharged particles are progressively attenuated in intensity as they pass through a medium. Their behavior follows an exponential decay law:

$$I(x) = I_0 e^{-\mu x} \tag{2.6}$$

where I_0 is the initial intensity of the beam, x is the absorber thickness, and μ is the

linear attenuation coefficient [15]. μ indicates the macroscopic probability per unit length that a particle will interact within the material, and is influenced by both the particle energy and the density and the atomic number Z of the absorber [13].

The principal interaction mechanisms between photons and matter are:

- Photoelectric effect: a photon is fully absorbed by an atom, resulting in the ejection of a tightly bound inner electron. The energy of the emitted photoelectron is given by $E = E_\gamma - E_B$, where $E_\gamma = h\nu$ is the photon energy and E_B is the binding energy of the electron. As a threshold phenomenon, this interaction only occurs when $E_\gamma > E_B$ [13].

- Compton scattering: the incident photon transfers a portion of its initial energy $h\nu$ to a free (i.e. loosely bound orbital) electron, which is then ejected at a recoil angle ϕ with respect to the incident photon direction. The photon itself is scattered by the so called scattering angle θ relative to its initial direction, undergoing an energy loss. Since all scattering angles are possible, the energy transferred to the electron can vary from zero to a large fraction of photon's initial energy [14].

  Starting from the conservation laws of total energy and momentum, it is possible to derive the Compton wavelength shift $\Delta\lambda$, the energy of the scatter photon $h\nu^{'}$ and the kinetic energy of the recoil electron E_K, as presented in Eqs. (2.7), (2.8) and (2.9) [13, 14].

$$\Delta\lambda = \lambda^{'} - \lambda = \lambda_c(1 - cos\theta) \tag{2.7}$$

$$h\nu^{'} = h\nu \frac{1}{1, + \epsilon(1 - cos\theta)} \tag{2.8}$$

$$E_K = h\nu \frac{\epsilon(1 - cos\theta)}{1 + \epsilon(1 - cos\theta)} \tag{2.9}$$

  In Eq. (2.7) λ and $\lambda^{'}$ are the wavelengths of the incident and scattered photons, respectively, and λ_c is the Compton wavelength of the electron. In Eqs. (2.8) and (2.9), $h\nu$ is the incident photon energy and ϵ is the incident photon energy normalized to the electron rest energy [13].

  The microscopic cross section of this process increases linearly with the atomic num-

ber of the absorber [14].

At low photon energies, when the energy transfer to the electron becomes negligible, Compton scattering reduces to Thomson scattering, the classical elastic scattering of photons by free electrons [15].

- Rayleigh scattering: also called coherent scattering, this process involves the interaction of the photon with bound atomic electrons. The scattering amplitudes from the individual electrons add coherently, so that the atom as a whole recoils but remains neither excited nor ionized. The photon is therefore scattered without energy loss, although with a change in direction [13, 15].

- Pair production: when interacting with the electric field near a nucleus, a high-energy photon can convert into an electron-positron pair. This process is only possible when the photon energy exceeds 1.022 MeV, and the presence of a nearby nucleus is essential to conserve momentum [13, 15].

- Photonuclear reactions: these ones occur when a photon directly interacts with an atomic nucleus, often leading to the emission of a neutron (e.g., (γ, n) reactions), or other particles and secondary radiation. Such processes become relevant at photon energies above a few MeV [12].

The microscopic cross section and predominance of each interaction type depend both on the photon energy and on the atomic number of the absorbing material [12].

Like photons, neutrons are electrically neutral and thus unaffected by electromagnetic forces. Their interactions occur via the strong nuclear force, which acts over very short distances. As a result, neutrons can penetrate deeply into materials before undergoing any significant interaction [15]. However, the secondary particles produced in these interactions, such as protons, alpha particles, or heavier nuclear fragments, are highly ionizing and therefore pose a significant biological hazard [13].

2.1.5 Dose: definition and general characteristics

A fundamental quantity in the study of IR interactions with matter and crucial in medical physics is the absorbed dose. It quantifies the expectation value of the average of energy deposited by ionizing radiation in a given mass of material and is defined as [13]:

$$D = \frac{dE}{dm} \tag{2.10}$$

The SI unit of the absorbed dose is the gray (Gy), defined as 1 J of energy absorbed per kg of absorbing material [13]. This quantity provides a direct measure of local energy deposition, which is essential for assessing both biological effects and therapeutic outcomes. The dose distribution in matter depends strongly on both the type and the energy of the incident radiation. Heavy charged particles exhibit a distinct depth-dose profile characterized by a Bragg peak, a sharp maximum of energy deposition occurring just before the particles come to rest. In the entrance region, where only a small number of interactions occur, the dose increases gradually, forming a so-called plateau. This behavior enables highly localized energy delivery in depth, making such particles highly suitable for specific radiotherapy applications [12, 13].

In contrast, at clinical energies, electrons, due to their low mass, undergo substantial multiple scattering, which leads to a broader, more surface-concentrated dose profile without a sharp Bragg peak. As previously discussed, their range is also less well-defined compared to that of heavy particles, which limits their applicability to superficial treatments [12].

Photons interact probabilistically through processes already discussed. As a result, their energy deposition follows an exponential attenuation pattern with depth, typically showing a high dose near the surface (the so-called build-up region) followed by a gradual decrease. Notably, a non-negligible dose is still deposited even at considerable depths inside the medium [15].

For neutrons, dose assessment is more complex. It depends strongly on the composition of the irradiated tissue, and neutron radiation is generally associated with a higher biological effectiveness compared to photons or electrons [13].

Fig. (2.4) shows depth-dose curves for different types of radiations.

2.2 Radioactive decays

2.2.1 Decay process

Nuclides are classified as either stable or unstable. Stable nuclides possess a binding energy configuration that prevents them from spontaneously transforming into other nuclear

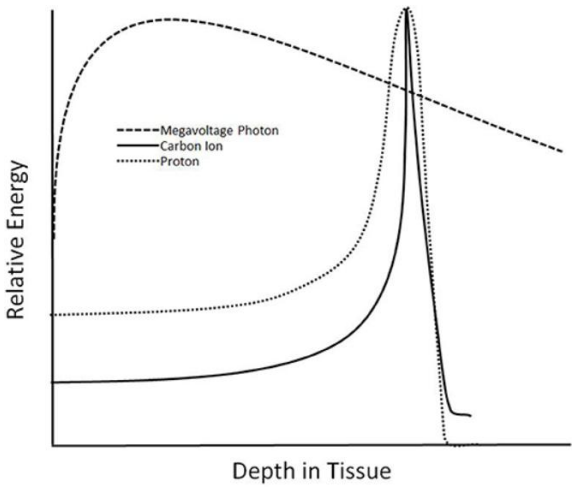

Figure 2.4: Depth-dose curves for different types of radiations [24].

species; they remain unchanged over time. On the other hand, unstable nuclides undergo spontaneous transformations into more stable configurations by emitting radiation in a process known as radioactivity [25]. For this reason, unstable nuclides are also called radionuclides. Nowadays, 275 stable nuclides and over 3000 radionuclides have been identified, either naturally occurring or artificially produced [13].

To reach more stable configurations, radionuclides undergo various nuclear decay processes, which are inherently statistical in nature. Each one is characterized by a specific type of emitted radiation, a decay constant λ, and a branching ratio. λ is the total decay probability per unit time characteristic for each radionuclide, and the branching ratio is the probability that the particles decays in a specific decay channel with respect to the total decay probability [15].

Considering a sample with N radionuclides of the same nuclear species, the mean number of nuclides decaying in a time dt is [15]:

$$dN = -\lambda N \, dt \tag{2.11}$$

Integrating over time, $N(t)$ follows the exponential decay law:

$$N(t) = N(0) \, e^{-\lambda t} \tag{2.12}$$

where $N(0)$ is the number of radionuclides at $t = t_0$.

Knowing the decay law it is now possible to define two other quantities: the mean lifetime, that represents the time required for the number of radionuclides to be reduced by a factor

$1/e$, and the half-time $T_{1/2}$, that is the time at which the number of initial radionuclides decreases by half [15]. Respectively:

$$\tau = \frac{1}{\lambda} \qquad T_{1/2} = \frac{\ln 2}{\lambda} \tag{2.13}$$

A fundamental quantity related to the decay law is the activity A, defined as the number of decays per unit time and measured in Bq (i.e. one disintegration per second) [15]:

$$A(t) = \lambda N(t) \tag{2.14}$$

2.2.2 Types of radioactive decays

Radioactive decay can occur through several mechanisms, depending on the nuclear configuration and energy balance. The decay modes are presented below in order of relevance to the objectives of this work:

- Beta decay: β particles are high-energy electrons or positrons emitted during nuclear transformation mediated by the weak interaction. In β^- decay, a neutron is converted into a proton with the emission of an electron and an antineutrino. Conversely, in β^+ decay, a proton is transformed into a neutron, emitting a positron and a neutrino:

$$\begin{aligned} n \rightarrow p + e^- + \bar{\nu}_e \quad &\Rightarrow \quad {}^{A}_{Z}X \rightarrow {}^{A}_{Z+1}Y + e^- + \bar{\nu}_e \\ p \rightarrow n + e^+ + \nu_e \quad &\Rightarrow \quad {}^{A}_{Z}X \rightarrow {}^{A}_{Z-1}Y + e^+ + \nu_e \end{aligned} \tag{2.15}$$

  The atomic number changes by one unit, while the mass number remains unchanged [13, 15]. The emitted β particles have a continuous energy spectrum because the decay energy is shared with the neutrino, as shown in Fig. (2.5). The upper limit of this spectrum corresponds to the reaction Q-value [15, 25]. In many cases, the daughter nucleus is left in an excited state and de-excites via γ emission or internal conversion [14].

  Radionuclides which decay via β^+ emission are defined as positron emitters (PEs) and play a central role in this thesis work.

- Alpha decay: typical of heavy nuclides ($Z > 82$), this process involves the emission of

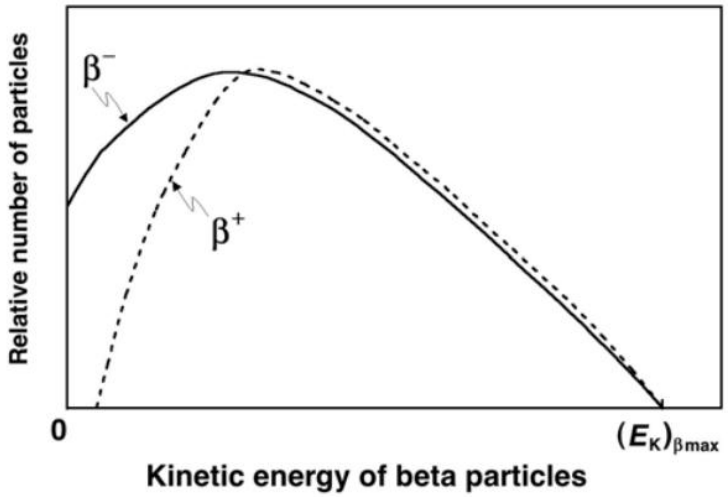

Figure 2.5: Energy spectra for β^- and β^+ decays [13].

a tightly bound ^4_2He nucleus (two protons and two neutrons) to reduce both nuclear mass and Coulomb repulsion, thereby moving toward a more stable configuration [15, 25]. The α-particle is mono-energetic and has very limited range in matter due to its high ionizing power [13].

- Electron capture (EC): as an alternative to β^+ decay, when the decay energy is below 1.022 MeV, EC involves the capture of an inner-shell electron by a proton in the nucleus, resulting in a neutron and a neutrino. This process leads to mono-energetic emissions and may be followed by characteristic X-rays or Auger electrons due to atomic rearrangement [13, 15].

- Gamma decay: excited nuclei, typically produced in other decays or nuclear reactions, can return to a lower state by emitting a γ photon. As this process considers an electromagnetic interaction, it is classified as a purely electromagnetic transition [13, 14].

- Internal conversion (IC): instead of γ emission, the nuclear excitation energy can be transferred directly to an orbital electron, which is then ejected from the atom [12, 14].

- Spontaneous fission: a decay mode characteristic of very heavy nuclei, it involves the splitting of a nucleus into two fragments of comparable mass, accompanied by the release of multiple neutrons (usually 2-4) and energy. This process is relevant for materials containing heavy elements but negligible in biological tissues [13, 25].

- Proton and neutron emission: in neutron-deficient or proton-rich nuclei, direct emission of a nucleon may occur to approach a more stable nuclear configuration. Nonetheless, these decays are rare [13, 15].

2.3 Carbon ion radiation therapy

2.3.1 General aspects

Carbon ion radiation theraphy (CIRT) is one of advanced radiotherapeutic techniques currently employed in the treatment of various tumor types. Owing to the unique physical and biological properties of carbon ions, this technique provides enhanced dose distribution and increased biological effectiveness compared to conventional radiotherapy [3, 5].

The concept of using heavy charged particles for therapeutic purposes was first introduced by Robert R. Wilson in 1946, when he recognized their potential for precise dose localization through the Bragg peak phenomenon [26]. In the following decades, the Lawrence Berkeley National Laboratory (LBNL) initiated experimental treatments using protons and helium ions. A pivotal moment occurred in 1975, when LBNL began clinical trials with high-energy heavy ions, achieving local tumor control rates two to three times higher than those seen with conventional radiotherapy. Further advancements included the development of the first isocentric rotating gantry for proton beam therapy at Fermilab (Batavia, Illinois) in 1990, which minimized radiation exposure to the surrounding healthy tissues.

In 1993, Japan established the world's first dedicated Heavy Ion Medical Accelerator (HIMAC) at the National Institute of Radiological Sciences (NIRS), marking the clinical inception of CIRT. Early results, particularly in the treatment of head and neck tumors, were highly promising, leading to the establishment of additional facilities in Japan (Hyogo, 2001), Germany (Darmstadt, 1997; Heidelberg, 2009), and China (Lanzhou, 2006).

Today, the global deployment of CIRT continues to expand. According to the Particle Therapy Co-Operative Group (PTCOG), there are currently around 200 particle therapy centers that are either operational, under construction, or in planning [27]. To date, more than 220,000 patients have received particle therapy, with approximately 14% treated using carbon ions.

Although CIRT has demonstrated promising clinical results, its use remains limited to selected cancer types and specialized centers, and further studies are ongoing to expand standardized treatment protocols [5].

Clinically, CIRT has shown promising results in managing a range of solid tumors such as skull base chordomas, chondrosarcomas, radioresistant sarcomas, recurrent rectal and pancreatic cancers, hepatocellular carcinoma, and head and neck malignancies. In Japan and parts of Europe, it is also utilized for certain pediatric cases and re-irradiation scenarios [21, 28].

Nonetheless, challenges persist. CIRT facilities are limited worldwide due to high costs and technical complexity. Treatment planning is complicated by factors such as accurate modeling of relative biological effectiveness (RBE), biological dose calculations, and nuclear fragmentation effects along the beam path [20]. Furthermore, although clinical data are promising, the evidence base is still smaller compared to photon and proton radiotherapy, highlighting the need for more randomized trials and long-term outcome studies [5, 29].

2.3.2 Physical aspects

One of the main physical advantages of CIRT compared to conventional radiotherapy can be understood by analyzing the Bragg curve in Fig. (2.4). As discussed in Section (2.1.5), being heavy charged particles, carbon ions deposit a relatively low dose at the beginning of their trajectory through biological tissue. As they travel deeper, the dose increases steeply, culminating in the Bragg peak. Beyond this point, the dose decreases sharply but does not vanish, due to nuclear fragmentation processes along the beam path that generate secondary fragments with lower Z. These fragments, depending on their charge and energy, may stop earlier than the primary ions or penetrate deeper, giving rise to the characteristic dose tail beyond the Bragg peak. [5, 30].

The depth at which this maximum occurs depends primarily on the initial kinetic energy of the projectile particles: increasing their energy increases their penetration range, shifting the peak deeper into tissue. This property allows clinicians to adjust the beam energy to precisely place the Bragg peak within the tumor volume, thus maximizing the dose to

cancerous tissue while minimizing damage to adjacent healthy tissues [5, 30]. In this way, it is possible to achieve very conformal target coverage even for deep-seated tumors [20].

However, the Bragg peak is inherently narrow, typically spanning only 2 to 6 mm [31], which is often insufficient to cover the full extent of larger or irregularly shaped tumors. To address this, the spread-out Bragg peak (SOBP) technique is used. It involves superimposing multiple Bragg peaks at different depths, obtained by modulating the initial energies and appropriately weighting the fluences of the carbon ion beam [5, 30]. This results in a broader and more homogeneous dose distribution across the target volume, while preserving the steep dose gradient beyond the tumor margins. This effect is illustrated in Fig.(2.6).

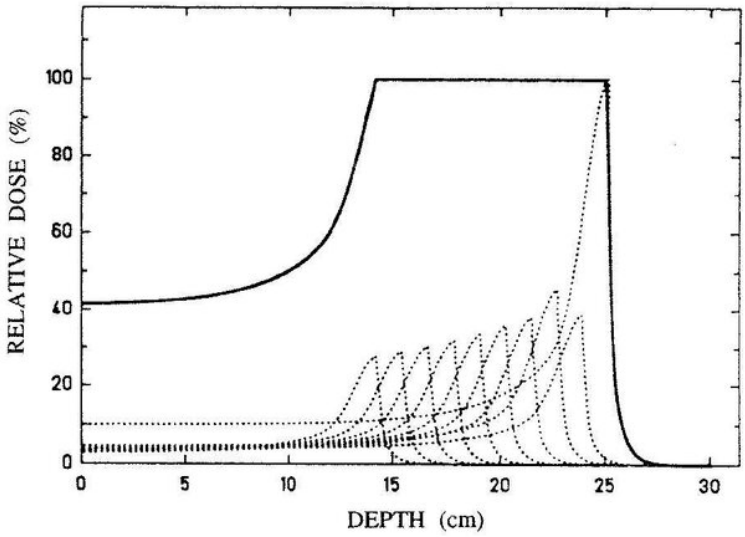

Figure 2.6: SOBP as a function of depth in water [5].

A distinctive physical feature of CIRT is nuclear fragmentation, which occurs when carbon ions interact with atomic nuclei in the tissue. These interactions produce secondary fragments, such as protons, helium, and lighter ions, that generally have longer ranges than the primary carbon ions, leading to a so-called "dose tail" beyond the Bragg peak [20, 31]. This tail partially reduces the sharp dose fall-off but remains reasonably well predictable and is accounted during treatment planning; it is also relatively shallow and extends at large angles in the three-dimensional dose distribution. In addition, nuclear interactions result in the production of PEs, both from the carbon projectiles and from the target tissue. These radionuclides enable *in-vivo* verification of dose deposition

via positron emission tomography (PET) imaging, improving treatment monitoring and quality assurance [20, 22].

Lateral scattering in CIRT is influenced by two competing mechanisms. The first one is multiple Coulomb scattering, which is strongly suppressed for carbon ions due to their larger mass and momentum, allowing the primary beam to maintain a relatively straight trajectory through tissue. The second one is nuclear fragmentation, which produces lighter secondary particles that are emitted at wider angles, thereby broadening the lateral and longitudinal dose distributions around and beyond the Bragg peak [20, 30].

The overall physical behavior of carbon ions is closely linked to the concept of linear energy transfer (LET), which quantifies the energy deposited per unit path length by ionizing particles and it is typically measured in keV/μm [4]. LET depends on both the charge and velocity of the particle, and is not constant along the beam path. In the entrance region, carbon ions travel at high speed and deposit energy sparsely, behaving as low-LET radiation. As they slow down near the Bragg peak, ionization events become denser and more localized, resulting in high-LET radiation [30].
Among the physical characteristics described, LET is the primary determinant of the enhanced biological effectiveness of carbon ions [4], which will be explored in the following section.

2.3.3 Biological aspects

It is known that different types of incident particles that deposit the same amount of dose produce different biological effects in living tissues [4]. This depends mainly on the particle LET.

The primary biological effect of interest in radiotherapy is DNA damage. Two mechanisms are involved. In the direct mechanism, radiation induces breaks directly in the DNA double helix. In the indirect mechanism, radiation interacts with other components of the cell, including water molecules, producing reactive oxygen species (ROS), which can chemically react with DNA and induce damage. Each type of radiation tends to favor one mechanism over the other [4].

Since low-LET particles are "sparsely ionizing" radiation, they release energy in a more random and uniform manner across the biological target, causing DNA damage that is in general spatially isolated, typically in the form of single-strand breaks (SSBs). These lesions are usually easy for the cell to repair through natural mechanisms, often without lasting consequences. Additionally, low-LET radiation tends to induce damage predominantly through the indirect pathway via ROS.
In contrast, high-LET radiation is "densely ionizing", meaning that the energy deposition is more clustered along the particle track. This leads to complex DNA damage, especially double-strand breaks (DSBs), which are much harder for the cell to repair [30].

The biological response to radiation in living tissues does not depend only on LET, but also on many other factors such as total dose, dose rate, number of dose fractions, cell and tissue type, oxygenation state, cell cycle phase, and the considered biological endpoint [4, 30]. The quantity that takes all of these variables into account is the relative biological effectiveness (RBE). It is defined as the ratio between the dose from a reference radiation and the dose from the radiation under investigation required to produce the same biological effect:

$$RBE = \left.\frac{D_{ref}}{D_{rad}}\right|_{iso} \tag{2.16}$$

Generally, the reference radiation used is X-rays, for which RBE = 1 for definition. A higher RBE value corresponds to a greater biological effect. For carbon ions, the RBE is not constant along the beam path; it increases and reaches its maximum value at the distal edge of the Bragg peak. This spatial variation implies that the DNA damage produced in the entrance region is generally less complex and more amenable to repair than the clustered lesions induced at the distal edge [20]. Typically, RBE values for carbon ions range between 2.5 and 3 [4, 30].

A further relevant concept is the oxygen enhancement ratio (OER), which quantifies the influence of oxygen on radiation-induced cellular damage. It is defined as the ratio between the dose required under hypoxic conditions and the dose required under aerobic conditions to produce the same biological effect [4]:

$$OER = \left.\frac{D_{hypoxic}}{D_{aerobic}}\right|_{iso} \tag{2.17}$$

For low-LET radiations, the OER typically ranges from 2.5 to 3, meaning that cells in low-oxygen environments are up to three times more resistant to radiation than well-oxygenated cells. This is because oxygen molecules interact with radiation-induced free radicals to stabilize DNA damage and inhibit repair mechanisms [4]. In hypoxic conditions, many of these radicals are neutralized before causing lethal damage, leading to reduced radiation effectiveness.

For high-LET radiation such as carbon ions, the OER decreases compared to low-LET radiation, indicating reduced dependence on oxygen; however, it remains slightly above 1 in the Bragg peak region, indicating that cytotoxicity is reduced by hypoxia, but it is still partially effective [4, 20, 21]. Recent findings suggest that carbon ions can achieve OER values as low as 1.2, depending on LET and tumor type, and that their ability to overcome hypoxia-induced resistance is more pronounced than that of photons or protons [32, 33]. Altogether, while current findings support the biological rationale for using carbon ions in hypoxic tumors, a deeper mechanistic understanding and more robust clinical validation are essential to fully realize the therapeutic potential of CIRT, especially through trials incorporating functional hypoxia imaging [33].

2.3.4 Facilities, beam delivery systems, and treatment verification

The main clinical facilities worldwide for CIRT use accelerators to accelerate carbon ions, but they differ in their beam delivery systems. These machines must be capable of delivering carbon ions (^{12}C isotopes) with energies typically ranging from 85 to 430 MeV/n, sufficient to reach tumors located at various depths within the human body. To achieve this, synchrotrons are employed, as they allow flexible modulation of beam energy during treatment, enabling precise control of the ion penetration depth. In contrast, cyclotrons are not currently used for carbon ions in clinical settings, as accelerating ^{12}C-ions requires highly specialized machines that are more complex and less practical than synchrotrons [20, 34, 35].

The beam delivery system transports the beam from the accelerator to the patient,

modulating its shape, energy, and intensity in accordance with the treatment plan. Beam modulation can be implemented through two main types of systems. The passive system uses absorbers and collimators to shape the beam, but this approach results in less accurate targeting of the tumor, leading to a broader dose distribution to surrounding healthy tissues. In contrast, the active system (or pencil beam scanning) employs magnetic fields to dynamically and precisely steer the beam, enabling three-dimensional dose modulation. This allows an improvement of conformity of the treatment volume to the tumor and minimizing the dose to healthy tissues [36, 37].

A critical step in all radiation therapies is the treatment planning process, which involves the definition of a dose distribution that maximizes irradiation of the tumor while sparing healthy tissues. This plan is developed using imaging data, primarily from X-ray computed tomography (CT) scans or X-ray radiography scans, which provide detailed anatomical information essential for accurate dose calculation [28]. Verification of patient positioning and treatment accuracy is routinely performed using CT imaging before each session. Additionally, PET is increasingly used for *in-vivo* verification of dose deposition, by detecting PEs produced during irradiation [22, 23]. The use of PET for treatment verification will be discussed in deeper detail in the following Section.

2.4 Imaging with PET

2.4.1 Positron emitter tomography (PET)

The use of annihilation coincidence detection for radionuclide imaging was first described in the early 1950s by Brownell and Sweet [38]. This imaging technique is based on the physical process of annihilation between a positron and an electron, which produces a pair of photons.

A fundamental requirement for PET is the presence of PEs inside the human body, as the goal is to reconstruct their distribution to investigate physiological and pathological processes. For this reason, the unstable nuclides used typically have a half-life shorter than 2 hours. One of the most common radionuclides used in nuclear medicine is ^{18}F, which has a half-life of about 110 minutes and usually delivered as the radiopharmaceutical fluorodeoxyglucose (^{18}F-FDG) [39]. The typical administered activity of PET radiotracers

in clinical practice ranges from approximately 125 to 740 MBq, balancing image quality and patient radiation dose [40].

The physical process begins with the emission of a positron by a radioactive nucleus within the medium. Depending on its kinetic energy after emission, the positron will travel a distance between a fraction of a millimeter and several millimeters from its point of origin. Eventually, it encounters a nearby atomic electron, leading to annihilation. This results in the production of two 511 KeV γ photons, which, in order to conserve energy and momentum, are emitted approximately at 180° [39].
The photons then reach one of the detector elements and interact with it mainly via the photoelectric effect or Compton scattering. These interactions produce scintillation light, which is collected by a photodetector to generate an electrical signal that is subsequently analyzed by the detector's read-out system. If both photons are detected within a narrow time window, typically a few nanoseconds, it is assumed they originated from the same annihilation event.
The annihilation event is then localized along the line of response (LOR) connecting the two detection points. By collecting a large number of these coincident photon pairs, an image of the spatial distribution of radionuclides can be reconstructed using computational algorithms [41].

A typical PET scanner consists of a ring of radiation detectors arranged around the subject. Commercial PET scanners generally use scintillator crystals such as Bismuth Germanate (BGO) or Lutetium Oxyorthosilicate (LSO). BGO, being less expensive, is often used for whole-body scans that require multiple detector rings, while LSO, due to its superior timing resolution, is preferred in dedicated PET systems [42].

It is worth knowing that, PET images reflect only the distribution of the radiotracer, which is a functional or metabolic signal, and not the underlying anatomical structures. This is because PET detectors measure γ-rays resulting from annihilation events but do not provide direct information about tissue density or morphology. As a result, it is often difficult to accurately localize functional abnormalities within the anatomical context of the body.

To overcome this limitation, PET is commonly combined with X-ray CT, which provides high-resolution anatomical data. The union of PET and CT images enables precise correlation between metabolic activity and anatomical landmarks, improving diagnostic accuracy and clinical utility [39, 42].

2.4.2 Paramenters of PET system and image reconstruction techniques

The performance of a PET system, namely, the quality of the resulting images, depends on several factors:

- Spatial resolution: this refers to the ability of the PET system to distinguish between two points in space. It is influenced by factors such as the detector element size, positron range, photon acollinearity, and depth-of-interaction effects. Typically, the spatial resolution is around 4-5 mm full width at half maximum (FWHM) for clinical scanners [39].

- γ-ray detection efficiency: it is mainly determined by the scintillator crystal properties, such as density and atomic number, which influence the stopping power of the crystal and thus its ability to fully absorb incoming γ photons, and scintillation decay time, which affects the temporal resolution and the ability to detect successive events efficiently.

- Attenuation and scatter: these occur both within body tissues and the detector itself, leading to a loss and change in direction of γ photons before they reach the detector. Attenuation reduces the number of detected photons, lowering image signal-to-noise ratio, while scatter changes the photon trajectories and introducing image artifacts.

- Random and scattered coincidences: random coincidences arise from unrelated photons detected within the coincidence window, while scattered coincidences occur when photons change direction before detection. Both add noise, degrading image quality and requiring correction.

- System sensitivity: the ability to detect true coincidence events per unit of administered radioactivity.

Modern PET systems often incorporate Time-of-Flight (TOF) capability, which improves image quality by using the difference in arrival time between the two annihilation photons to more accurately localize the annihilation event along the line of response

[39, 42]. TOF-PET significantly enhances signal-to-noise ratio, especially in larger patients, and improves contrast recovery.

Regarding image reconstruction, two widely adopted iterative algorithms are:

- List-Mode Maximum Likelihood Expectation Maximization (LM-MLEM): this method uses individual event data and applies a statistical approach to maximize the likelihood function. It is particularly useful when handling dynamic or gated acquisitions, as it retains full temporal and spatial resolution [43, 44].
- Ordered Subsets Expectation Maximization (OSEM): an accelerated version of MLEM, OSEM divides the dataset into subsets and updates the image after each subset. This technique offers a good compromise between reconstruction speed and accuracy, and is the standard algorithm in most commercial PET systems [45].

Compared to traditional analytical methods like Filtered Back Projection (FBP), these iterative algorithms provide better noise suppression and improved image fidelity, especially under low-count conditions or when high spatial resolution is required [41].

2.4.3 Range verification in CIRT with PET

Range uncertainties in CIRT arise primarily due to anatomical changes, patient positioning errors, and limitations in converting CT Hounsfield units into stopping powers for treatment planning. These uncertainties can lead to discrepancies between the planned and actual ion range, potentially resulting in incorrect dose distributions in both tumor and surrounding healthy tissues. To address this issue, it is necessary to monitor the ion range during treatment, verify the spatial accuracy of the irradiation field, and detect any deviations between the prescribed and delivered dose caused by patient misalignments or anatomical variations over the course of therapy [6, 7]. To ensure accurate dose delivery and minimize the risk of both underdosage and overdosage, range monitoring should be performed *in-vivo* and non-invasively, either during or immediately after irradiation. PET technique is commonly used for this purpose.

PET monitoring is achieved by exploiting the production of PEs generated by nuclear reactions during irradiation. Many preliminary studies and experiments have been conducted and nowadays PET systems are among the most widely used tools for range

verification in CIRT [8, 46]. By analyzing the spatial activity distribution measured with PET, the localization of the delivered dose can be inferred. One of the earliest experimental confirmations was provided by [47], which stated that the range distributions of PEs had a pronounced maximum near the range of the primary particles. Moreover, [9] found that activation and dose distributions were not directly proportional. This is due to the fact that different underlying physical processes are involved: nuclear mechanisms for secondary emissions versus electromagnetic processes for the dose. In the case of carbon ions, PEs originating from target nuclei remain almost at the interaction point, while PE projectile fragments travel further and accumulate near their end of range, producing a peaked activity signal just before the Bragg peak [48]. This occurs because such fragments are isotopes of the primary ions that, having the same charge but lower mass, stop earlier. The behavior is shown in Fig.(2.7). This spatial correlation enables PET imaging to be used as an indirect but effective indicator of dose delivery.

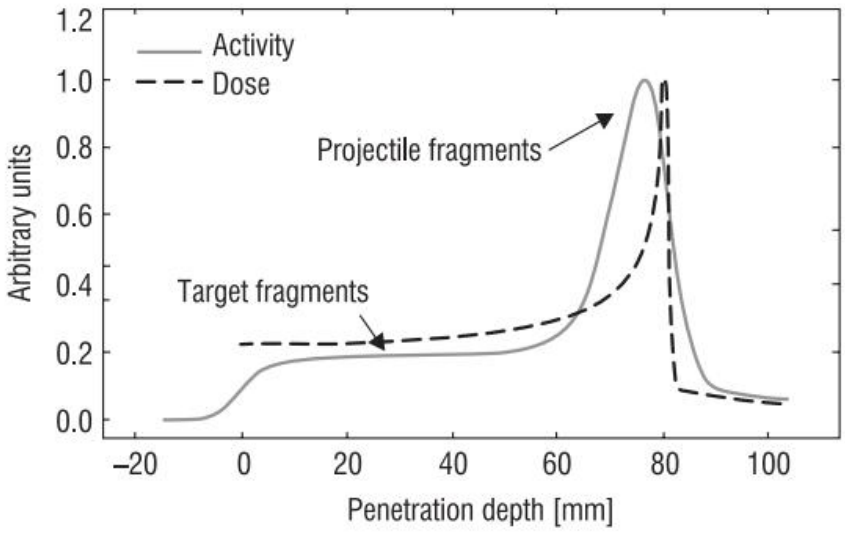

Figure 2.7: Dose and activity distribution as a function of depth [48].

PET-based range verification entails a comparison of the measured positron emissions with a predicted activity distributions. Monte Carlo (MC) simulations are typically employed to reproduce PEs activity distributions based on treatment plan parameters and PET system characteristics, enabling comparison between expected and measured PET signals [49–51]. Although highly accurate, MC simulations require significant computational resources and time, which currently limits their routine clinical applicability. As an alternative to MC methods, analytical approaches were proposed to predict positron

emitter distribution (PED).
Examples of MC simulation tools developed for range verification as well as computational algorithms for PET predictions are described in detail in Sections (2.5.3) and (2.6), respectively.

One of the main challenges in PET-based range verification is the low activity produced by activated nuclei, typically around 200 Bq $Gy^{-1}cm^{-3}$ in CIRT, which is significantly lower than diagnostic PET activity levels [9]. In addition, the short half-life of PEs and biological washout reduce the PET signal rapidly if measurements are performed post-irradiation, in the so-called off-line PET [7, 52]. To overcome the limitations of off-line PET and to improve the spatial accuracy, on-line, or in-beam, PET acquisition during treatment has been developed, requiring dedicated PET scanners compatible with the beam delivery system [53, 54]. The main difference between off-line and on-line beam PET acquisition lies in the timing of image acquisition: the off-line measurements are acquired several minutes after treatment [7], while the on-line signal is acquired during irradiation or in short pauses between pulsed beam deliveries [55]. During off-line acquisition, the main contribution to the signal comes from ^{11}C, which has a half-life of 20 min, while during on-line acquisition, the contribution of short-lived isotopes as ^{10}C and ^{15}O becomes more pronounced. [52].
In summary, PET imaging combined with advanced computational modeling and innovative scanner technology provides a robust and accurate method for *in-vivo* range verification in CIRT, helping to ensure that the delivered dose conforms to the prescribed treatment plan.

2.4.4 OpenPET system

One of the most recent PET scanners designed for in-beam PET acquisition is the OpenPET system, developed at the Heavy Ion Medical Accelerator (HIMAC) in Chiba, Japan. It represents the first open-geometry 3D PET scanner worldwide specifically conceived for dose verification in particle therapy [56]. Its innovative geometry provides an open space that can be physically accessed during acquisition, while still allowing highly accurate 3D imaging [57].

Over the years, two prototypes of the OpenPET system have been developed: the dual-ring OpenPET (DROP) and the single-ring OpenPET (SROP). The latter has a cylindrical shape truncated by two parallel planes, tilted with respect to the axial direction, forming an ellipsoidal open space. This configuration creates an accessible field of view (FOV), ensures higher sensitivity at the center, and requires fewer detectors compared to the DROP system, while still providing a beam path suitable for in-beam PET acquisition. In addition, the SROP geometry enables the treatment beam port to be placed as close as possible to the patient, thereby reducing beam broadening. The use of depth-of-interaction (DOI) detectors further guarantees uniform spatial resolution, even though the detectors are arranged in an ellipsoidal ring [58, 59] (see Fig. (2.8)).

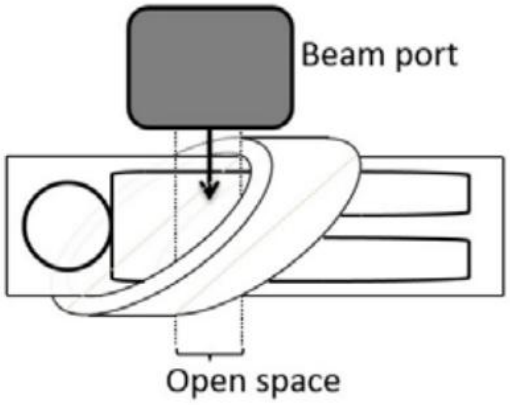

Figure 2.8: Single-ring OpenPET simplified geometry [59].

The tilt angle of the SROP geometry can be derived from the desired open-space width C, the detector ring axial width W, and the bed width B (i.e., the cylinder diameter). As Fig. (2.9) shows, in the top view, the geometry resembles a parallelogram with side lengths equal to W, while in the lateral view it appears circular with a diameter B. When observed perpendicularly to the detector ring, the geometry takes the shape of an ellipsoid [58].

Two different detector arrangements are possible in the SROP: the slant-ellipsoid (SE) arrangement, where detector rings are stacked at a slanted angle along the bedside; and the axial-shift (AS) arrangement, where block detectors are incrementally shifted along the axial direction, so that the center of each detector surface is slanted with respect to the axis. Simulation studies have shown no significant differences in image quality between the two configurations. However, small-scale prototype experiments revealed that the AS-type geometry is more compact and easier to construct than the SE-type, as it avoids the

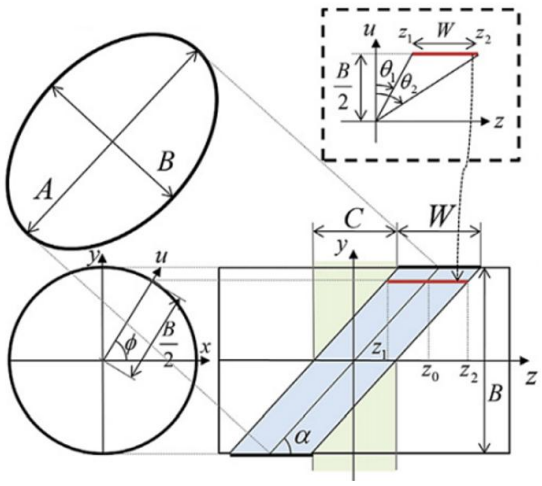

Figure 2.9: Geometrical analysis of the top, lateral and perpendicular view of SROP [58].

complexity of fabricating ellipsoidal block rings. Based on these results, the whole-body OpenPET system was ultimately implemented using the AS-type configuration [56].

The whole-body SROP consists of 4 axially shifted detector rings, each containing 40 DOI detectors. This configuration reduces parallax error, since most LORs are oblique, and DOI detectors can identify the interaction depth in addition to the 2D position. The detector ring has an inner diameter of 660 mm and a total axial length of 214 mm. The ring plane is tilted by 45° relative to the axial (z) direction, creating an open space of 430 mm. Each DOI detector is composed of a 16×16×4 array of Zr-doped gadolinium oxorthosilicate (GOSZ) scintillator crystals (2.8×2.8×7.5 mm^3 each), forming blocks of 46×46×30 mm^3. These are coupled to 64-channel photomultiplier tubes (PMTs) with super-bialkali photocathodes. The detectors, equipped with front-end electronics, are connected to the data acquisition (DAQ) system via 7 m coaxial cables, in order to minimize radiation damage to the electronic circuits during use in particle therapy irradiation rooms. Data are acquired in singles list-mode, with coincidence detection performed offline by software [57] (see Fig. (2.10)).

The measured performance includes an energy resolution of 14% and a timing resolution of 4.4 ns. Consequently, the energy window is set to 400-600 keV and the coincidence timing window to 10 ns. Random correction is performed through the delayed coincidence method, using a 10 ns delayed timing window with a 128 ns delay [57].

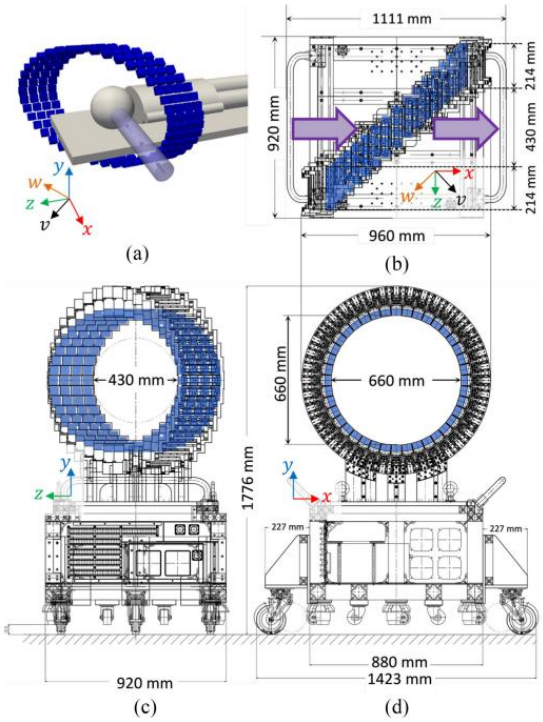

Figure 2.10: Conceptual illustration of SROP (a) and design sketches: top (b), side (c), and front (d) views. The blue blocks are the scintillator blocks. The red, blue, green, black, and orange arrows indicate the x, y, z, v, and w directions defined in the system, for which the origin is the FOV center [57].

2.5 Monte Carlo methods

2.5.1 General aspects

MC methods are computational techniques that use random variables to estimate solutions to mathematical problems that are difficult to treat analytically or numerically. They are particularly useful in systems whose behavior can be described probabilistically. In particular, MC approaches are based on a few fundamental principles [60]:

- The outcome T of a stochastic process depends on a set of random variables $x_1, x_2, \ldots, x_k$, such that $T = T(x_1, x_2, \ldots, x_k)$.
- Statistical properties of the process are described by expected values and variances, for example $\sigma_T^2 = \langle T^2 \rangle - \langle T \rangle^2$.
- Many MC problems can be expressed as the estimation of multidimensional integrals:

$$I = \langle T \rangle = \int_\Omega T(x_1, x_2, \ldots, x_k)\, g(x_1, x_2, \ldots, x_k)\, dx_1 \ldots dx_k \tag{2.18}$$

where g represents the joint probability density of the input variables.

At the core of MC algorithms is the generation of sequences of random numbers, typically pseudo-random, due to the deterministic nature of digital computers. Given a seed x_0, a deterministic algorithm produces a sequence $x_1, x_2, \ldots$ that approximates independent uniform samples over [0,1), with the sequence eventually repeating after a period that depends on the generator [60].

In particle physics simulations, such as those commonly used in medical physics, MC methods perform particle tracking: individual particles are followed step by step through probabilistic interactions with matter. Each particle's trajectory, including scattering events, energy deposition, and generation of secondary particles, is sampled according to known physical interaction probabilities. This approach allows MC simulations to provide highly detailed reference solutions, which can then be used to validate analytical methods, optimize experimental setups, and support data analysis.

2.5.2 MC simulation tools

In medical physics, MC simulations are commonly implemented with specialized software tools, including Geant4, FLUKA, and MCNP.

Geant4 is an open-source simulation toolkit developed by CERN and Geant4 Collaboration using object-oriented programming principles, that models the interaction of radiation with matter through MC techniques [61]. It has been widely applied in many fields, including high-energy, nuclear and accelerator physics, as well as medical and space applications.
The modular software architecture of Geant4 allows for a detailed representation of the physical setup: system geometry, materials involved, types of particles, their initial generation, their transport through matter and physics models, taking into account relevant physical interactions. In addition, Geant4 provides tools to simulate detector response, record detailed information about each particle's trajectory, such as position, momentum, and energy at each step, and manage output by allowing the user to choose which types of data to save and at what level of granularity. A key feature of the toolkit is the inclusion of a wide set of physics models covering a broad energy range. These models, based on experimental cross-section data and theoretical formulations, enable accurate simulation

of particle-matter interactions (Section (2.1)) [61].

FLUKA instead is a general-purpose MC code developed by CERN and INFN, optimized for highly accurate simulations of particle transport and interactions, including nuclear reactions. It is extensively used in medical physics, particularly in particle therapy, due to its precise modeling of energy deposition and secondary particle production. Unlike Geant4, FLUKA provides pre-implemented physics models that are extensively validated, which can simplify setup while ensuring high accuracy [62].

Similarly, MCNP (Monte Carlo N-Particle), developed at Los Alamos National Laboratory, is designed for neutron, photon, and electron transport in complex geometries. It is widely used for dosimetry, radiation shielding, and safety assessments. MCNP relies on a text-based input for geometry and materials and provides accurate particle transport calculations, particularly for applications involving neutrons and photon shielding [63].

2.5.3 MC methods in PET signal prediction

In particle therapy, MC simulations are widely used for dose distribution calculations and treatment plan verification [49]. In the context of PET-based range verification, MC methods are also applied to predict the expected PET signal. For example, in [64] the FLUKA MC code is used to compute both the dose and the PED from clinical CT data in proton therapy. Additionally, the INSIDE project [65] implemented Geant4 simulations to model in-beam PET imaging for CIRT, demonstrating the feasibility of real-time monitoring.

For PET signal prediction, the starting point is the definition of the input data, which include the patient's anatomical geometry, with the tissue density and elemental composition [9, 23], together with information from the treatment plan, such as the beam spot parameters and the temporal structure of the delivered fraction.
Based on these inputs, the codes reproduce the relevant physical processes: the transport and energy loss of the primary ions and their fragments in tissue, nuclear reactions leading to the production of PEs, their subsequent decay, and the annihilation of positrons followed by the emission and detection of γ-rays. [49].
The MC simulation workflow is typically divided into two main steps. In the first step,

the primary particles are tracked and their interactions with the target are simulated to generate the spatial and temporal distribution of PEs.

PED then serves as the input for the second step, in which PET images are generated. This step includes modeling positron annihilation, γ-ray generation, and incorporating the PET system's geometry and response characteristics. This step can be achieved either through full MC simulations [65] or, alternatively, by analytical models [66, 67].

Even though MC simulations are a powerful tool for predicting PET images, they are computationally intensive and time-consuming, which limits their integration into clinical workflows. To address these challenges, several fast MC codes have been developed [68–70].

However, currently available fast MC tools have been developed mainly for proton therapy and are not yet established for carbon-ion therapy, especially in terms of PET-based range verification, including PE production and γ-ray detection [50, 51].

2.6 Computational algorithms in PED and activity prediction

Over the years, several alternatives to time-consuming MC simulations have been developed to predict PED in particle therapy.

In [71, 72], an experiment-based yield approach in CIRT was presented, in which PEDs are reconstructed by linearly superimposing the measured PE yields from different reference materials, scaled according to the local elemental composition of the target. In [71] the feasibility of this approach was demonstrated in one dimension, while the follow-up study [72] extends it to three dimensions. However, the latter highlights some limitations in accurately describing the lateral distribution of projectile fragments and secondary particles, due to the simplifying assumptions of the model.

A filtering approach was proposed in [73] for the first time for proton therapy to predict PE activity $P(z)$ along depth z in tissue. It is calculated as the convolution of the depth-dose distribution $D(z)$ with a filter kernel $f(z)$:

$$P(z) = D(z) * f(z) = \int_{-\infty}^{\infty} D(z')\, f(z - z')dz' \tag{2.19}$$

Where $f(z)$ is defined as a set of functions $\tilde{Q}_\nu(x)$ which are the convolution of a Gaussian $G(x)$ and a power-law $P_\nu(x)$ function.
This filtering approach was later extended in [11] to the carbon ion case, applying it to the 1D PED along the beam axis. The same methodology had already been explored in [74] using patient geometry and performing a quasi-3D distributions, i.e. voxel lines, showing some limitations of [11].

Finally, in [10], the analytical framework of [11] is adjusted and extended to compute the full 3D PED. This extension is based on a pencil beam algorithm (PBA) and some improvements on the 1D approach were also made, including a more realistic modeling of longitudinal heterogeneity effects in projectile fragment PED, while maintaining significantly lower computational costs compared to MC simulations. This approach will be described in detail in the following Chapter.

3

Materials and Methods

In this thesis work, a structured methodology was adopted to evaluate and validate an analytical approach for predicting the three-dimensional PED for PET-based monitoring during CIRT, as proposed in [10].
First, MC simulations were carried out using a PMMA phantom, in parallel with analytical calculations, with the aim of comparing simulated and analytical results and validating the proposed method. Next, a procedure to convert PED into an activity distribution was developed, in order to compare the analytical predictions with in-beam PET measurements and to assess the practical reliability of the calculations.

The chapter is organized as follows: in Section (3.1) the analytical approach described in [10] is presented in detail; Section (3.2) illustrates the performed MC simulations; Section (3.3) explains the procedure for converting PED into activity distribution; finally, Section (3.4) presents the comparison between the predicted activity distribution and the PET measurement data.

3.1 3D Analytical approach of positron emitter distribution

The novel analytical method described in [10] is based on a pencil beam algorithm (PBA), sharing a similar input structure with the approach originally proposed in [75] for 3D dose reconstruction in proton therapy. This dedicated computational framework allows the calculation of the 3D PED for a single pencil beam spot.

The construction of the PBA in [10] can be summarized as follows:

- Laterally integrated depth positron emitter distribution (IDPED): the IDPED is derived by applying analytical functions combined with a filtering approach to the laterally integrated depth-dose (IDD) at corresponding energies in a reference material. The parameters of these functions, as well as the reference IDD, are obtained from MC simulations. In practical applications, the IDD may also be extracted from the 3D dose distribution of each ion beam spot.
- Lateral distribution of PED: the lateral spread of PEs is parameterized by fitting distributions calculated by MC simulations in the reference material along the penetration depth, using either single or double Gaussian functions as appropriate.
- Heterogeneity corrections: the PBA includes methods to account for longitudinal heterogeneities along the beam path, as well as lateral heterogeneities across the beam cross-section. Longitudinal heterogeneities are handled through scaling and mapping techniques, while lateral heterogeneities are incorporated using a ray-casting approach [76, 77].

3.1.1 Generation of database using MC simulations

The Geant4 toolkit (version 10.07.p04) was employed in [10] to generate a reference dataset used as input for the novel 3D analytical method for modeling PED in CIRT.
The physics list selected for this simulation is QGSP_BIC (Quark-Gluon String Precompound with Binary Cascade for light ions), which combines several models to accurately describe hadronic interactions over a wide energy range. This choice is based on the validation studies presented in [78, 79], which demonstrate that QGSP_BIC provides the best overall agreement with experimental data in terms of the production yield and spatial distribution of PET-relevant isotopes, such as ^{10}C, ^{11}C and ^{15}O, under ^{12}C-ion irradiation.
For the reference dataset generation in [10], the simulation was carried out using a homogeneous cylindrical phantom filled with a reference material representative of human tissues and whose composition is listed in Table (3.1).

The ^{12}C-ion beam is modeled as a mono-energetic and mono-directional pencil beam that propagates along the cylinder axis (z-direction). Numerous independent simulations are performed, each with a different initial nominal energy ranging from 80 to 430 MeV/n and using 5×10^8 primary carbon ions per simulation.

Mass density	$1.54\ \mathrm{g{\cdot}cm^{-3}}$
Electron density	$4.71{\cdot}10^{20}\mathrm{cm^{-3}}$
Mass abundance	
Hydrogen (H)	2%
Carbon (C)	31%
Nitrogen (N)	26%
Oxygen (O)	38%
Phosphorus (P)	1%
Calcium (ca)	3%

Table 3.1: Material information of reference material [10]

Following the findings reported in [23], the production of the main PEs relevant to CIRT, ^{10}C, ^{11}C, ^{13}N, ^{14}O, and ^{15}O, are scored in each voxel of the phantom, along with the physical dose.

3.1.2 Determination of target and projectile PE

After the generation of the reference dataset, the first step in the framework for 3D PED prediction is the determination of PEs to be included.
Following [23], the relevant isotopes are ^{10}C, ^{11}C, ^{13}N, ^{14}O, and ^{15}O. Among these, ^{10}C and ^{11}C can be produced through both projectile and target fragmentation, whereas the remaining isotopes originate exclusively from target fragmentation. As outlined in Section (2.1.2), projectile and target fragments differ in spatial distributions due to their distinct kinetic energies (Section (2.4.3)). For this reason, these PEs were separated into target and projectile groups by comparing the kinetic energy of each fragment with that of the incident ^{12}C-ion at the moment of interaction (see Fig. (3.1)), and by applying a threshold of 70% of the incident energy for ^{11}C [11] and 50% for ^{10}C [10].

This classification leads to the consideration of five target PEs ($^{10}C_{tar}$, $^{11}C_{tar}$, ^{13}N, ^{14}O, ^{15}O) and two projectile PEs ($^{10}C_{proj}$ and $^{11}C_{proj}$). Finally, a further subdivision of PEs was made according to the type of target nuclei involved in their reaction channels under the assumption that a given nucleus can only produce isotopes with atomic numbers less than or equal to its own.

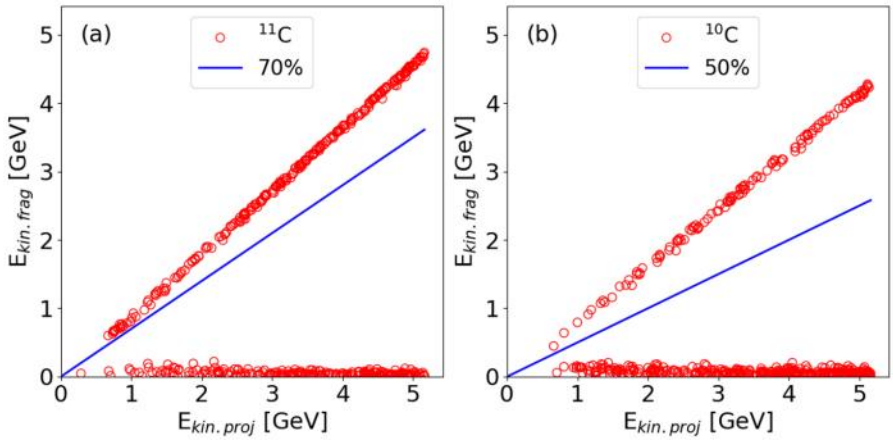

Figure 3.1: Kinetic energy of ^{11}C (a) and ^{10}C (b) fragments produced after the interaction of a ^{12}C-ion with a target nucleus [10]. Below 0.2 GeV, the fragment energy is independent of the projectile energy, corresponding to isotopes generated via target fragmentation (labeled as $^{10}C_{tar}$ and $^{11}C_{tar}$). At higher energies, the fragment kinetic energy scales with that of the ^{12}C-ion, corresponding to projectile fragments (labeled as $^{10}C_{proj}$ and $^{11}C_{proj}$).

3.1.3 IDPED construction

Once PEs included are defined, the next step for the 3D PED calculation is the introduction of the IDPED.

For each PE, the IDPED is obtained by applying a filtering method to the IDD in a reference material, followed by analytical modeling. In [10], the parameters of the modeling functions are derived from MC simulations in the reference material explained in Section (3.1.1).

The filtering approach implemented was originally introduced in [73] for proton therapy and is already described in Section (2.6). For carbon ions, this method was examined but proved to be not able to predict IDPED with different energies [11]. Instead only the distal fall-off position, i.e. the depth at which PED begins to decrease significantly from its maximum, marking the transition from the build-up region to the distal tail, is determined using the convolution method. The rest of PED profile is reconstructed through parametrized functions.

According to [10], the IDPED was modeled separately for target PEs and projectile PEs:

- IDPED of target PEs: as shown in Fig. (3.2) for each isotope type i, the IDPED can be divided into a build-up region b, described by the sum of two exponential terms and a distal region d, modeled with a power-law function dependent on the initial kinetic energy of the beam.

$$\begin{cases} IDPED_{i,b}(E,z) = A_i(1-\alpha_i e^{-c_{1,i}z}) + B_i(e^{c_{2,i}z}-1) \\ IDPED_{i,d}(E,z) = \beta_i E^3 \frac{1}{z^{n_i}} \end{cases} \tag{3.1}$$

In the first equation, the two terms account for different growth behaviors of the distribution:

The first exponential term models a slower build-up, with:

- A_i: theoretical maximum number of produced PEs at large depth for the slow component;
- α_i: fraction determined by the number of PEs at the phantom entrance;
- $c_{1,i}$: build-up rate of the slow component.

The second exponential term compensates for the rapid increase of PE production in the region just before the Bragg peak, with:

- B_i: amplitude determined by the difference between the number of PEs at the end of the build-up predicted by the first term and the corresponding MC simulation result;
- $c_{2,i}$: rate of the rapid growth.

In the second equation, the scaling factor β_i and the power of function n_i depend on the PE subspecies i and they depend on the energy.

The boundary between the two parts is obtained from the distal fall-off positions of the convolved profiles (Eq. 3.1), selecting the value that best matches MC simulated data. Since the distal part begins several millimeters downstream the end of the build-up part, the gap is interpolated linearly.

- IDPED of projectile PEs: the distal limit of the distribution is set to the 80% distal fall-off position of the convolved profiles, while the proximal limit is estimated from the ratio $\frac{A_f}{A_p}$ of the incident primary particle range. A_f is the fragment mass number and A_p is the mass number of the primary ^{12}C-ion. The corresponding range is obtained from the distal fall-off position of the IDD. Fig. (3.3) illustrated the example of the IDPED of $^{11}C_{proj}$ produced by target nuclei in the reference material for energies of 100, 200, 300 and 400 MeV/n .

$$IDPED_{i,proj}(E,z) = [h_i(E) \cdot \Phi_{^{12}C}(z)] * G_i(z) \tag{3.2}$$

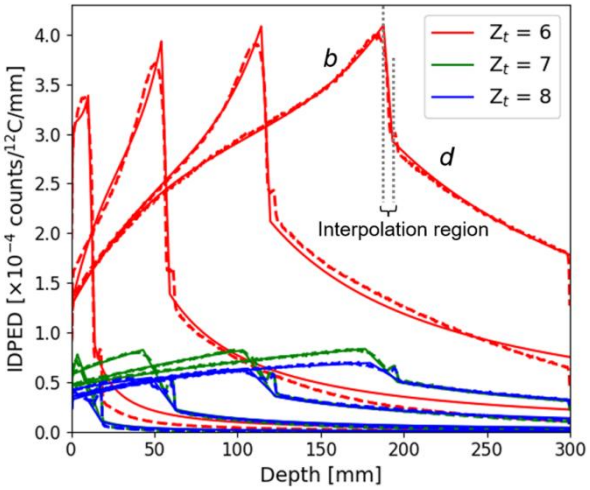

Figure 3.2: IDPED of $^{11}C_{tar}$ produced by C, Ni, O target nuclei in the reference material for energies of 100, 200, 300 and 400 MeV/n [10].

With:

- $h_i(E)$: energy-dependent scaling factor, expressed as a fourth-order polynomial, used to normalize the peak height of the IDPED;
- $\Phi_{^{12}C}(z)$: fluence correction term for ^{12}C-ion;
- $G_i(z)$: Gaussian function accounting for statistical energy loss fluctuations.

For the case of projectile PEs generated on hydrogen targets, the above modeling is not applicable, as these distributions exhibit a longer build-up compared to heavier target nuclei (see Fig (3.3)). In this case, better agreement with MC data is achieved by employing a Landau-based parameterization:

$$IDPED(E,z) = [k(E) \cdot Landau(\mu,\eta)] * G(z) \tag{3.3}$$

With:

- $k(E)$: scaling factor depending on energy, represented as a third-order polynomial;
- μ: position of the maximum of the Landau distribution, determined from the peak position of the convolved profiles P;
- η: width of the Landau distribution, found to scale linearly with the 80% distal fall-off position of the IDD;
- $G(z)$: Gaussian function describing residual fluctuations due to energy straggling.

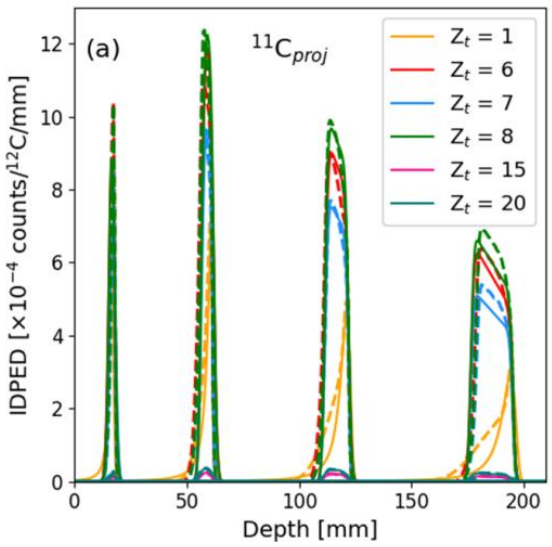

Figure 3.3: IDPED of $^{11}C_{proj}$ produced by target nuclei in the reference material for energies of 100, 200, 300 and 400 MeV/n [10].

3.1.4 Parameterization of lateral distribution

To construct a full 3D parametrization of PED, the approach presented in [10] extends the IDPED modeling described in [11] by explicitly incorporating the lateral distribution of PEs. For projectile PEs, the lateral spread can be accurately modeled by a single Gaussian function, with the depth-dependent σ values fitted from MC simulations (Eq. (3.4) (1)). In contrast, target PEs exhibit a broader off-axis contribution that can not be properly described by a single Gaussian. To address this, a double Gaussian parameterization is adopted, originally proposed in [80] for modeling the lateral dose distribution in particle therapy. While in [80] the double Gaussian accounts for the central dose core and the extended low-dose halo, in [10] the same concept is applied to the lateral distribution of PEs, where σ_1 and σ_2 represent the narrow and broad Gaussian components with relative weights $1 - w$ and w, respectively (Eq. (3.4) (2)).

In order to mitigate statistical fluctuations observed at large radial distances from the beam axis, the fitting region is chosen to enclose 99.75% of the total area in the radius-weighted distribution $r \cdot PED(E, z, r)$. Moreover, the fitted σ values are corrected by quadratically adding the actual entrance beam width, instead of using the fixed reference value of 3 mm. This correction ensures a more accurate description of the lateral tails of PED.

$$\begin{cases} PED(E,z,r) = IDPED(E,z)\frac{1}{2\pi\sigma(E,z)^2}e^{-\frac{r^2}{2\sigma(E,z)^2}} & (1) \\ PED(E,z,r) = IDPED(E,z)\left(\frac{1-w(E,z)}{2\pi\sigma_1(E,z)^2}e^{-\frac{r^2}{2\sigma_1(E,z)^2}} + \frac{w(E,z)}{2\pi\sigma_2(E,z)^2}e^{-\frac{r^2}{2\sigma_2(E,z)^2}}\right) & (2) \end{cases} \tag{3.4}$$

3.1.5 Beam and phantom information

The last input information for the 3D PED framework are the beam and phantom information. Beam information consists of incident direction and position with respect to the phantom, initial nominal energy and beam spot size. Phantom data include mass density, electronic density, mass fractions of elements and mean excitation energy of the material in each voxel. In case of application of this analytical method to clinical scenarios, these information are derived from the corresponding patient CT data and treatment plan files.

3.1.6 Longitudinal heterogeneity effect

Since IDPED and lateral distribution of PEs are calculated in a reference space, a conversion from the penetration depth z in a heterogeneous material to the reference material-equivalent depth $z_{ref,eq}$ is necessary. This step is crucial, as tissue heterogeneities induce variations in density and composition that significantly affect both the energy loss of primary ions and the production of secondary PEs. To address this, in [10] the strategy proposed in [73] is adopted. It consists firstly in the definition of the path-length operator F, which performs the depth conversion:

$$F : z \rightarrow z_{ref,eq} = \int_0^z SPR(z)dz \tag{3.5}$$

Here, $SPR(z)$ is the stopping power ratio between the local medium and the reference material. Physically, this operator ensures that each point in the heterogeneous geometry is mapped into an equivalent position in a homogeneous reference medium, preserving the equivalence in terms of ion energy degradation.

Beyond this geometrical transformation, the material dependence of PE production and stopping must be accounted for. Indeed, target and projectile PEs behave differently:

- For target PEs, since they are produced and stopped essentially at the same position, it is sufficient to introduce a local correction factor $g_j(z)$ to weight the contribution

of different target nuclei [73]. This factor is defined as:

$$g_j(z) = \left[\frac{w_j(z) \cdot \rho(z)}{w_{j,ref} \cdot \rho_{ref}}\right] \tag{3.6}$$

Where $w_j(z)/w_{j,ref}$ is the weight fraction of the target nucleus j at depth z relative to the weight fraction of the same target nucleus in the reference material, and $\rho(z)/\rho_{ref}$ is the mass density of the material at depth z relative to the mass density of the reference material. This correction directly modulates the PE yield in heterogeneous tissues.

- Projectile PEs do not stop in the position where they are produced, thus, a mapping relationship to relate producing position and stopping position is defined. In case of homogeneous material the two positions are related linearly. Assuming that projectile fragments have the same velocity of ^{12}C-ions, the stopping position R_f is defined as:

$$R_f = \frac{A_{proj}}{12} R_0 + \frac{12 - A_{proj}}{12} z \tag{3.7}$$

Where R_0 is the range of the primary ^{12}C-ions and A_{proj} the fragment mass number [11].

This linear relation breaks down in heterogeneous media, where the interplay between composition and density modifies the transport of fragments. To overcome this, the heterogeneous space is first converted into the homogeneous reference space using Eq. (3.5). Then, a new mapping between the production voxels of the PEs and their stopping voxels is established by Eq. (3.7). Finally a scaling factor $\zeta_j(z)$, to consider the material effect on projectile PED at depth z is built as:

$$\zeta_j(z) = a \sum_{m \in I} g_{j,m} \tag{3.8}$$

With $a = K/N$ being the ratio between the stopping interval length and the production interval length in the reference space, and I the set of producing voxels mapped to the voxel at depth z. The scaling factor $\zeta_j(z)$ therefore considers the contribution of produced fragments over multiple producing voxels.

3.1.7 Ray casting technique

At the beginning of Section (3.1.6), the concept of the reference material-equivalent depth $z_{ref,eq}$ is introduced to account for longitudinal heterogeneities. In the proposed PBA, the ray casting method [76, 77] is employed to address lateral heterogeneity effects, by determining the corresponding water-equivalent depth z_{eq} along the beam path.
In practice, for each voxel traversed by the beam, a ray parallel to the central beam axis is traced through the heterogeneous medium. Along this ray, the geometrical path length t_i in each material voxel is converted into a water-equivalent thickness according to the stopping power ratio (SPR) between the local medium and water:

$$t_{eq,i} = t_i \cdot SPR_i \tag{3.9}$$

The water-equivalent depth z_{eq} is then obtained as the cumulative sum of these contributions along the ray:

$$z_{eq} = \sum_i t_i \cdot RSP_i \tag{3.10}$$

This approach effectively replaces the true heterogeneous geometry with an equivalent depth in water that reproduces the same energy loss and scattering conditions. Moreover, as demonstrated in [77], this strategy provides an efficient correction for tissue inhomogeneities without requiring full MC transport, and can be integrated in analytical pencil-beam models with negligible additional computational cost.
In [10], the ray casting procedure is similarly used to compute the reference-material-equivalent depth $z_{ref,eq}$. Unlike the original formulations, $z_{ref,eq}$ is expressed in terms of the chosen reference material instead of water, ensuring consistency with the parameterization of the analytical model based on the MC data in the reference material.

3.1.8 3D PED calculation

Finally, using all the quantities defined in the previous sections the distribution of total PEs in a voxel with its center coordinate (x, y, z) by a single pencil beam with an initial energy E is calculated as:

$$PED(E,x,y,z) = \left(\sum_j \begin{cases} g_j(x,y,z) & \text{if target PE} \\ \zeta_j(x,y,z) & \text{if projectile PE} \end{cases} \cdot IDPED_j(E, z_{ref,eq}) \right) \cdot G(E, z_{ref,eq}, r) \tag{3.11}$$

Where the factors g_j and ζ_j are defined in Eqs. (3.6) and (3.8), respectively. $z_{ref,eq}$ is the reference-material-equivalent depth calculated using the ray casting technique, IDPED is obtained as described in Section (3.1.3), G is the single or double Gaussian for the lateral parameterization as explained in Section (3.1.4) and r is the off-axis distance.

3.2 Validation of the analytical framework for 3D PED prediction

In this thesis work, to validate the analytical framework, a comparison is performed between MC simulated PED and analytical predicted PED under the same setup.
For this purpose, a PMMA (Polymethyl Methacrylate) phantom is employed. PMMA is a widely used tissue-equivalent material, whose composition is reported in Table (3.2). The choice of this material is motivated by the fact that, in the final part of this work, the analytical predictions are compared with experimental measurements carried out in PMMA.

Mass density	1.19 g·cm^{-3}
Electron density	3.87·10^{20}cm^{-3}
Mass abundance	
Hydrogen (H)	8%
Carbon (C)	60%
Oxygen (O)	32%

Table 3.2: Material information of PMMA [10]

The phantom consists of a box with dimensions 200×200×300 mm^3, voxelized with a spatial resolution of 1 mm^3.
The ^{12}C-ion beam is modeled as a mono-energetic and mono-directional pencil beam with $\sigma_0 = 3$ mm, propagating along the z-axis and originating 50 mm upstream of the phantom. The initial nominal kinetic energy is set to 200 MeV/n.
Two separate simulations are performed using the Geant4 toolkit (version 10.07.p04) with

the QGSP_BIC physics list. The first simulation, with $3 \cdot 10^6$ primary particles, is dedicated to dose scoring, while the second, with $1.5 \cdot 10^8$ primaries, is used for PED generation. The isotopes ^{10}C, ^{11}C, ^{13}N, ^{14}O and ^{15}O are scored and recorded.
The dose distribution obtained from the first simulation serves as a key input for the subsequent analytical framework calculations. As a result, the 3D distribution of each PE is derived and then compared with the distributions obtained from the MC simulation.

3.3 PED to activity conversion

Once PED has been obtained by the analytical method described above for each PE type, the next step is to convert this distribution into the activity distribution, in order to compare it with measured PET data (typically the averaged activity or the total number of decay distribution within a certain time frame of measurement).
In [10], a larger set of isotopes is included in PED calculation compared to [11], allowing validation against both off-line and in-beam PET measurements. This study focuses on in-beam PET measured data, thus a conversion method from PED to in-beam PET signal is presented.
This approach is based on the methodology described in [66], adapted for CIRT applications.
The activity conversion method recursively calculates the number and spatial distribution of the total decays of each PE type in every irradiation phase. The pulsed irradiation is divided into cycles, each consisting of: a beam-on phase, during which the beam is active and PEs are continuously produced, and a beam-off phase, during which only decay processes occur.
The following assumptions are adopted, consistent with previous analytical models [66, 73, 81]:

- The annihilation position coincides with the location where the PEs come to rest.
- A β^+-decay branching ratio of 100% is assumed.
- The activity conversion method neglects temporal fluctuations in beam energy, position, and intensity during beam-on phases.
- A constant PE production rate K_j during the beam-on phases is assumed:

$$K_j = \frac{PE_j}{t_f - t_i} \tag{3.12}$$

Where PE_j is the total number of isotope j generated during the beam on-phase, and t_i, t_f are the start and end time. Initially, the number of PEs in the phantom is zero, and since the analytical framework provides the number of each PE produced per primary particle, PE_j is obtained by multiplying this value by the number of primaries delivered during this beam-on phase.

- For phantoms, biological washout effects occurring in living tissues are not considered, so that only the physical decay is modeled.

The PET distribution (i.e. the total number of β^+ decay) is calculated as followed:

1. Compute the activity as a function of time for each isotope in each phase, using its specific decay constant;

2. Integrate the activity over the phase duration to compute the 3D decay distribution for each isotope;

3. Sum the decay distributions of all isotopes to obtain the total 3D PET distribution.

Section (3.3.1) and Section (3.3.2) present the formulas used for the activity and decays calculation in a PMMA phantom, respectively. The required input data include: (a) total number of beam primaries; (b) total number of each PE type per primary; (c) 3D PED for each isotope; (d) half-life and physical decay constant for each PE. The latter are reported in Table (3.3).

PE	**Half-life** $T_{1/2}$ **[s]**	**Physical decay constant** λ_{phys} **[1/s]**
^{10}C	19.29	$3.59 \cdot 10^{-2}$
^{11}C	1221.8	$5.67 \cdot 10^{-4}$
^{14}O	70.606	$9.82 \cdot 10^{-3}$
^{15}O	122.24	$5.67 \cdot 10^{-3}$
^{13}N	597.50	$1.16 \cdot 10^{-3}$

Table 3.3: PEs, half-life and physical decay constant values [82].

3.3.1 Activity calculation

For the irradiation of a PMMA phantom, only physical decay processes are considered, as no biological effects occur [7]. The activity $A_j(t)$ for each isotope j is calculated using the expressions in Eq. (3.13), where beam-on and beam-off phases are treated separately. In the beam-on phase, the formula takes into account both decay and continuous PE production, while the beam-off phase includes only the decay term, consistent with previous analytical approaches [66, 81].

$$\begin{cases} A_j(t) = A_j(t_i)e^{-\lambda_{phys,j}(t-t_i)} + \frac{PE_j}{t_f - t_i}(1 - e^{-\lambda_{phys,j}(t-t_i)}) & (1) \\ A_j(t) = A_j(t_i)e^{-\lambda_{phys,j}(t-t_i)} & (2) \end{cases} \tag{3.13}$$

Where:

- j denotes the isotope species;
- t_i and t_f are the initial and final time of each phase, respectively (with t_i of one phase corresponding to t_f of the previous one);
- $A_j(t_i)$ is the residual activity at the beginning of the current phase (equal to the activity at t_f of the previous phase);
- In (1), the first term represents the decay of pre-existing PEs, while the second term accounts for their production during the beam-on phase, assuming a constant production rate as defined in Eq. (3.12).

In this way the conversion method supports different PEDs for different beam-on phases if beam characteristics vary.

The total activity is given by the sum of the activity calculated for each PE isotope type.

3.3.2 3D decay distribution calculation

The 3D decay distribution for each isotope is then obtained by integrating its activity between t_i and t_f for each phase. These assumptions follow the methodology proposed in [66] and extended in [81] for analytical PET prediction:

$$D_j(t_i, t_f; x, y, z) = \int_{t_i}^{t_f} A_j(t)\, dt \tag{3.14}$$

The decay distributions for beam-on and beam-off phases are expressed as:

- Beam-on phase. Since in Eq. (3.13) (1) has two terms the integral calculation is

divided into two integrals:

$$\int_{t_i}^{t_f} A_j(t_i) e^{-\lambda_{phys,j}(t-t_i)}\, dt \;=\; A_j(t_i) \frac{1 \,-\, e^{-\lambda_{phys,j}(t_f - t_i)}}{\lambda_{phys,j}} \tag{3.15}$$

$$\int_{t_i}^{t_f} \frac{PED_j(x,y,z)}{t_f \,-\, t_i} (1 - e^{-\lambda_{phys,j}(t-t_f)})\, dt \;=\; \frac{PED_j(x,y,z)}{t_f \,-\, t_i} \left[(t_f \,-\, t_i) \,-\, \frac{1 \,-\, e^{-\lambda_{phys,j}(t_f - t_i)}}{\lambda_{phys,j}} \right] \tag{3.16}$$

So that the total decay distribution is given by the sum of the results obtained in Eqs. (3.15) and (3.16).

- Beam-off phase. No PE production occurs and the integral simplifies to:

$$D_j(t_i, t_f; x, y, z) \;=\; \int_{t_i}^{t_f} A_j(t_i) e^{-\lambda_{phys,j}(t-t_i)}\, dt \;=\; A_j(t_i) \frac{1 \,-\, e^{-\lambda_{phys,j}(t_f - t_i)}}{\lambda_{phys,j}} \tag{3.17}$$

3.4 Comparison between measured PET signal and predicted activity distribution

3.4.1 Experimental setup

Experimental PET data used for the validation of the 3D analytical approach described in Section (3.1) were provided by the Japanese National Institutes for Quantum Science and Technology (QST) and acquired with the SROP system presented in Section (2.4.4). The irradiated phantom was a PMMA box with dimensions 150 mm (bed direction) × 90 mm (height) × 150 mm (beam direction). It was positioned in the scanner FOV with the beam aligned along the z-axis. The isocenter was located at (75 cm, 55 cm, 55 cm) with respect to the bottom surface of the phantom. The geometry setup in side, beam's eye, and top views is reported in Fig. (3.4).

Six irradiation cases were performed. The beam used was a mono-energetic and mono-directional ^{12}C-ion pencil beam with initial nominal energy $E = 255.7$ MeV/n. The phantom was irradiated with a single spill and the *mesh2* ripple filter was applied in the beamline.

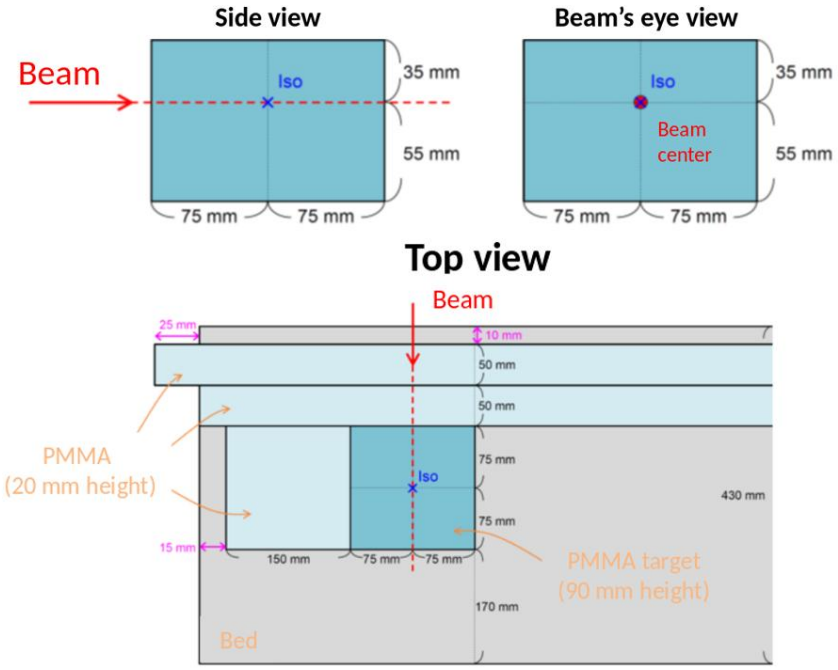

Figure 3.4: Geometry setup in side, beam's eye, and top views.

The *mesh2* ripple filter is an aluminum mesh that broadens the Bragg peak of a mono-energetic beam longitudinally, following a normal distribution characterized by a mean water-equivalent thickness t and a standard deviation σ. In this experimental setup, $t = 5.4$ mm and $\sigma = 1.5$ mm [83].

A summary of the beam parameters for the six cases is reported in Tab. (3.4).

The "Un-scanned" configuration corresponds to irradiation with a single pencil beam (spot), while in the other cases multiple spots were used, producing a square irradiation field of the specified dimensions.

Beam parameters	**Nb particles**	**Beam-on time [ms]**
Un-scanned 1.5 Gy	$7 \cdot 10^6$	16
Un-scanned 1.5 Gy	$1 \cdot 10^7$	34
2x2 cm^2 1.5 Gy	$9 \cdot 10^7$	213
2x2 cm^2 3 Gy	$1 \cdot 10^9$	426
4x4 cm^2 1.5 Gy	$3 \cdot 10^8$	777
4x4 cm^2 3 Gy	$6 \cdot 10^8$	1553

Table 3.4: Beam parameters

The PET measurement started immediately after the end of the irradiation, until 600 s. In the end, the PET images were reconstructed for three different time frames: 0-60 s, 0-600 s, and 300-600 s.

Image reconstruction was performed using list-mode MAPED (MEdian root prior) with 80 iterations. The reconstructed 3D image size was (540 × 480 × 480) voxels with an isotropic voxel size of 1.5 mm.

Fig. (3.5) shows the IDD profile of the irradiated ^{12}C-ion pencil beam, expressed in arbitrary units, calculated in PMMA using a MC simulation and provided by QST.

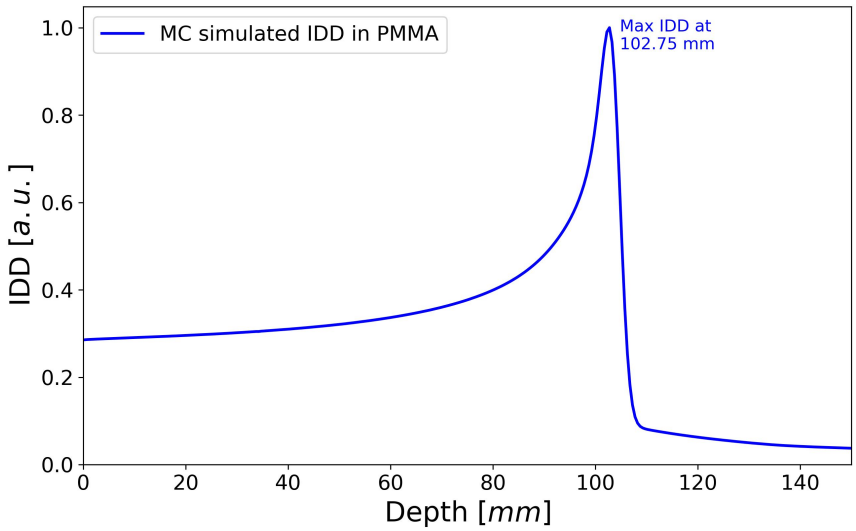

Figure 3.5: MC simulated IDD (from QST) in PMMA from a ^{12}C-ion pencil beam with an initial nominal energy of 255.7 MeV/n.

3.4.2 Predicted activity distribution calculation

As the IDD, provided by QST, was simulated in PMMA, while the analytical approach requires dose in the reference material, a depth conversion is performed. The depth axis is rescaled by integrating the SPR along the measured depth, producing an equivalent depth in the reference material (see Fig. 3.6). The SPR is calculated as:

$$SPR = \frac{ln\left(\frac{2m_e c^2 \beta^2 \gamma^2}{I_{PMMA}}\right) - \beta^2}{ln\left(\frac{2m_e c^2 \beta^2 \gamma^2}{I_{ref}}\right) - \beta^2} \cdot \frac{\rho_{e,PMMA}}{\rho_{e,ref}} \tag{3.18}$$

Where β and γ are the relativistic parameters of the incident particle, I is the mean excitation energy and ρ_e is the electron density.

Moreover, the presence of the ripple filter along the beam path reduces the initial beam energy and modulates the particle range, resulting in a shallower and broader Bragg peak. To account for this effect in the analytical calculation, a range modulation procedure is applied as follows.

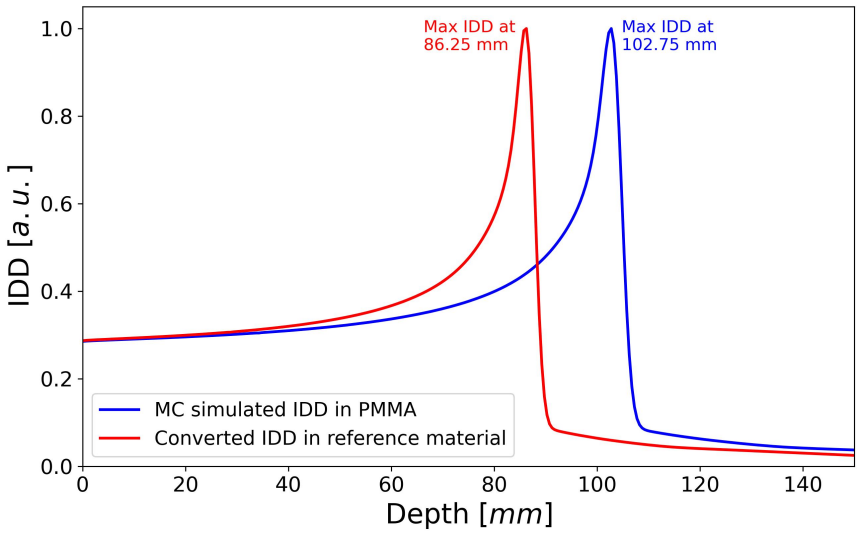

Figure 3.6: IDDs in PMMA and in the reference material after conversion from a ^{12}C-ion pencil beam with an initial nominal energy of 255.7 MeV/n. The blue and red lines represent the MC simulated IDD in PMMA (from QST) and the IDD in reference material, respectively.

Starting from a previously validated mono-energetic IDD in the reference material, a series of IDDs shifted in depth by 0.5 mm increments to the left is generated, until the position of the rising edge of the QST IDD is reached. By fitting the QST IDD, the weights of the shifted IDDs are determined so that their superposition reproduces the QST IDD. These weights are then normalized so that their sum equals 1.

The validated IDD curve was obtained by MC simulation using a mono-energetic ^{12}C-ion pencil beam with an initial nominal energy of 250 MeV/n. In Fig. (3.7) the normalized QST IDD and the normalized validated IDD in reference material are shown, together with the 22 shifted curves. Based on the preliminary fitting result, the 22 shifted IDDs are further reduced to 11 curves with shifts from 1 mm to 6.5 mm, excluding the curves with negligible weights. The weights corresponding to the 11 shifted curves used for the fit are reported in Table (3.5). Fig. (3.8) shows that the reconstructed curve obtained as the weighted sum of the shifted curves matches the QST IDD with very good agreement.

Shifted Curves	**Weights**	**shifted curves**	**Weights**
Curve 0	0.0659	Curve 6	0.1511
Curve 1	0.0285	Curve 7	0.0887
Curve 2	0.1205	Curve 8	0.0787
Curve 3	0.1052	Curve 9	0.0235
Curve 4	0.1698	Curve 10	0.0323
Curve 5	0.1358		

Table 3.5: Weights of the shifted curve obtained from the fitting process.

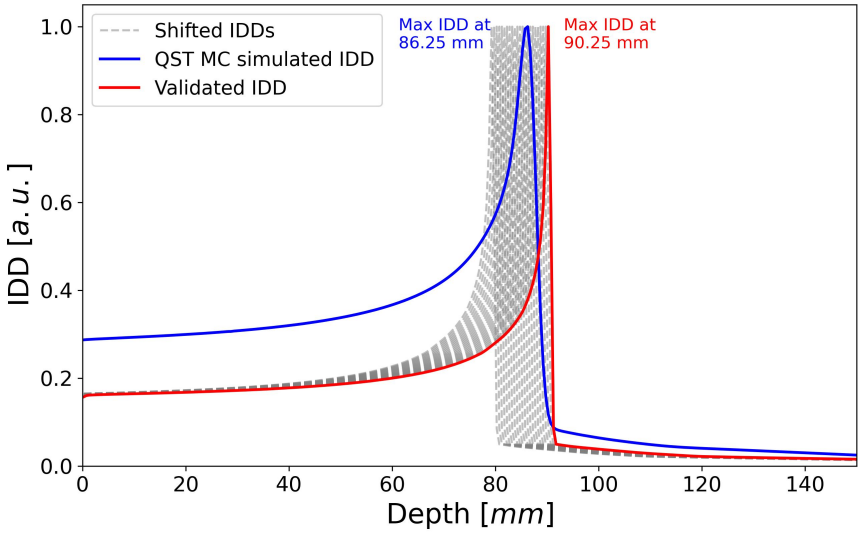

Figure 3.7: Normalized IDDs in the reference material. The blue line represents the QST IDD curve obtained from a ^{12}C-ion pencil beam with an initial nominal energy of 255.7 MeV/n, with the ripple filter effect applied. The red line represents the validated IDD curve obtained from a ^{12}C-ion pencil beam with an initial nominal energy of 250 MeV/n. The dashed lines represent the shifted curves, generated from the validated IDD curve with a step size of 0.5 mm.

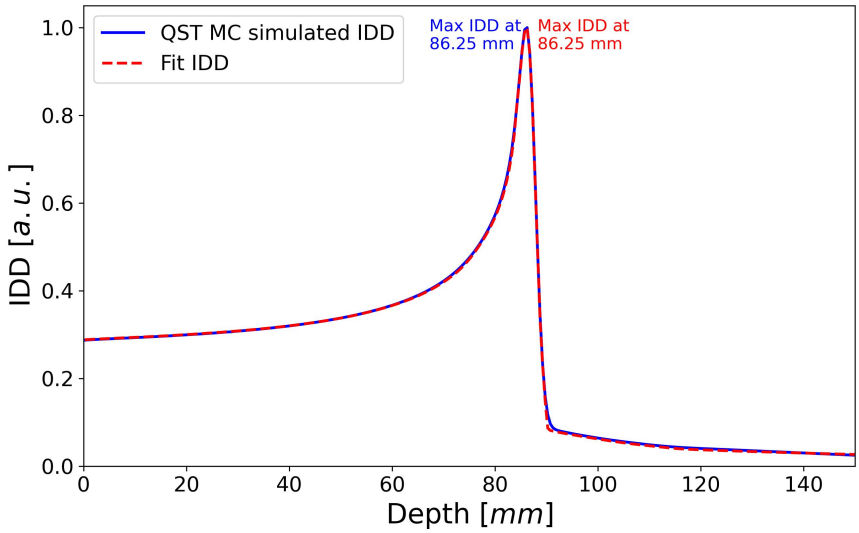

Figure 3.8: Normalized IDDs in the reference material. The blue line represents the QST IDD curve obtained from a ^{12}C-ion pencil beam with an initial nominal energy of 255.7 MeV/n, with the ripple filter applied. The red dashed line represents the normalized reconstructed IDD curve obtained from the fitting process.

Once the shifted IDDs and their weights are obtained, the PED corresponding to each IDD is calculated by the analytical approach. To reconstruct the distribution corresponding to the QST IDD, these PEDs are summed according to their respective weights. The input parameters for the analytical method, along with those used for the IDD conversion, are summarized in Table 3.6.

After obtaining the PED using the analytical framework, the 3D decay distribution is calculated for each scenario. Finally, a Gaussian filter with the FWHM of 7 mm is applied

Material characteristics			
	Water	Reference Material	PMMA *
Mean excitation energy [eV]	78	88.48	74.66
Electron density [10^{20}cm^{-3}]	3.34	4.7134	3.19
Phantom characteristics			
Nb of voxels (x-axis)	Nb of voxels (y-axis)	Nb of voxels (z-axis)	Voxel size [mm]
150	90	150	1
Beam characteristics			
Initial energy [MeV/n]	Position	Initial size [mm]	Div. coef. in air
255.7	(75, 55, 0)	2.625 **	0.00333 ***

Table 3.6: Input parameters.
* The SPR = 1.165 relative to water used to calculate the mean excitation energy for PMMA was experimentally measured.
** The initial beam size used in the code for both x and y directions is obtained as the average of experimental σ_x and σ_y at the entrance surface (75 mm upstream of the isocenter).
*** The beam divergence coefficient in air used in the code is calculated starting from the experimental values.

to account for the spatial resolution of the PET scanner, and the signal is converted to counts/ml.

To reproduce the Un-scanned case, the activity distribution calculation is performed directly on PED obtained from the single pencil beam. For the 2×2 cm^2 and 4×4 cm^2 irradiation field cases, however, the spot PED is first shifted and summed to generate the multiple-spot configurations, and the activity calculation is then applied.

4

Results and Discussion

4.1 Comparison of MC simulated PED and analytically predicted PED

In this section, a comparison between PED in a PMMA phantom obtained from MC simulations and calculated using the analytical framework described in Section (3.2) is presented.

Fig. (4.1) shows the MC simulated IDPED and the analytically predicted IDPED for total PEs, together with the simulated IDD in PMMA originating from a ^{12}C-ion pencil beam with an initial nominal energy of 200 MeV/n. In Fig. (4.2) the MC simulated IDPED and the analytically predicted IDPED for separate PEs are illustrated.

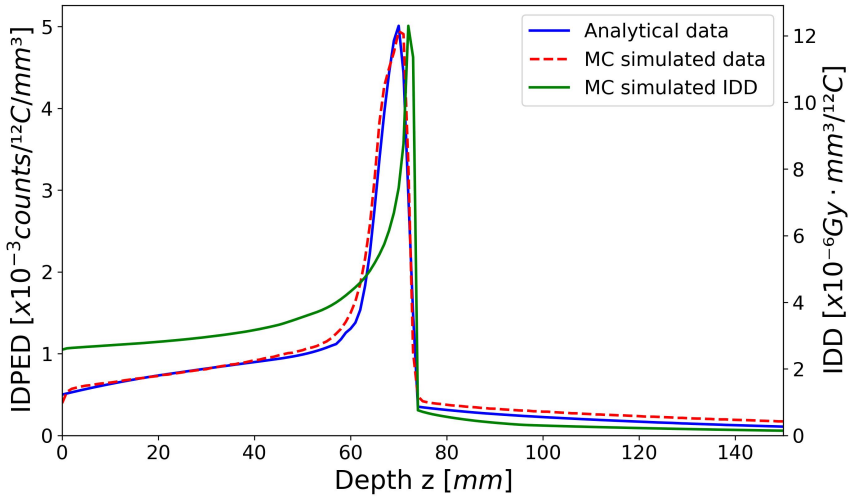

Figure 4.1: IDPED for total PEs from a ^{12}C-ion pencil beam with an initial nominal energy of 200 MeV/n in a PMMA phantom. The blue line represents the analytically predicted IDPED, the red dashed line the MC simulated IDPED and the green line the MC simulated IDD.

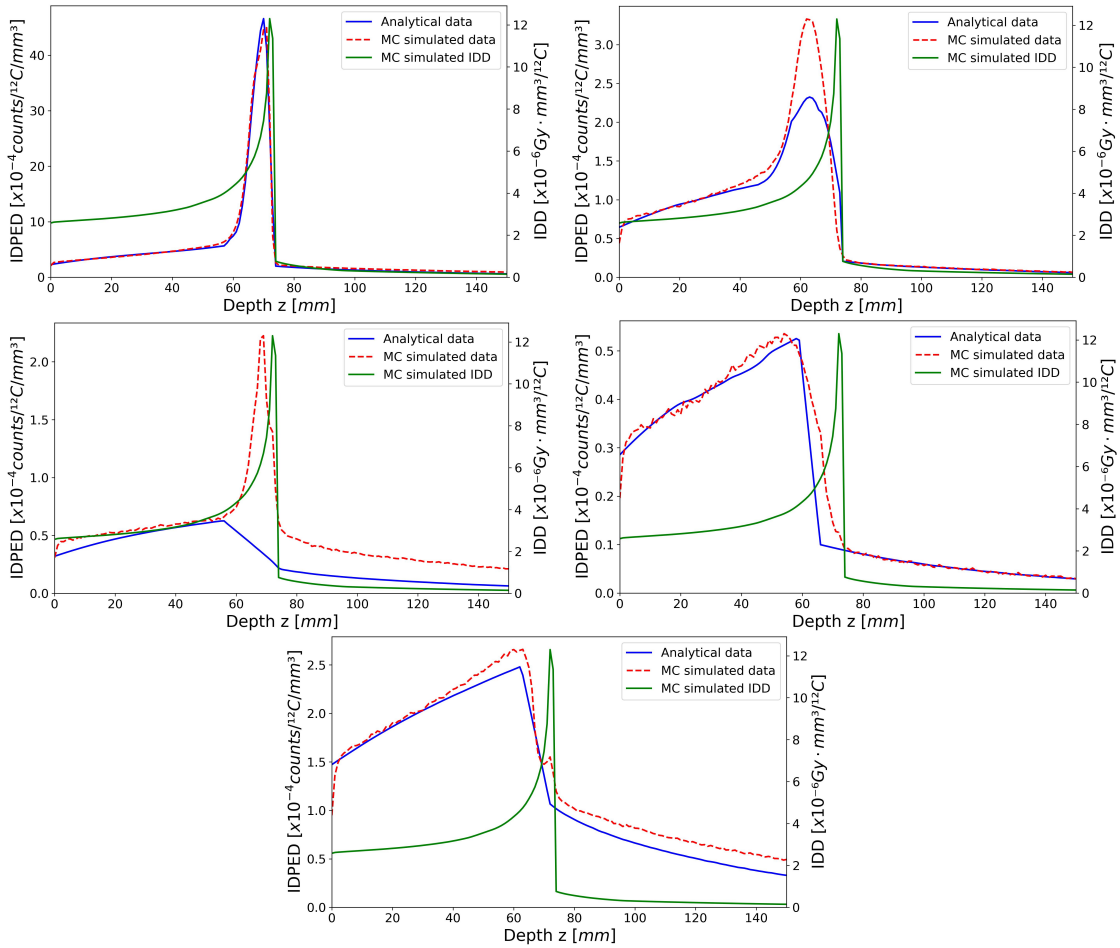

Figure 4.2: IDPED for separate PEs from a ^{12}C-ion pencil beam with an initial nominal energy of 200 Mev/n in a PMMA phantom. Shown, in order from top to bottom and from left to right, are the ^{11}C, ^{10}C, ^{13}N, ^{14}O, and ^{15}O isotopes. The blue line represents the analytically predicted IDPED, the red dashed line the MC simulated IDPED and the green line the MC simulated IDD.

The differences between MC simulated IDPED and total analytically predicted IDPED for total PEs were quantified using the normalized root mean square error (NRMSE):

$$NMRSE = \frac{1}{max_{MC} - min_{MC}} \sqrt{\frac{1}{N} \sum_{i=1}^{N} (y_i - \widehat{y}_i)^2} \tag{4.1}$$

where $max_{MC} - min_{MC}$ is the difference between the maximum and minimum values of the MC simulated IDPED, N is the total number of sampled points, and y_i and $\widehat{y}_i$ are the MC simulated and analytically predicted IDPED values, respectively. The NRMSE was computed using uniformly sampled data points, corresponding to one voxel (1 mm) along the beam axis. This sampling resolution was kept consistent for both datasets and may slightly influence the resulting NRMSE value, especially in regions with steep gradients. The computed NRMSE value is 0.0178.

The range for both cases was estimated using the distal positions corresponding to 20%

and 80% of the maximum PED, referred to as the R20 and R80 values, respectively. The peak position was obtained directly from the original data sampled at a 1 mm voxel size, whereas the R20 and R80 depths were determined after linear interpolation and resampling with a finer bin size of 0.01 mm to improve the accuracy in locating the corresponding depth positions. The associated uncertainties were taken as ±0.5 mm for the peak position (half of the voxel size) and ±0.01 mm for R20 and R80 (interpolation step). For the differences between analytical and simulated values, the uncertainties were propagated in quadrature.

Table (4.1) summarizes the resulting peak, R20, and R80 values for both the total MC simulated and analytically predicted IDPED distributions.

	MC simulated IDPED	**Analytical predicted IDPED**	**Δ value**
Peak position [mm]	70.0 ± 0.5	70.0 ± 0.5	0.0 ± 0.7
R20 value [mm]	73.05 ± 0.01	73.42 ± 0.01	0.38 ± 0.01
R80 value [mm]	71.61 ± 0.01	71.29 ± 0.01	0.32 ± 0.01

Table 4.1: Peak position, R20 and R80 values for MC simulated and analytically predicted IDPED for a ^{12}C-ion pencil beam with an initial nominal energy of 200 MeV/n in a PMMA phantom. Reported uncertainties correspond to ±0.5 mm (half-voxel) for the peak position and ±0.01 mm (interpolation step) for R20 and R80.

These values indicate that the analytically predicted IDPED profile for total PEs is in good agreement with the simulated one, in terms of both distal fall-off position and amplitude. This consistency supports the accuracy of the IDPED prediction by the analytical approach.

Fig. (4.3) (left) shows the 2D PED obtained from the MC simulation, and in the right figure, the analytically calculated 2D PED is presented. Both distributions are illustrated on the y-z plane containing the central beam axis.

A quantitative comparison between the two distributions is performed using the 3D global gamma index analysis. This method simultaneously evaluates both the relative differences in PE values and the spatial distance-to-agreement. For each point in the analytical PED, the corresponding point in the reference MC PED is considered acceptable if the gamma value is below unity, meaning that both the relative difference and spatial deviation fall within the predefined tolerances. In this study, a 10% maximum threshold is

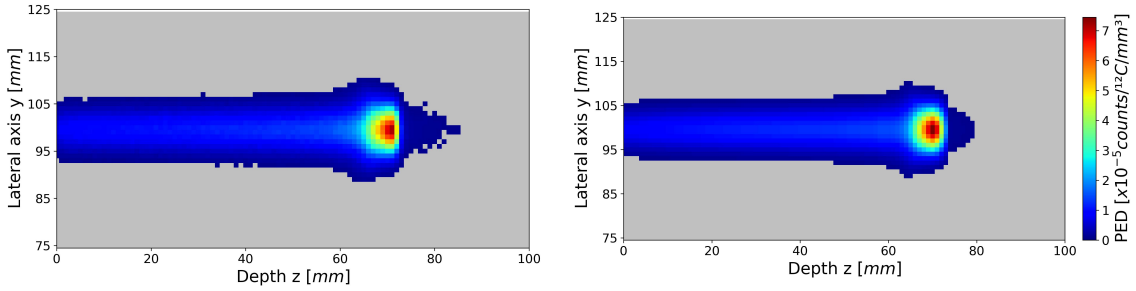

Figure 4.3: 2D PED on the y-z plane containing the central beam axis for a ^{12}C-ion pencil beam with an initial nominal energy of 200 MeV/n in a PMMA phantom. The left plot represents the MC simulated PED, and the right plot the analytically predicted PED. For visualization purposes, values below $1 \cdot 10^{-6}$ were not displayed (threshold applied).

applied, so that only points with an intensity greater than 10% of the maximum value are included. Two sets of acceptance criteria are employed: 2%/2 mm and 1%/1 mm. Using the 2%/2 mm and 1%/1 mm criteria, passing rates of 99.80% and 98.13%, respectively, were obtained, indicating very good agreement between the MC simulated and analytically predicted PEDs.

The corresponding gamma index maps are shown in Fig. (4.4), with the left panel representing the 2%/2 mm case and the right panel the 1%/1 mm case.

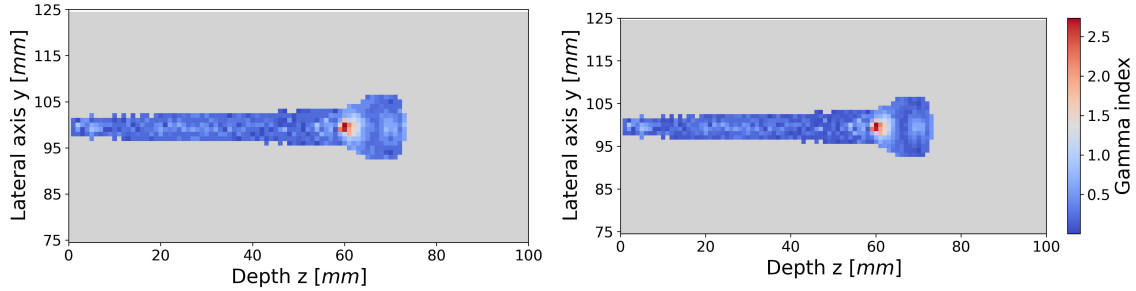

Figure 4.4: Global gamma index maps on the y-z plane containing the central beam axis. The left plot corresponds to the 2%/2 mm criterion, and the right plot to the 1%/1 mm criterion.

The lateral profiles of the MC simulated and analytically predicted PEDs are shown in Fig. (4.5) on a semi-logarithmic scale at different depths. At shallow depths, the PED is mainly composed of target PEs, and its lateral distribution can be described as a combination of narrow and broad Gaussian components. At greater depths, the total PED is predominantly consisting of projectile PE.

In summary, the analytically predicted PED is in good agreement with the MC simulated PED, indicating that the analytical model provides a consistent description within the PMMA phantom.

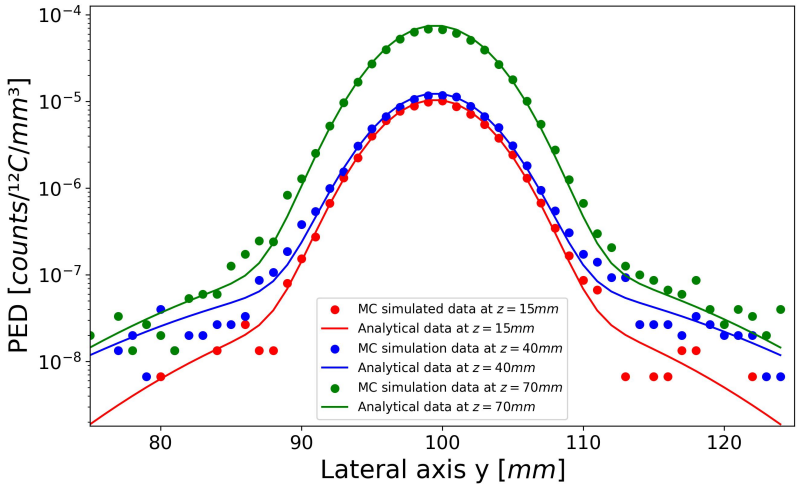

Figure 4.5: Lateral profiles of MC simulated (dots) and analytically predicted (lines) PEDs on a semi-logarithmic scale at depths of 15 mm (red), 40 mm (blue), and 70 mm (green).

4.2 Measured PET signal and analytically predicted activity distributions

In this section, the comparison between the PET signals measured at QST and the analytically predicted activity distributions for a ^{12}C-ion beam with an initial nominal energy of 255.7 MeV/n in a PMMA phantom is presented.

Fig. (4.6) shows the 2D PED analytically calculated on the y-z plane containing the central beam axis, and Fig. (4.7) the corresponding analytically predicted IDPED together with the MC simulated IDD in PMMA, which was provided by QST.

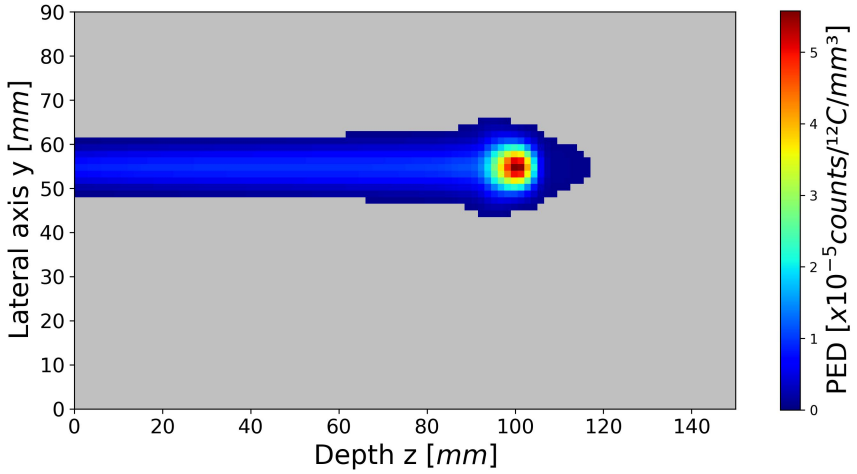

Figure 4.6: 2D analytically calculated PED on the y-z plane containing the central beam axis for a ^{12}C-ion pencil beam with an initial nominal energy of 255.7 MeV/n in a PMMA phantom.

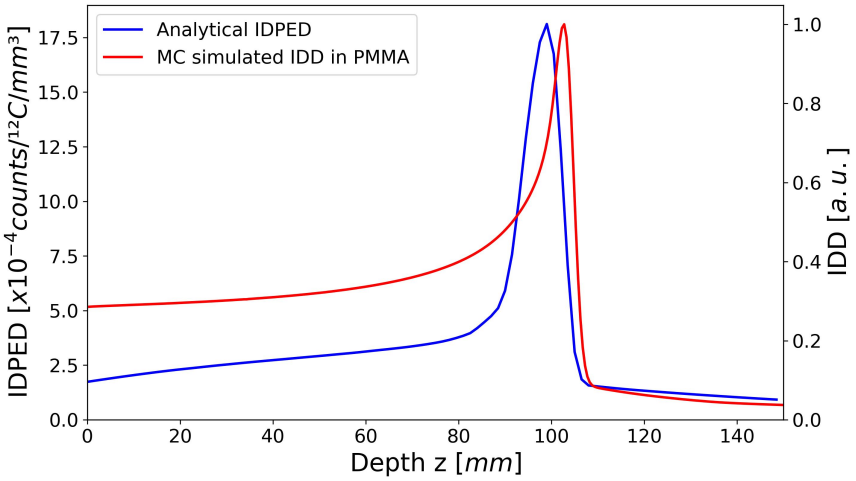

Figure 4.7: IDPED for total PEs from a ^{12}C-ion pencil beam with an initial nominal energy of 255.7 MeV/n in a PMMA phantom. The blue line represents the analytically predicted IDPED, while the red line represents the MC simulated IDD from QST.

When comparing the predicted longitudinally integrated activity distributions for the 0-60 s time frame with measured data, the predicted activity distributions were found to be overestimated in both the 1.5 Gy and 3 Gy delivered-dose cases (see Appendix A). Since, in this early time frame, the signal is mainly dominated by the decay of ^{10}C and ^{15}O, scaling factors of 0.67 and 0.5, respectively, were applied to these PEs to correct for this discrepancy. The activity distributions presented in the following were analytically calculated from the total PED after applying these two scaling factors.

Figs. (4.8), (4.9), and (4.10) show the 2D measured and the analytically predicted activity distributions on the y-z plane containing the central beam axis for the single spot, 2×2 cm^2, and 4×4 cm^2 irradiation field configurations, respectively, with a delivered dose of 3 Gy. The results are presented for the three different time frames after the end of irradiation: 0-60 s, 0-600 s, and 300-600 s. The signal is expressed in counts/ml.
The results for the 1.5 Gy cases are illustrated in Appendix B.

In Fig. (4.11), the integrated longitudinal profiles of the measured and analytically predicted activity distributions are shown for the single spot, 2×2 cm^2, and 4×4 cm^2 irradiation field configurations, with a delivered dose of 3 Gy. Tables (4.2), (4.3), and (4.4) report the peak positions ans R80 values, as well as the total NRMSE values and the NRMSE values relative to the integrated longitudinal profile for each case.
The peak positions were obtained directly from the original data sampled at a voxel size of

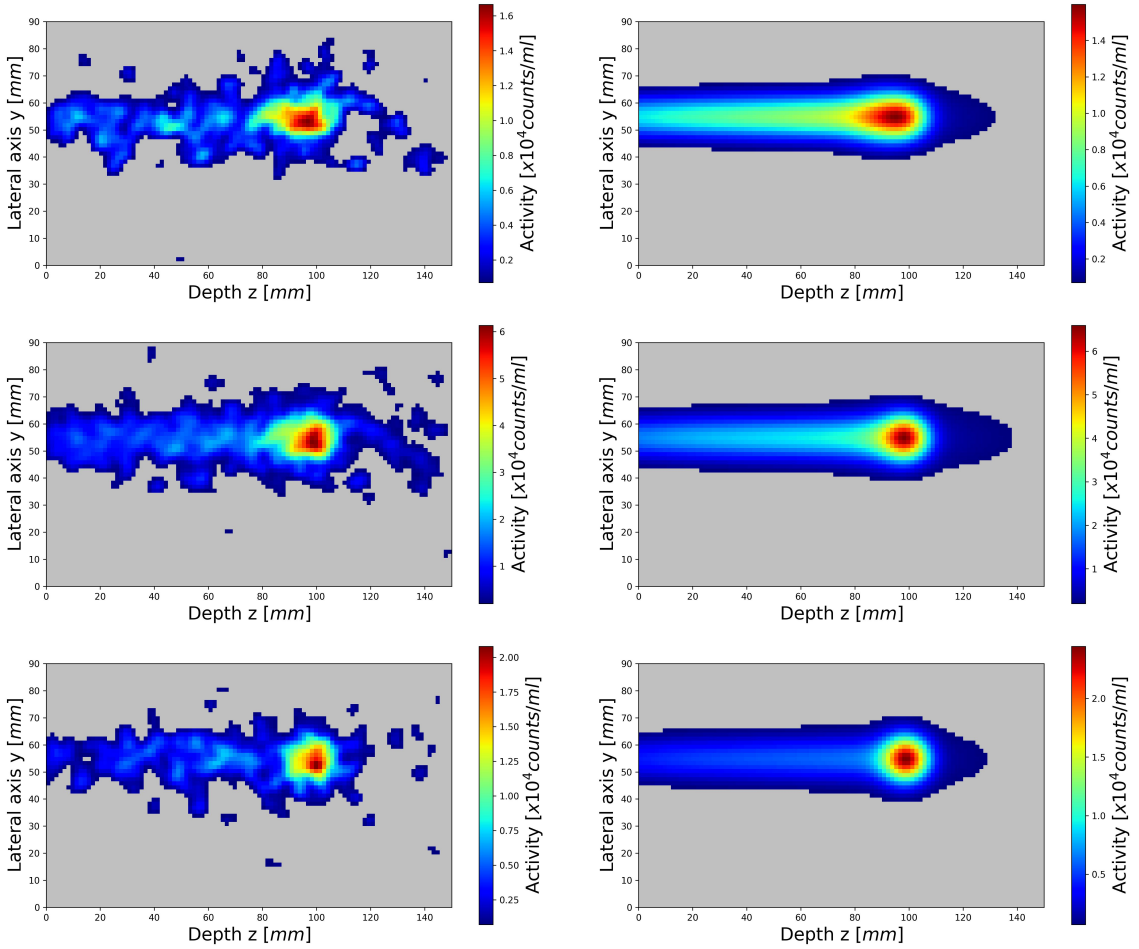

Figure 4.8: 2D measured and analytically predicted activity distributions for the single spot configuration with a delivered dose of 3 Gy. Results are shown on the y-z plane containing the central beam axis for the three time frames after the end of irradiation: 0-60 s (top), 0-600 s (middle), and 300-600 s (bottom). Measured activity distributions are shown on the left, and analytically predicted distributions are shown on the right. The signal is expressed in counts/ml.

1.5 mm, leading to an uncertainty of ± 0.75 mm, corresponding to half the voxel dimension and thus reflecting the intrinsic spatial resolution of the dataset. The R80 values were determined after applying a linear interpolation and resampling with a finer bin size of 0.01 mm to estimate the sub-voxel depth position corresponding to 80% of the maximum activity. However, since the experimental data cannot achieve a precision better than the voxel resolution, the same overall uncertainty of ± 0.75 mm was assigned to the R80 values. For comparisons between measured and analytically predicted distributions, uncertainties were propagated in quadrature, resulting in a combined uncertainty of ± 1.06 mm for the differences in peak and R80 positions. The R20 values were not reported, as the higher noise level in the distal regions of the measured data prevented a reliable determination.

The analytically calculated integrated longitudinal activity profiles for individual PE

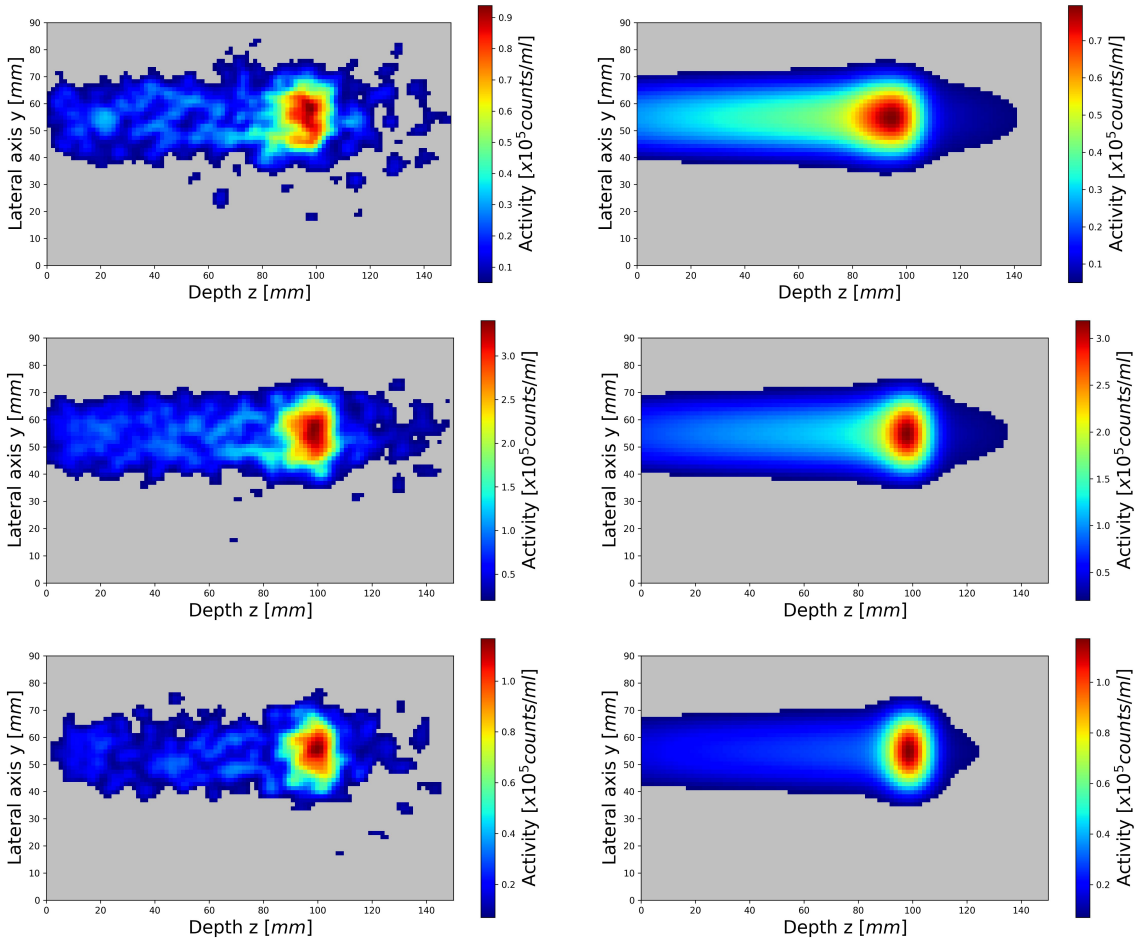

Figure 4.9: 2D measured and analytically predicted activity distributions for the 2×2 cm^2 irradiation field configuration with a delivered dose of 3 Gy. Results are shown on the y-z plane containing the central beam axis for the three time frames after the end of irradiation: 0-60 s (top), 0-600 s (middle), and 300-600 s (bottom). Measured activity distributions are shown on the left, and analytically predicted distributions are shown on the right. The signal is expressed in counts/ml.

are shown in Fig. (4.12). These profiles indicate that, in the 0-60 s time frame after the end of irradiation, the signal is dominated by the decay of ^{10}C and ^{15}O, which are PEs with the shortest half-lives. In contrast, in the 0-600 s time frame, their contribution decreases while the contribution from ^{11}C decay increases, becoming the dominant source of activity also in the 300-600 s time frame after irradiation.

Finally, Fig. (4.13) shows the lateral activity distributions at fixed depths for the single spot, 2×2 cm^2, and 4×4 cm^2 irradiation field configurations, respectively, with a delivered dose of 3 Gy.

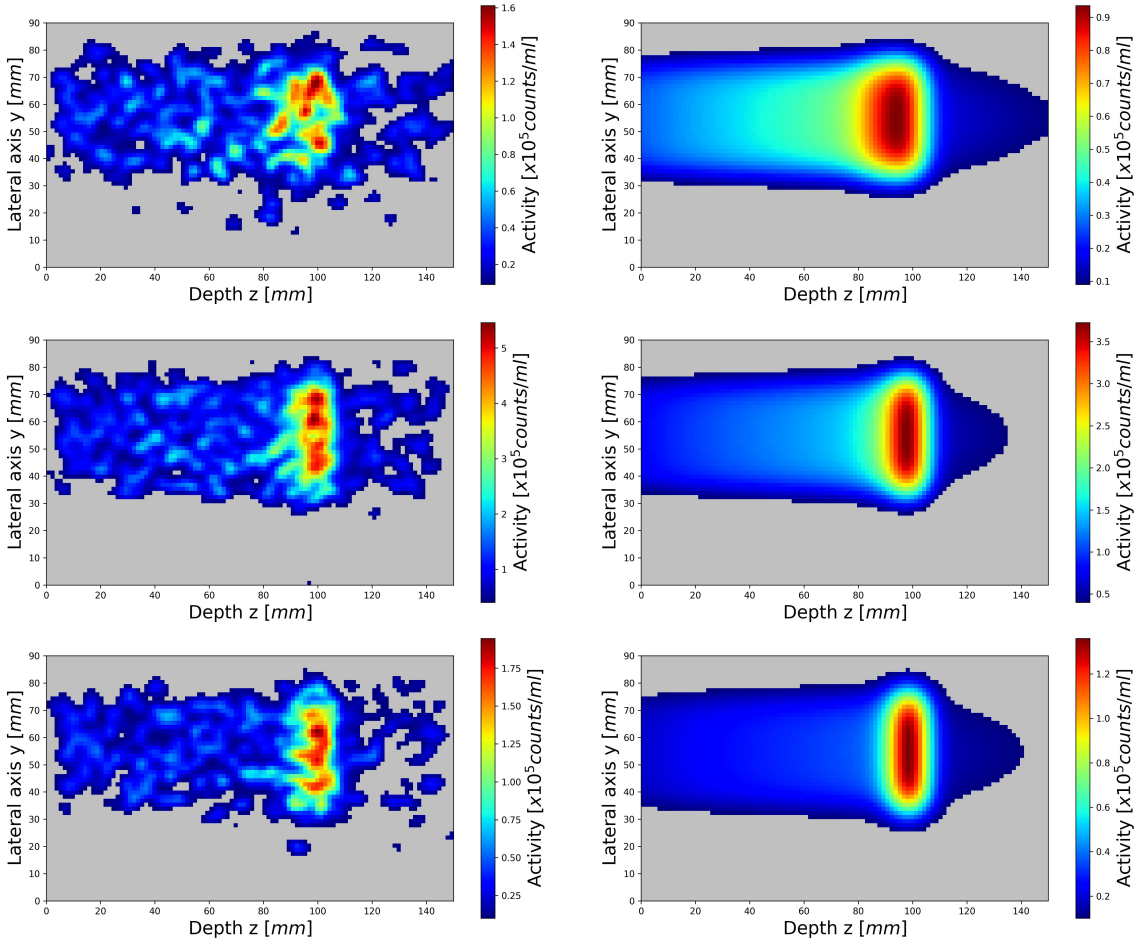

Figure 4.10: 2D measured and analytically predicted activity distributions for the 4x4 cm^2 irradiation field configuration with a delivered dose of 3 Gy. Results are shown on the y-z plane containing the central beam axis for the three time frames after the end of irradiation: 0-60 s (top), 0-600 s (middle), and 300-600 s (bottom). Measured activity distributions are shown on the left, and analytically predicted distributions are shown on the right. The signal is expressed in counts/ml.

4.3 Discussion

A first consistency check with MC simulations presented in Section (4.1) shows that the analytically predicted IDPED for total PEs reproduces the peak positions and amplitudes with minimal deviations in both the distal fall-off and lateral spread. As the analytical model was parameterized based on the Geant4 simulations, these results primarily demonstrate its internal consistency. Moreover, the observed trends are consistent with those reported in [10] where the model was originally introduced.

Next, the validation with in-beam PET measurement data was performed.

For the single spot cases, the analytical model closely reproduced the measured longitudinal and lateral activity profiles, with more pronounced discrepancies in the proximal region and in the earliest time frame (0-60 s after irradiation). These deviations are pri-

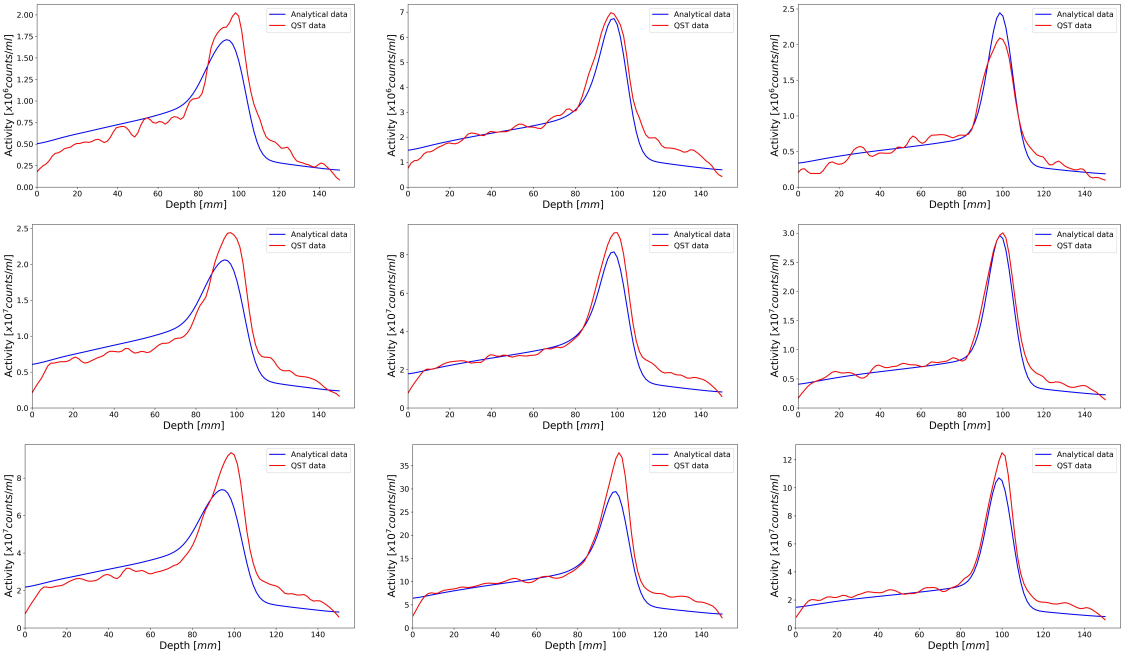

Figure 4.11: Integrated longitudinal activity profiles for the single spot (top), 2×2 cm^2 (middle), and 4×4 cm^2 (bottom) irradiation field configurations, with a delivered dose of 3 Gy. From left to right, the profiles correspond to time frames 0-60 s, 0-600 s, and 300-600 s after the end of irradiation. The blue line represents the analytically predicted activity profile, while the red line represents the measured profile.

marily associated with the short-lived isotopes ^{10}C and ^{15}O, whose production and decay are particularly sensitive to nuclear fragmentation modeling and to statistical fluctuations, which are more relevant in the shortest acquisition time window. It should be noted that the analytical model was calibrated on MC simulations performed with the Geant4 toolkit; therefore, any discrepancies between the measured and analytically predicted activity distributions may originate from limitations in the underlying nuclear models implemented in Geant4. This interpretation is consistent with the findings reported in [78, 79], where similar deviations were attributed to the description of light fragment production in Geant4-based calculations. At later time frames (0-600 s and 300-600 s), when the contribution from the longer-lived ^{11}C becomes dominant, the overall agreement improved. In these time frames, the peak and R80 differences were below 2 mm, and the total NRMSE values were around 0.05.

For the 2×2 cm^2 irradiation field configuration, the analytical predictions maintained a similarly high level of agreement with the measured PET data. The longitudinal profiles appear smoother compared to the single spot case, as the larger irradiated area increases the number of voxels contributing along the lateral directions for each depth, effectively improving the signal-to-noise ratio of the integrated depth profile. In contrast, smaller

Unscan - 3 Gy	Measured data	Analytically predicted data	Δ value
0 - 60 s			
Peak depth [mm]	98.50 ± 0.75	93.90 ± 0.75	4.60 ± 1.06
R80 value [mm]	102.66 ± 0.75	101.05 ± 0.75	1.61 ± 1.06
Total NRMSE		0.053	
NRMSE of longitudinal profiles		0.094	
0 - 600 s			
Peak depth [mm]	97.00 ± 0.75	98.50 ± 0.75	-1.50 ± 1.06
R80 value [mm]	103.92 ± 0.75	102.79 ± 0.75	1.13 ± 1.06
Total NRMSE		0.052	
NRMSE of longitudinal profiles		0.067	
300 - 600 s			
Peak depth [mm]	98.50 ± 0.75	98.50 ± 0.75	0.00 ± 1.06
R80 value [mm]	103.86 ± 0.75	103.09 ± 0.75	0.77 ± 1.06
Total NRMSE		0.045	
NRMSE of longitudinal profiles		0.059	

Table 4.2: Peak positions, R80 values, and corresponding shifts (Δ = measured - analytical) for the measured and analytically predicted integrated longitudinal activity profiles in the single spot configuration with a delivered dose of 3 Gy. Positional uncertainties correspond to half the voxel size (1.5 mm / 2 = 0.75 mm). Uncertainties on the differences were obtained by propagation in quadrature (±1.06 mm). Total and longitudinal-profile NRMSE values quantify the overall and depth-wise agreement between measured and analytically predicted distributions. Results are shown for the time frames 0-60 s, 0-600 s, and 300-600 s after the end of irradiation (see Fig. (4.10) (top)).

fields inherently include a higher fraction of background voxels in the lateral integration, which leads to more pronounced statistical fluctuations. The agreement in peak and R80 positions, typically within 1-3 mm, improves progressively across time frames, as the contribution from the longer-lived ^{11}C isotope becomes dominant. These differences are comparable to the estimated spatial uncertainty (±1.06 mm), indicating an overall consistent positional match. The corresponding NRMSE values (0.04-0.10) further confirm that the analytical model reproduces the measured depth profiles within the expected experimental accuracy.

For the 4×4 cm^2 irradiation field configuration, both longitudinal and lateral activity profiles showed reasonable consistency with the measured PET data across all time frames. Slight distal shifts were observed in the measured profiles, with peak position differences ranging from 1.5 to 4.6 mm and R80 differences between 0.6 and 2.3 mm, which are comparable to the estimated spatial uncertainty (±1.06 mm). The largest deviations occurred in the earliest time frame (0-60 s), likely due to the contribution of short-lived isotopes

2x2scan - 3 Gy	Measured data	Analytically predicted data	Δ value
0 - 60 s			
Peak depth [mm]	97.00 ± 0.75	93.90 ± 0.75	3.10 ± 1.06
R80 value [mm]	103.32 ± 0.75	101.06 ± 0.75	2.26 ± 1.06
Total NRMSE		0.085	
NRMSE of longitudinal profiles		0.096	
0 - 600 s			
Peak depth [mm]	100.00 ± 0.75	98.50 ± 0.75	1.50 ± 1.06
R80 value [mm]	103.98 ± 0.75	102.80 ± 0.75	1.18 ± 1.06
Total NRMSE		0.079	
NRMSE of longitudinal profiles		0.066	
300 - 600 s			
Peak depth [mm]	100.00 ± 0.75	98.50 ± 0.75	1.50 ± 1.06
R80 value [mm]	103.99 ± 0.75	103.09 ± 0.75	0.09 ± 1.06
Total NRMSE		0.070	
NRMSE of longitudinal profiles		0.043	

Table 4.3: Peak positions, R80 values, and corresponding shifts (Δ = measured - analytical) for the measured and analytically predicted integrated longitudinal activity profiles in the 2×2 cm^2 irradiation field configuration with a delivered dose of 3 Gy. Positional uncertainties correspond to half the voxel size (1.5 mm / 2 = 0.75 mm). Uncertainties on the differences were obtained by propagation in quadrature (±1.06 mm). Total and longitudinal-profile NRMSE values quantify the overall and depth-wise agreement between measured and analytically predicted distributions. Results are shown for the time frames 0-60 s, 0-600 s, and 300-600 s after the end of irradiation (see Fig. (4.10) (middle)).

(^{10}C and ^{15}O) and statistical fluctuations. The total and longitudinal-profile NRMSE values, ranging from 0.095 to 0.108 and from 0.052 to 0.104, respectively, indicate a generally good agreement between the analytical predictions and the measured data, with improved consistency at later acquisition windows.

A comparison across the three irradiation setups shows that the analytical model reproduces the main features of the measured longitudinal profiles. Differences, particularly in the earliest time frames where short-lived isotopes (^{10}C and ^{15}O) contribute most and in proximal regions, together with the need to apply scaling factors to better match measured PET data, highlight the limitations of the Geant4-based tuning. Residual deviations in peak positions and R80 values remain, typically within ±1.06 mm; while lateral integration smooths the profiles, larger fields can still exhibit noise, indicating that the model is not yet ideal for precise range verification.

Overall, the validation against MC simulations and experimental PET data suggests that the developed analytical framework is a very promising tool for describing PED in both

4x4scan - 3 Gy	Measured data	Analytically predicted data	Δ value
0 - 60 s			
Peak depth [mm]	98.50 ± 0.75	93.90 ± 0.75	4.60 ± 1.06
R80 value [mm]	103.39 ± 0.75	101.09 ± 0.75	2.30 ± 1.06
Total NRMSE		0.108	
NRMSE of longitudinal profiles		0.104	
0 - 600 s			
Peak depth [mm]	100.00 ± 0.75	98.50 ± 0.75	1.50 ± 1.06
R80 value [mm]	103.69 ± 0.75	102.80 ± 0.75	0.89 ± 1.06
Total NRMSE		0.102	
NRMSE of longitudinal profiles		0.074	
300 - 600 s			
Peak depth [mm]	100.00 ± 0.75	98.50 ± 0.75	1.50 ± 1.06
R80 value [mm]	103.73 ± 0.75	103.09 ± 0.75	0.64 ± 1.06
Total NRMSE		0.095	
NRMSE of longitudinal profiles		0.052	

Table 4.4: Peak positions, R80 values, and corresponding shifts (Δ = measured - analytical) for the measured and analytically predicted integrated longitudinal activity profiles in the 4×4 cm^2 irradiation field configuration with a delivered dose of 3 Gy. Positional uncertainties correspond to half the voxel size (1.5 mm / 2 = 0.75 mm). Uncertainties on the differences were obtained by propagation in quadrature (±1.06 mm). Total and longitudinal-profile NRMSE values quantify the overall and depth-wise agreement between measured and analytically predicted distributions. Results are shown for the time frames 0-60 s, 0-600 s, and 300-600 s after the end of irradiation (see Fig. (4.10) (middle)). Results are shown for the time frames 0-60 s, 0-600 s, and 300-600 s after the end of irradiation (see Fig. (4.10) (bottom)).

un-scanned and scanned carbon-ion fields. However, further measurements and additional tuning of the model parameters to real data, rather than solely relying on MC simulations, are necessary to fully establish its accuracy and reliability for precise PET-based range verification.

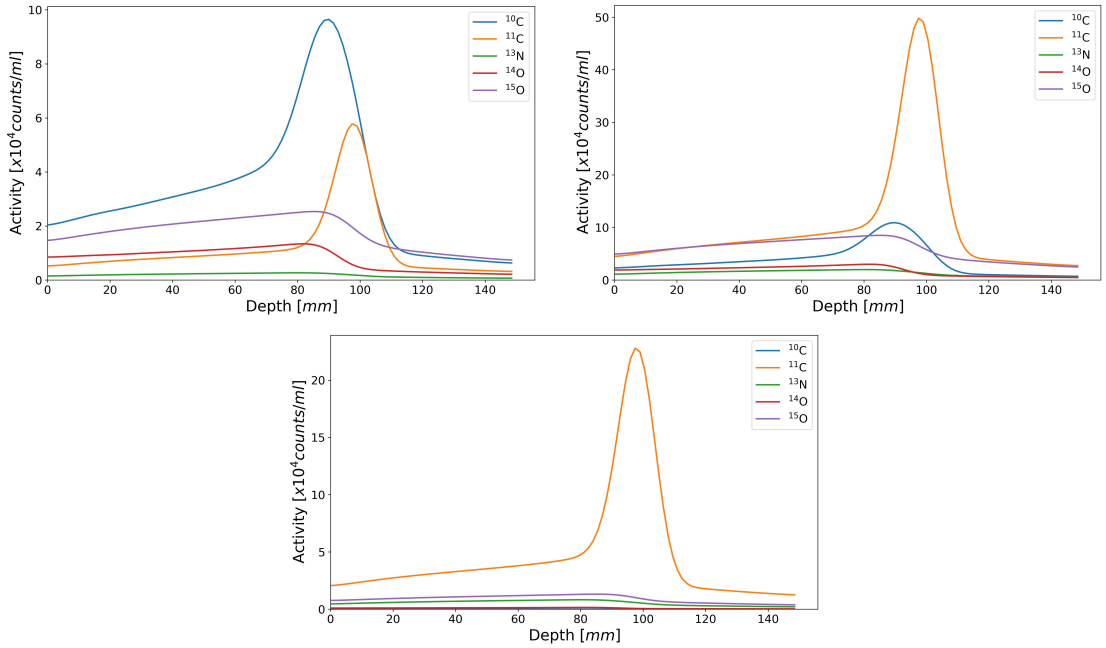

Figure 4.12: Integrated longitudinal activity distributions for the 2×2 cm^2 irradiation field configuration with a delivered dose of 3 Gy, shown separately for each PE. Results are presented for the time frames 0-60 s, 0-600 s, and 300-600 s after the end of irradiation.

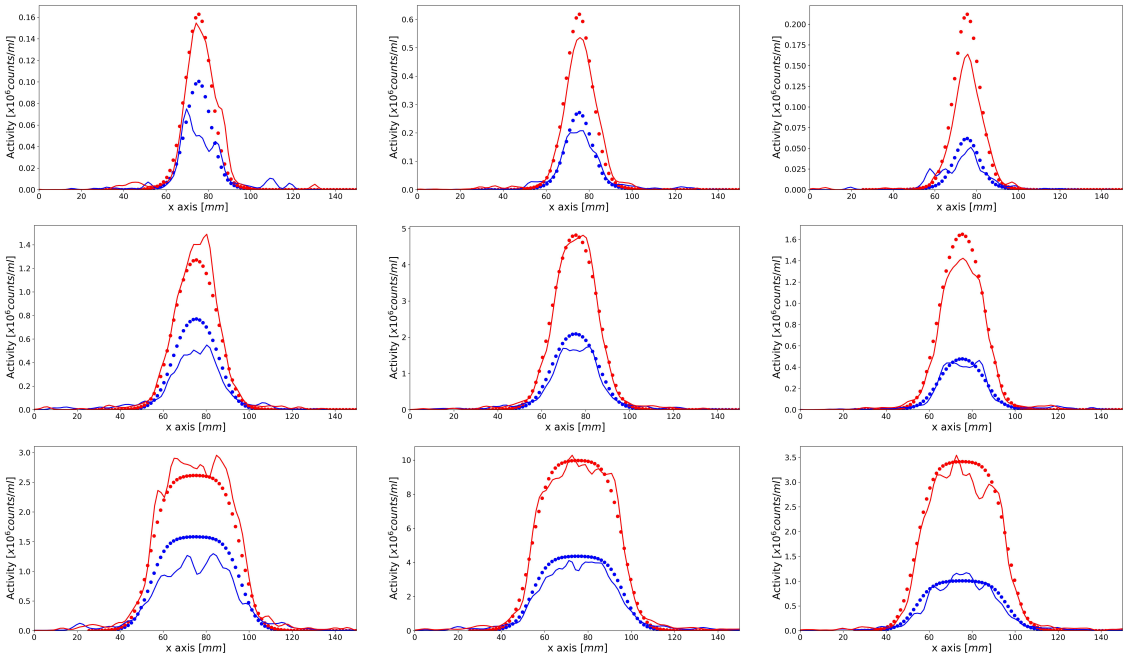

Figure 4.13: Lateral activity profiles at selected depths for the single spot (top), 2×2 cm^2 (middle), and 4×4 cm^2 (bottom) irradiation field configurations, with a delivered dose of 3 Gy. From left to right, the profiles correspond to time frames 0-60 s, 0-600 s, and 300-600 s after the end of irradiation. Blue lines and markers represent measured and analytically predicted activity profiles at z = 75 mm, while red lines and markers correspond to profiles at z = 94.5 mm.

5

Conclusion and Outlook

The validation of the analytical model for predicting three-dimensional PED in CIRT has yielded encouraging results. Although the model was originally developed and validated against MC simulations in previous work [10], this thesis extends its validation by performing a detailed comparison with in-beam PET measurements. This represents a significant advancement, demonstrating that the analytical approach can reliably reproduce activity distributions measured in real in-beam PET scenarios.

For the 200 MeV/n pencil beam irradiation, the analytical model reproduced the MC simulated distributions with high consistency: the peak position matched exactly (70±0.5 mm), while R20 and R80 differed by 0.38±0.01 mm and 0.32±0.01 mm, respectively. The NRMSE was 0.0178, and gamma index passing rates were 99.80% (2%/2 mm) and 98.13% (1%/1 mm), confirming deviations well below 1 mm for range metrics. This consistency test is limited by the fact that the model was tuned on Geant4 simulations.

Comparison with in-beam PET data confirmed the model's ability to capture the main spatial and temporal features of the activity distributions, including the transition from short-lived isotopes (^{10}C, ^{15}O) in the early phase to the predominance of ^{11}C at later times. Deviations in peak position up to ∼1-4.6 mm and minor differences in peak-to-plateau shape were observed, reflecting limitations of the Geant4-based tuning. Empirical scaling corrections were necessary to better reproduce the measured activity, and local discrepancies in intensity and profile shape remain. NRMSE values were generally below 0.1, with occasional cases reaching 0.108, highlighting the need for caution when using the current model for precise range assessment.

The analytical approach demonstrated computational efficiency and the potential for fast,

near real-time predictions of PED and PET activity distributions. While key features, such as the distal fall-off, are reproduced with deviations generally below a few millimeters, local discrepancies above 1 mm indicate that further refinement is required before clinical application. Limitations observed in early time frames point to the need for improved modeling of short-lived PEs yields, and validation so far was restricted to homogeneous PMMA phantoms. Future work should extend the validation to heterogeneous phantoms and patient-specific geometries, and focus on refining the model parameters based on measured data rather than solely on MC simulations.

In conclusion, this thesis demonstrates the application of the analytical framework to a realistic clinical beam model and its validation against experimental in-beam PET data. The model reproduces the main spatial and temporal activity features with deviations generally within a few millimeters, illustrating both its potential and current limitations. This work provides a foundation for further improvements, systematic tuning to experimental data, and future steps toward quantitative, fast analytical predictions for PET-based range verification and adaptive treatment monitoring in CIRT.

A

Longitudinal activity profile for 0-60 s cases without scaling factors

Fig. (A.1) shows the integrated longitudinal profiles of the measured and analytically predicted activity distributions for the single spot, 2×2 cm^2, and 4×4 cm^2 irradiation field configurations, corresponding to the 0-60 s time frame after the end of irradiation. In these cases, the analytically predicted profiles are displayed without applying the scaling factors to ^{10}C and ^{15}O PEs, resulting in a pronounced overestimation in both the plateau and the peak regions.

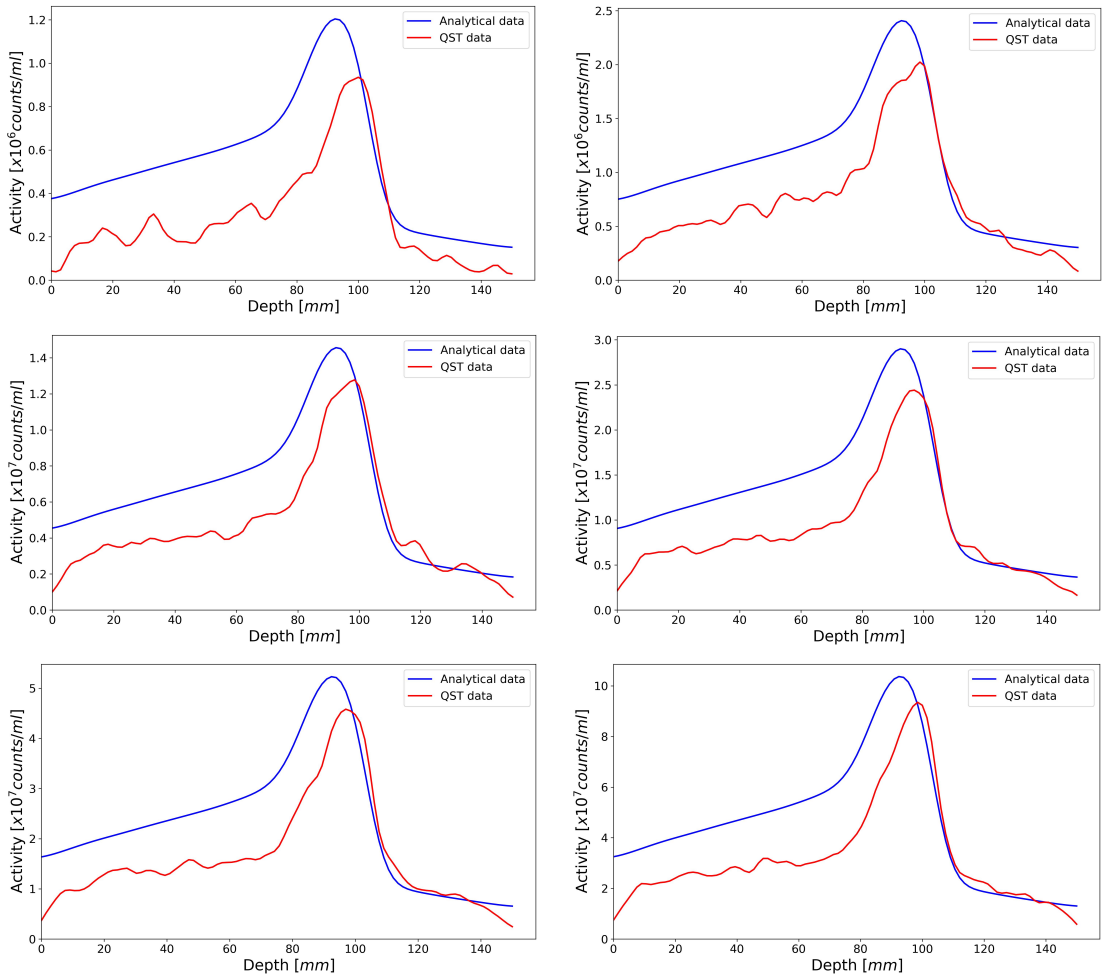

Figure A.1: Integrated longitudinal activity profiles for the single spot (top), 2×2 cm^2 (middle), and 4×4 cm^2 (bottom) irradiation field configurations for the 0-60 s time frame after the end of irradiation. Dose delivered of 1.5 Gy and 3 Gy cases are shown on the left and on the right, respectively. The blue line represents the analytically predicted activity profile without applying the scaling factors, while the red line represents the measured profile.

B

Results for 1.5 Gy delivered dose cases

Figs. (B.1), (B.2), and (B.3) show the 2D measured and the analytically predicted activity distributions on the y-z plane containing the central beam axis for the single spot, 2×2 cm^2, and 4×4 cm^2 irradiation field configurations, respectively, with a delivered dose of 1.5 Gy. The results are presented for the three different time frames after the end of irradiation: 0-60 s, 0-600 s, and 300-600 s. The signal is expressed in counts/ml.

In Fig. (B.4), the integrated longitudinal profiles of the measured and analytically predicted activity distributions are shown for the one single spot, 2×2 cm^2, and 4×4 cm^2 irradiation field configurations, with delivered dose of 1.5 Gy. Tables (B.1), (B.2) and (B.3) report the peak positions and R80 values, as well as the total NRMSE values and the NRMSE values relative to the integrated longitudinal profile for each case.

Fig. (B.5) shows the lateral activity distributions at fixed depths for the single spot, 2×2 cm^2, and 4×4 cm^2 irradiation field configurations, respectively, with delivered dose of 1.5 Gy.

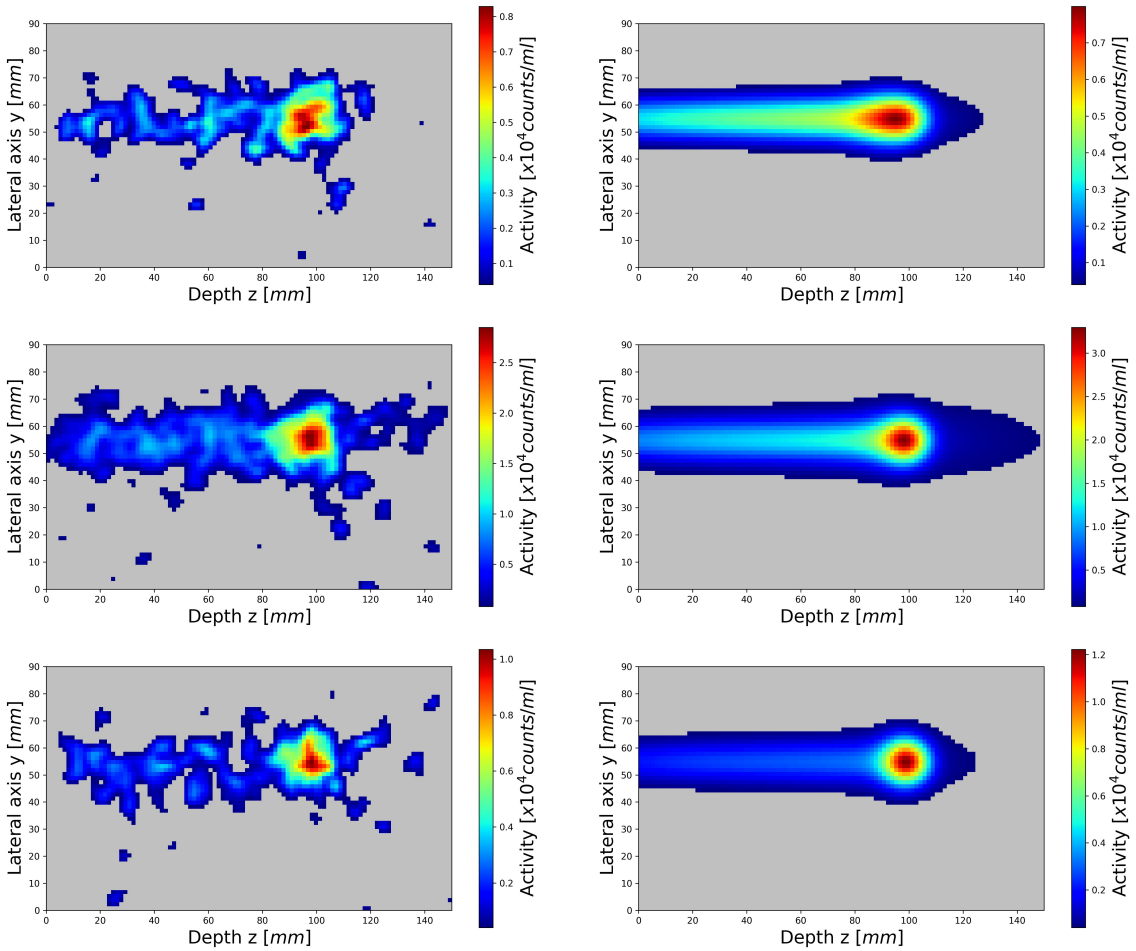

Figure B.1: 2D measured and analytically predicted activity distributions for the single spot configuration with a delivered dose of 1.5 Gy. Results are shown on the y-z plane containing the central beam axis for the three time frames after the end of irradiation: 0-60 s (top), 0-600 s (middle), and 300-600 s (bottom). Measured activity distributions are shown on the left, and analytically predicted distributions are shown on the right. The signal is expressed in counts/ml.

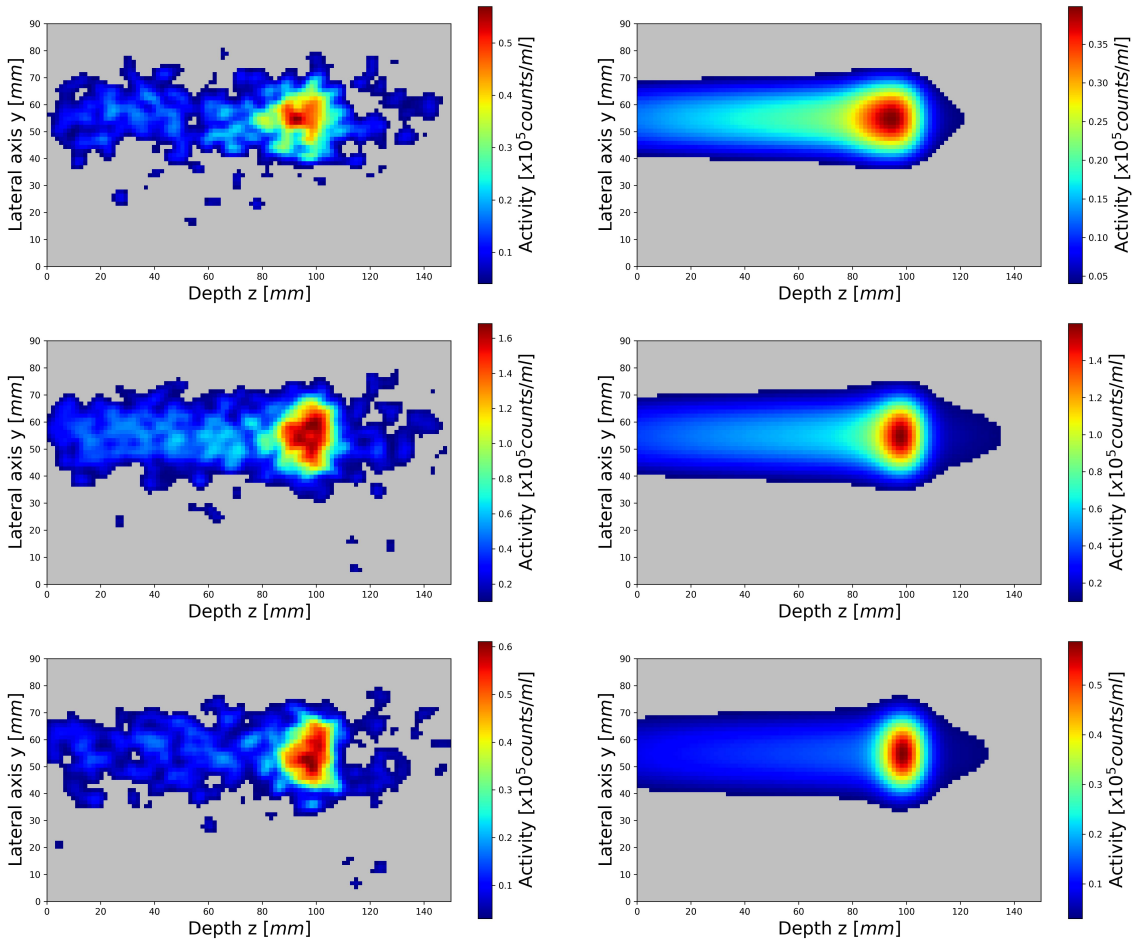

Figure B.2: 2D measured and analytically predicted activity distributions for the 2×2 cm^2 irradiation field configuration with a delivered dose of 1.5 Gy. Results are shown on the y-z plane containing the central beam axis for the three time frames after the end of irradiation: 0-60 s (top), 0-600 s (middle), and 300-600 s (bottom). Measured activity distributions are shown on the left, and analytically predicted distributions are shown on the right. The signal is expressed in counts/ml.

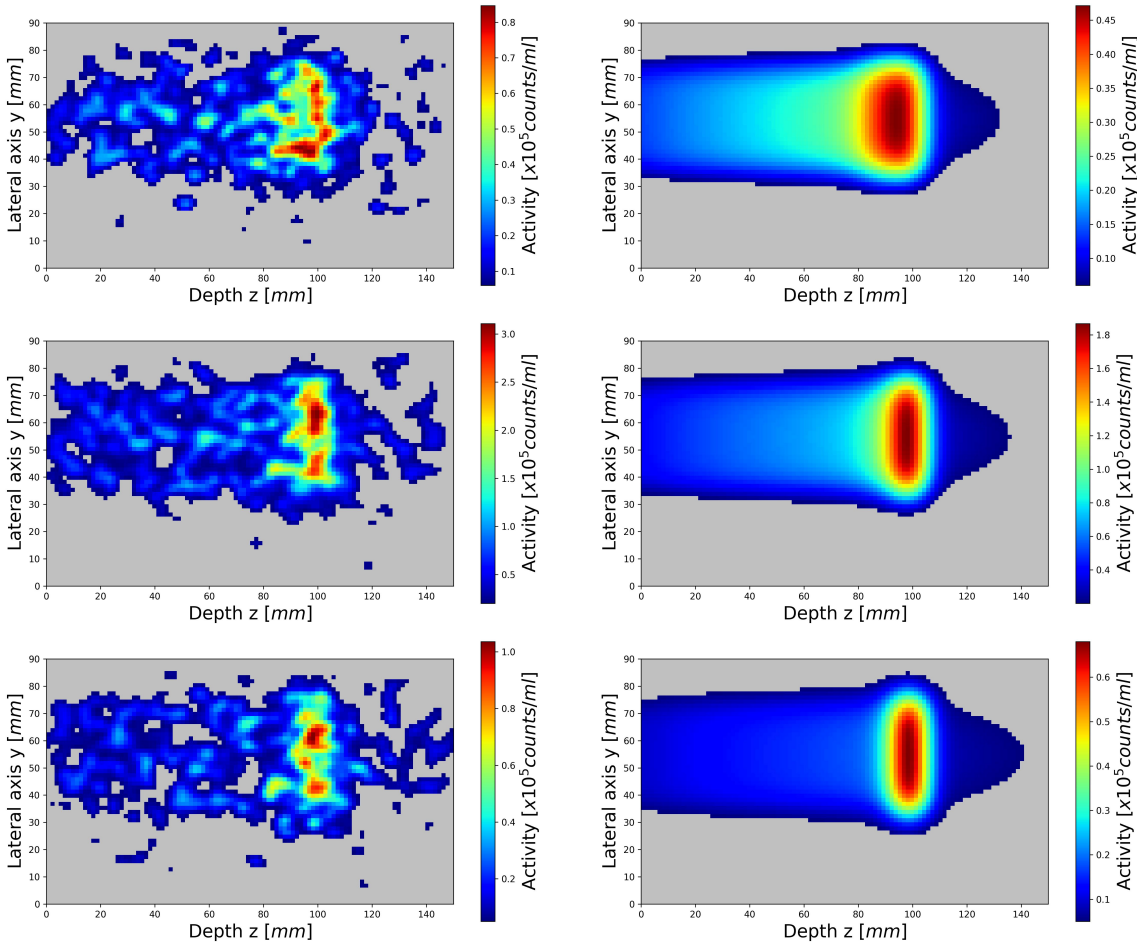

Figure B.3: 2D measured and analytically predicted activity distributions for the 4x4 cm^2 irradiation field configuration with a delivered dose of 1.5 Gy. Results are shown on the y-z plane containing the central beam axis for the three time frames after the end of irradiation: 0-60 s (top), 0-600 s (middle), and 300-600 s (bottom). Measured activity distributions are shown on the left, and analytically predicted distributions are shown on the right. The signal is expressed in counts/ml.

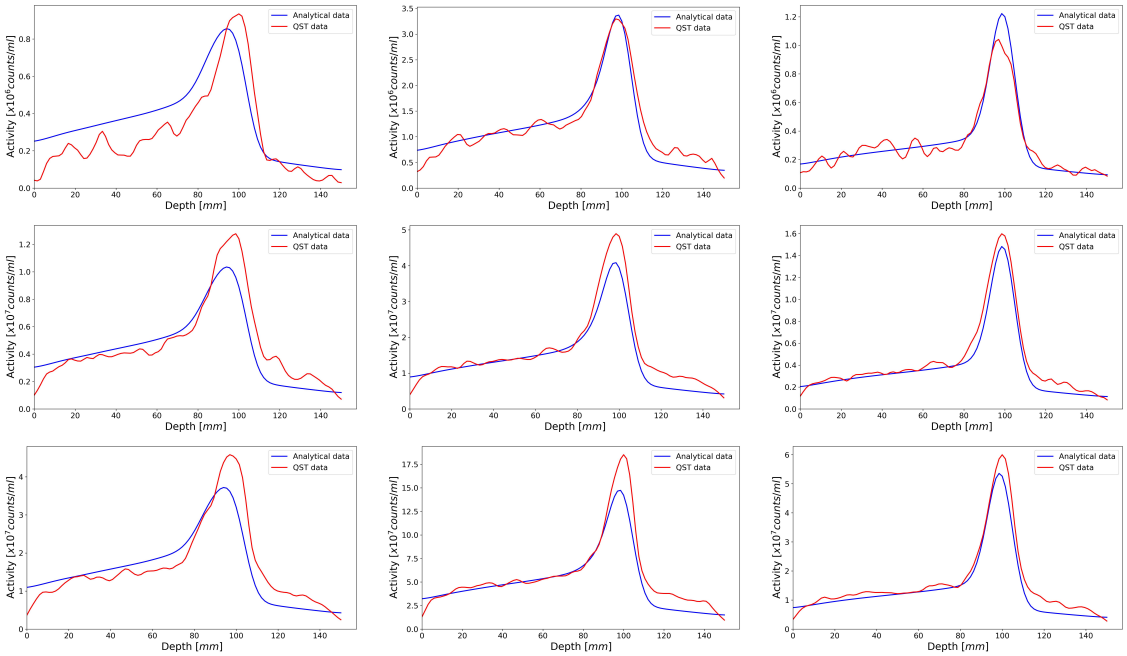

Figure B.4: Integrated longitudinal activity profiles for the single spot (top), 2×2 cm^2 (middle), and 4×4 cm^2 (bottom) irradiation field configurations, with a delivered dose of 1.5 Gy. From left to right, the profiles correspond to time frames 0-60 s, 0-600 s, and 300-600 s after the end of irradiation. The blue line represents the analytically predicted activity profile, while the red line represents the measured profile.

Unscan - 1.5 Gy	**Measured data**	**Analytically predicted data**	**Δ value**
0 - 60 s			
Peak depth [mm]	100.00 ± 0.75	93.90 ± 0.75	6.10 ± 1.06
R80 value [mm]	104.85 ± 0.75	101.05 ± 0.75	3.80 ± 1.06
TotalNRMSE		0.055	
NRMSE of longitudinal profiles		0.150	
0 - 600 s			
Peak depth [mm]	97.00 ± 0.75	98.50 ± 0.75	-1.05 ± 1.06
R80 value [mm]	104.15 ± 0.75	102.79 ± 0.75	1.36 ± 1.06
Total NRMSE		0.054	
NRMSE of longitudinal profiles		0.060	
300 - 600 s			
Peak depth [mm]	97.00 ± 0.75	98.50 ± 0.75	-1.50 ± 1.06
R80 value [mm]	103.47 ± 0.75	103.09 ± 0.75	0.38 ± 1.06
Total NRMSE		0.046	
NRMSE of longitudinal profiles		0.063	

Table B.1: Peak positions, R80 values, and corresponding shifts (Δ = measured - analytical) for the measured and analytically predicted integrated longitudinal activity profiles in the single spot configuration with a delivered dose of 1.5 Gy. Positional uncertainties correspond to half the voxel size (1.5 mm / 2 = 0.75 mm). Uncertainties on the differences were obtained by propagation in quadrature (±1.06 mm). Total and longitudinal-profile NRMSE values quantify the overall and depth-wise agreement between measured and analytically predicted distributions. Results are shown for the time frames 0-60 s, 0-600 s, and 300-600 s after the end of irradiation (see Fig. (B.4) (top)).

2x2scan - 1.5 Gy	Measured data	Analytically predicted data	Δ value
0 - 60 s			
Peak depth [mm]	98.50 ± 0.75	93.90 ± 0.75	4.60 ± 1.06
R80 value [mm]	103.08 ± 0.75	101.06 ± 0.75	2.02 ± 1.06
TotalNRMSE		0.070	
NRMSE of longitudinal profiles		0.103	
0 - 600 s			
Peak depth [mm]	98.50 ± 0.75	98.50 ± 0.75	0.00 ± 1.06
R80 value [mm]	103.36 ± 0.75	102.80 ± 0.75	0.56 ± 1.06
TotalNRMSE		0.081	
NRMSE of longitudinal profiles		0.072	
300 - 600 s			
Peak depth [mm]	98.50 ± 0.75	98.50 ± 0.75	0.00 ± 1.06
R80 value [mm]	103.49 ± 0.75	103.09 ± 0.75	0.40 ± 1.06
TotalNRMSE		0.067	
NRMSE of longitudinal profiles		0.051	

Table B.2: Peak positions, R80 values, and corresponding shifts (Δ = measured - analytical) for the measured and analytically predicted integrated longitudinal activity profiles in the 2×2 cm^2 irradiation field configuration with a delivered dose of 1.5 Gy. Positional uncertainties correspond to half the voxel size (1.5 mm / 2 = 0.75 mm). Uncertainties on the differences were obtained by propagation in quadrature (±1.06 mm). Total and longitudinal-profile NRMSE values quantify the overall and depth-wise agreement between measured and analytically predicted distributions. Results are shown for the time frames 0-60 s, 0-600 s, and 300-600 s after the end of irradiation (see Fig. (B.4) (middle)).

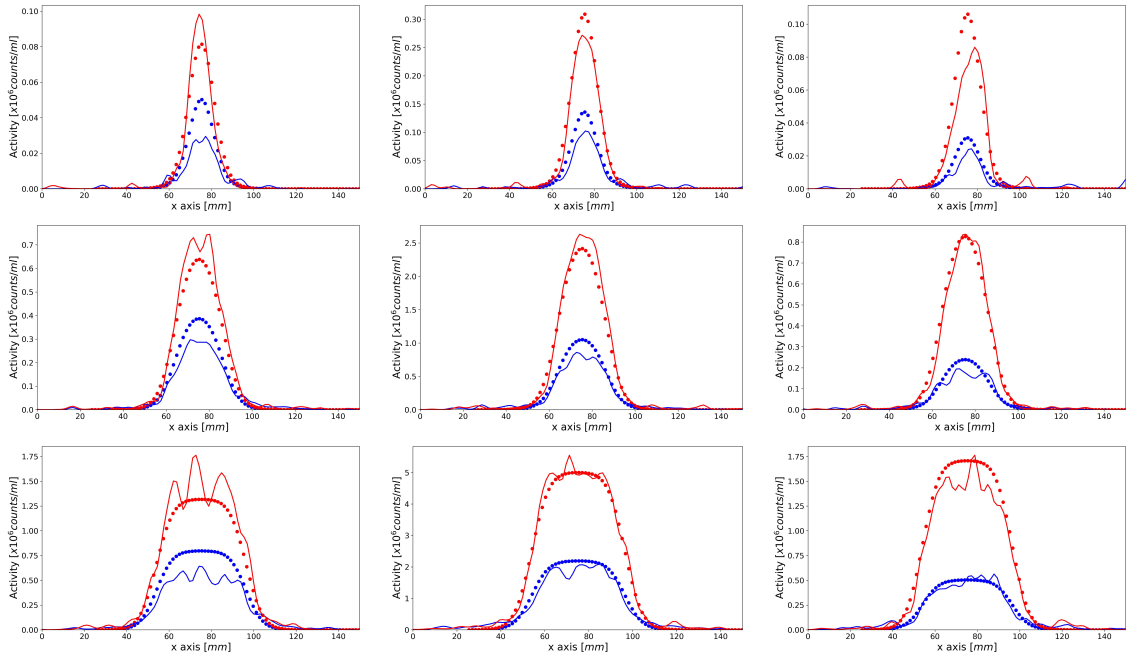

Figure B.5: Lateral activity profiles at selected depths for the single spot (top), 2×2 cm^2 (middle), and 4×4 cm^2 (bottom) irradiation field configurations, with a delivered dose of 1.5 Gy. From left to right, the profiles correspond to time frames 0-60 s, 0-600 s, and 300-600 s after the end of irradiation. Blue lines and markers represent measured and analytically predicted activity profiles at z = 75 mm, while red lines and markers correspond to profiles at z = 94.5 mm.

4x4scan - 1.5 Gy	Measured data	Analytically predicted data	Δ value
0 - 60 s			
Peak depth [mm]	97.00 ± 0.75	93.90 ± 0.75	3.10 ± 1.06
R80 value [mm]	103.86 ± 0.75	101.07 ± 0.75	2.79 ± 1.06
Total NRMSE		0.099	
NRMSE of longitudinal profiles		0.105	
0 - 600 s			
Peak depth [mm]	100.00 ± 0.75	98.50 ± 0.75	1.50 ± 1.06
R80 value [mm]	103.87 ± 0.75	102.80 ± 0.75	1.07 ± 1.06
Total NRMSE		0.097	
NRMSE of longitudinal profiles		0.075	
300 - 600 s			
Peak depth [mm]	100.00 ± 0.75	98.50 ± 0.75	1.50 ± 1.06
R80 value [mm]	104.01 ± 0.75	103.09 ± 0.75	0.92 ± 1.06
Total NRMSE		0.091	
NRMSE of longitudinal profiles		0.052	

Table B.3: Peak positions, R80 values, and corresponding shifts (Δ = measured - analytical) for the measured and analytically predicted integrated longitudinal activity profiles in the 4×4 cm^2 irradiation field configuration with a delivered dose of 1.5 Gy. Positional uncertainties correspond to half the voxel size (1.5 mm / 2 = 0.75 mm). Uncertainties on the differences were obtained by propagation in quadrature (±1.06 mm). Total and longitudinal-profile NRMSE values quantify the overall and depth-wise agreement between measured and analytically predicted distributions. Results are shown for the time frames 0-60 s, 0-600 s, and 300-600 s after the end of irradiation (see Fig. (B.4) (bottom)).

Bibliography

[1] F. Bray, M. Laversanne, H. Sung, J. Ferlay, R. L. Siegel, I. Soerjomataram, and A. Jemal. Global cancer statistics 2022: GLOBOCAN estimates of incidence and mortality worldwide for 36 cancers in 185 countries. *CA: A Cancer Journal for Clinicians*, 2024.

[2] A. Zafar, S. Khatoon, M. J. Khan, J. Abu, and A. Naeem. Advancements and limitations in traditional anti-cancer therapies: a comprehensive review of surgery, chemotherapy, radiation therapy, and hormonal therapy. *Discover Oncology*, 2025.

[3] A. Pompos, M. Durante, and H. Choy. Heavy Ions in Cancer Therapy. *Jama Oncol*, 2016.

[4] E. J. Hall and A. J. Giaccia. *Radiobiology for the Radiologist*. 8th ed. Wolters Kluwer, 2018.

[5] X. Wang, X. Chen, G. Li, X. Han, T. Gao, W. Liu, and X. Tang. Application of Carbon Ion and Its Sensitizing Agent in Cancer Therapy: A Systematic Review. *Frontiers in Oncology*, 2021.

[6] K. Parodi, F. Pönisch, and W. Enghardt. Experimental study on the feasibility of in-beam PET for accurate monitoring of proton therapy. *IEEE Transactions on Nuclear Science*, 2005.

[7] K. Parodi, H. Paganetti, H. A. Shih, S. Michaud, J. S. Loeffler, T. F. DeLaney, N. J. Liebsch, J. E. Munzenrider, A. J. Fischman, A. Knopf, and T. Bortfeld. Patient study of in vivo verification of beam delivery and range, using positron emission tomography and computed tomography imaging after proton therapy. *International Journal of Radiation Oncology Biology Physics*, 2007.

[8] A. C. Kraan. Range Verification Methods in Particle Therapy: Underlying Physics and Monte Carlo Modeling. *Frontiers in Oncology*, 2015.

[9] W. Enghardt, P. Crespo, F. Fiedler, R. Hinz, K. Parodi, J. Pawelke, and F. Pönisch. Charged hadron tumor therapy monitoring by means of PET. *Nuclear Instruments and Methods in Physics Research Section A: Accelerators, Spectrometers, Detectors and Associated Equipment*, 2004.

[10] T. Du, J. Bauer, K. Parodi, and M. Pinto. An analytical approach to predict 3D positron emitter distribution in carbon ion therapy. *Physics in Medicine & Biology*, 2025.

[11] T. Hofmann, A. Fochi, K. Parodi, and M. Pinto. Prediction of positron emitter distributions for range monitoring in carbon ion therapy: an analytical approach. *Physics in Medicine & Biology*, 2019.

[12] F. H. Attix. *Introduction to Radiological Physics and Radiation Dosimetry*. John Wiley & Sons, 1986.

[13] E. B. Podgoršak. *Radiation Physics for Medical Physics*. 2nd ed. Springer, 2010.

[14] G. F. Knoll. *Radiation Detection and Measurement*. 3rd ed. John Wiley & Sons, 2000.

[15] W. R. Leo. *Techniques for Nuclear and Particle Physics Experiment*. Springer-Verlag, 1987.

[16] N. Bohr. On the theory of the decrease of velocity of moving electrified particles on passing through matter. *The London, Edinburgh, and Dublin Philosophical Magazine and Journal of Science*, 1913.

[17] H. A. Bethe. Zur Theorie des Durchgangs schneller Korpuskularstrahlen durch Materie. *Annalen der Physik*, 1930.

[18] F. Bloch. Zur Bremsung rasch bewegter Teilchen beim Durchgang durch materie. *Annalen der Physik*, 1933.

[19] R. L. Workman and Particle Data Group. Passage of Particles Through Matter. *Progress of Theoretical and Experimental Physics*, 2022. Review of Particle Physics.

[20] G. Kraft. Tumor therapy with heavy charged particles. *Progress in Particle and Nuclear Physics*, 2000.

[21] M. Durante and J. S. Loeffler. Charged particles in radiation oncology. *Nature Reviews Clinical Oncology*, 2010.

[22] K. Parodi, W. Enghardt, and T. Haberer. In-beam PET measurements of β^+ radioactivity induced by proton beams. *Physics in Medicine & Biology*, 2002.

[23] F. Pönisch, K. Parodi, B. G. Hasch, and W. Enghardt. The modelling of positron emitter production and PET imaging during carbon ion therapy. *Physics in Medicine & Biology*, 2004.

[24] T. D. Malouff, A. Mahajan, S. Krishnan, C. Beltran, D. S. Seneviratne, and D. M. Trifiletti. Carbon Ion Therapy: A Modern Review of an Emerging Technology. *Frontiers in Oncology*, 2020.

[25] G. Friedlander, J. W. Kennedy, E. S. Macias, and J. M Miller. *Nuclear and Radiochemistry*. 3rd ed. John Wiley & Sons, 1981.

[26] R. R. Wilson. Radiological use of fast protons. *Radiology*, 1946.

[27] Particle Therapy Co-Operative Group (PTCOG). Particle therapy facilities in clinical operation, 2025. URL `https://www.ptcog.site/index.php/facilities-in-operation-public`.

[28] T. Kamada, H. Tsujii, E. A. Blakely, J. Debus, W. De Neve, M. Durante, O. Jäkel, R. Mayer, R. Orecchia, R. Pötter, S. Vatnitsky, and W. T. Chu. Carbon ion radiotherapy in Japan: an assessment of 20 years of clinical experience. *The Lancet Oncology*, 2015.

[29] A. A. Lazar, R. Schulte, B. Faddegon, E. A. Blakely, and M. Roach. Clinical trials involving carbon-ion radiation therapy and the path forward. *Cancer*, 2018.

[30] O. Mohamad, B. J. Sishc, J. Saha, A. Pompos, A. Rahimi, M. D. Story, A. J. Davis, and D. W. N. Kim. Carbon Ion Radiotherapy: A Review of Clinical Experiences and Preclinical Research, with an Emphasis on DNA Damage/Repair. *Cancers (Basel)*, 2017.

[31] H. Tsujii, T. Kamada, K. Noda, H. Tsuji, and K. Karasawa. *Carbon-Ion Radiotherapy: Principles, Practices, and Treatment Planning*. Springer, 2014.

[32] F. Koosha, M. Ahmadikamalabadi, and M. Mohammadi. Review of Recent Improvements in Carbon Ion Radiation Therapy in the Treatment of Glioblastoma. *Advances in Radiation Oncology*, 2024.

[33] O. Sokol and M. Durante. Carbon Ions for Hypoxic Tumors: Are We Making the Most of Them? *Cancers (Basel)*, 2023.

[34] H. Tsujii. Overview of Carbon-ion Radiotherapy. *Journal of Physics: Conference Series*, 2017.

[35] T. Kanai. Radiation Therapy Using High-Energy Carbon Beams. In V. Shevelko and H. Tawara, editors, *Atomic Processes in Basic and Applied Physics*, Springer Series on Atomic, Optical, and Plasma Physics. Springer, 2012.

[36] D. Schulz-Ertner and H. Tsujii. Particle radiation therapy using proton and heavier ion beams. *Journal of Clinical Oncology*, 2007.

[37] T. Haberer, J. Debus, O. Jäkel, D. Schulz-Ertner, and U. Weber. The Heidelberg Ion Therapy Center. *Radiotherapy and Oncology*, 2004.

[38] W H. Sweet and G. L. Brownell. Localization of intracranial lesions by scanning with positron-emitting arsenic. *Journal of the American Medical Association*, 1955.

[39] N. B. Smith and A. Webb. *Introduction to Medical Imaging: Physics, Engineering and Clinical Applications*. Cambridge University Press, 2010.

[40] J. Arbizu, S. Morbelli, S. Minoshima, H. Barthel, P. Kuo, D. Van Weehaeghe, N. Horner, P. M. Colletti, and E. Guedj. SNMMI Procedure Standard/EANM Practice Guideline for Brain [^{18}F]FDG PET Imaging, Version 2.0. *Journal of Nuclear Medicine*, 2025.

[41] P. J. Allisy-Roberts and J. Williams. *Farr's Physics for Medical Imaging*. 2nd ed. Elsevier Health Sciences, 2008.

[42] M. A. Flower, editor. *Webb's Physics of Medical Imaging*. 2nd ed. CRC Press, 2012.

[43] T. Masuda, T. Nishio, J. Kataoka, M. Arimoto, A. Sano, and K. Karasawa. ML-EM algorithm for dose estimation using PET in proton therapy. *Physics in Medicine & Biology*, 2019.

[44] T. Masuda, T. Nishio, A. Sano, and K. Karasawa. Extension of the ML-EM algorithm for dose estimation using PET in proton therapy: application to an inhomogeneous target. *Physics in Medicine & Biology*, 2020.

[45] H. M. Hudson and R. S. Larkin. Accelerated image reconstruction using ordered subsets of projection data. *IEEE Transactions on Medical Imaging*, 1994.

[46] A. C. Knopf and A. Lomax. In vivo proton range verification: a review. *Physics in Medicine & Biology*, 2013.

[47] W. Enghardt, W. D. Fromm, H. Geissel, H. Heller, G. Kraft, A. Magel, P. Manfrass, G. Münzenberg, F. Nickel, J. Pawelke, D. Schardt, C. Scheidenberger, and M Sobiella. The spatial distribution of positron-emitting nuclei generated by relativistic light ion beams in organic matter. *Physics in Medicine & Biology*, 1992.

[48] K. Parodi. *Nuclear Medicine Review*, 2012.

[49] E. Fiorina, V. Ferrero, F. Pennazio, G. Baroni, G. Battistoni, N. Belcari, P. Cerello, N. Camarlinghi, M. Ciocca, and A. Del Guerra et al. Monte Carlo simulation tool for online treatment monitoring in hadrontherapy with in-beam PET: A patient study. *Physica Medica*, 2018.

[50] K. McNamara, A. Schiavi, D. Borys, K. Brzezinski, J. Gajewski, R. Kopeć, A. Rucinski, T. Skóra, S. Makkar, J. Hrbacek, D. C. Weber, A. J. Lomax, and C. Winterhalter. GPU accelerated Monte Carlo scoring of positron emitting isotopes produced during proton therapy for PET verification. *Physics in Medicine & Biology*, 2022.

[51] D. Borys, J. Baran, K. Brzeziński, J. Gajewski, N. Chug, A. Coussat, E. Czerwiński, M. Dadgar, K. Dulski, and K. V. Eliyan et al. ProTheRaMon-a GATE simulation framework for proton therapy range monitoring using PET imaging. *Physics in Medicine & Biology*, 2022.

[52] C. Paganelli, C. Gianoli, and A. Knopf. *Imaging in Particle Therapy: Current practice*

and future trends. Biophysical Society-IOP Series. Institute of Physics Publishing, 2024.

[53] E. Yoshida, H. Tashima, T. Shinaji, K. Shimizu, H. Wakizaka, A. Mohammadi, F. Nishikido, and T. Yamaya. Development of a Whole-Body Dual Ring OpenPET for in-Beam PET. *IEEE Transactions on Radiation and Plasma Medical Sciences*, 2017.

[54] A. Mohammadi, H. Tashima, Y. Iwao, S. Takyu, G. Akamatsu, F. Nishikido, E. Yoshida, A. Kitagawa, K. Parodi, and T. Yamaya. Range verification of radioactive ion beams of ^{11}C and ^{15}O using in-beam PET imaging. *Physics in Medicine & Biology*, 2019.

[55] N. Camarlinghi, G. Sportelli, G. Battistoni, N. Belcari, M. Cecchetti, G. A. P. Cirrone, G. Cuttone, S. Ferretti, A. Kraan, A. Retico, F. Romano, P. Sala, K. Straub, A. Tramontana, A. Del Guerra, and V. Rosso. An in-beam PET system for monitoring ion-beam therapy: test on phantoms using clinical 62 MeV protons. *Journal of Instrumentation*, 2014.

[56] H. Tashima, E. Yoshida, N. Inadama, F. Nishikido, Y. Nakajima, H. Wakizaka, T. Shinaji, M. Nitta, S. Kinouchi, M. Suga, H. Haneishi, T. Inaniwa, and T. Yamaya. Development of a small single-ring OpenPET prototype with a novel transformable architecture. *Physics in Medicine & Biology*, 2016.

[57] H. Tashima, E. Yoshida, Y. Iwao, H. Wakizaka, A. Mohammadi, M. Nitta, A. Kitagawa, T. Inaniwa, F. Nishikido, A. B. Tsuji, Y. Nagai, C. Seki, T. Minamimoto, Y. Fujibayashi, and T. Yamaya. Development of a Multiuse Human-Scale Single-Ring OpenPET System. *IEEE Transactions on Radiation and Plasma Medical Sciences*, 2021.

[58] H. Tashima, T. Yamaya, E. Yoshida, S. Kinouchi, M. Watanabe, and E. Tanaka. A single-ring OpenPET enabling PET imaging during radiotherapy. *Physics in Medicine & Biology*, 2012.

[59] T. Yamaya. OpenPET: a novel open-type PET system for 3D dose verification in particle therapy. *Journal of Physics: Conference Series*, 2017.

[60] R. Y. Rubinstein and D. P. Kroese. *Simulation and the Monte Carlo Method*. 3rd ed. John Wiley & Sons, 2016.

[61] S. Agostinelli, J. Allison, K. A. Amako, J. Apostolakis, H. Araujo, P. Arce, M. Asai, D. Axen, S. Banerjee, and G. Barrand et al. Geant4-a simulation toolkit. *Nuclear Instruments and Methods in Physics Research Section A: Accelerators, Spectrometers, Detectors and Associated Equipment*, 2003.

[62] G. Battistoni, J. Bauer, T. T. Boehlen, F. Cerutti, M. P. W. Chin, R. Dos Santos Augusto, A. Ferrari, P. G. Ortega, W. Kozłowska, G. Magro, A. Mairani, K. Parodi, P. R. Sala, P. Schoofs, T. Tessonnier, and V. Vlachoudis. The FLUKA Code: An Accurate Simulation Tool for Particle Therapy. *Frontiers in Oncology*, 2016.

[63] A. J. Kulesza, R. T. Adams, J. S. Bull, T. Goorley, H. G. Hughes, R. L. Martz, M. E. Rising, A. R. Schake, and A. J. Zukaitis. MCNP® code version 6.3.0 theory & user manual. Technical report, Los Alamos National Laboratory, 2022.

[64] K. Parodi, A. Ferrari, F. Sommerer, and H. Paganetti. Clinical CT-based calculations of dose and positron emitter distributions in proton therapy using the FLUKA Monte Carlo code. *Physics in Medicine & Biology*, 2007.

[65] F. Pennazio, G. Battistoni, M. G. Bisogni, N. Camarlinghi, A. Ferrari, V. Ferrero, E. Fiorina, M Morrocchi, P. Sala, G. Sportelli, R. Wheadon, and P. Cerello. Carbon ions beam therapy monitoring with the INSIDE in-beam PET. *Physics in Medicine & Biology*, 2018.

[66] K. Parodi, T. Bortfeld, and T. Haberer. Comparison between in-beam and offline positron emission tomography imaging of proton and carbon ion therapeutic irradiation at synchrotron- and cyclotron-based facilities. *International Journal of Radiation Oncology, Biology, Physics*, 2008.

[67] J. Bauer, D. Unholtz, F. Sommerer, C. Kurz, T. Haberer, K. Herfarth, T. Welzel, S. E. Combs, J. Debus, and K. Parodi. Implementation and initial clinical experience of offline PET/CT-based verification of scanned carbon ion treatment. *Radiotherapy and Oncology*, 2013.

[68] A. Schiavi, M. Senzacqua, S. Pioli, A. Mairani, G. Magro, S. Molinelli, M. Ciocca, G. Battistoni, and V. Patera. Fred: a GPU-accelerated fast-Monte Carlo code for rapid treatment plan recalculation in ion beam therapy. *Physics in Medicine & Biology*, 2017.

[69] K. Choi, S. B. Mein, B. Kopp, G. Magro, S. Molinelli, M. Ciocca, and A. Mairani. FRoG-A New Calculation Engine for Clinical Investigations with Proton and Carbon Ion Beams at CNAO. *Cancers (Basel)*, 2018.

[70] P. Lysakovski, B. Kopp, T. Tessonnier, S. Mein, A. Ferrari, T. Haberer, J. Debus, and A. Mairani. Development and validation of MonteRay, a fast Monte Carlo dose engine for carbon ion beam radiotherapy. *Medical Physics*, 2024.

[71] M. Priegnitz, F. Fiedler, D. Kunath, K. Laube, and W. Enghardt. An Experiment-Based Approach for Predicting Positron Emitter Distributions Produced During Therapeutic Ion Irradiation. *IEEE Transactions on Nuclear Science*, 2012.

[72] S. Helmbrecht, M. Priegnitz, W. Enghardt, H. Rohling, and F. Fiedler. Application of a Yield Approach for the Prediction of Positron Emitter Distributions Produced During Therapeutic Carbon-Ion Beam Irradiation. *IEEE Transactions on Nuclear Science*, 2016.

[73] K. Parodi and T. Bortfeld. A filtering approach based on Gaussian-powerlaw convolutions for local PET verification of proton radiotherapy. *Physics in Medicine & Biology*, 2006.

[74] V. Vasic, K. Parodi, and M. Pinto. Evaluating an analytical prediction algorithm of positron emitter distributions in patient data for PET monitoring of carbon ion therapy: A simulation study. *Applied Radiation and Isotopes*, 2024.

[75] M. Soukup, M. Fippel, and M. Alber. A pencil beam algorithm for intensity modulated proton therapy derived from Monte Carlo simulations. *Physics in Medicine & Biology*, 2005.

[76] B. Schaffner, E. Pedroni, and A. Lomax. Dose calculation models for proton treatment planning using a dynamic beam delivery system: an attempt to include density

heterogeneity effects in the analytical dose calculation. *Physics in Medicine & Biology*, 1999.

[77] M. Siggel, P. Ziegenhein, S. Nill, and U. Oelfke. Boosting runtime-performance of photon pencil beam algorithms for radiotherapy treatment planning. *Physics in Medicine & Biology*, 2012.

[78] A. Chacon, S. Guatelli, H. Rutherford, D. Bolst, A. Mohammadi, A. Ahmed, M. Nitta, F. Nishikido, Y. Iwao, H. Tashima, E. Yoshida, G. Akamatsu, S. Takyu, A. Kitagawa, T. Hofmann, M. Pinto, D. R. Franklin, K. Parodi, T. Yamaya, A. Rosenfeld, and M. Safavi-Naein. Comparative study of alternative Geant4 hadronic ion inelastic physics models for prediction of positron-emitting radionuclide production in carbon and oxygen ion therapy. *Physics in Medicine & Biology*, 2019.

[79] A. Chacon, H. Rutherford, A. Hamato, M. Nitta, F. Nishikido, Y. Iwao, H. Tashima, E. Yoshida, G. Akamatsu, S. Takyu, H. G. Kang, D. R. Franklin, K. Parodi, T. Yamaya, A. Rosenfeld, S. Guatelli, and M. Safavi-Naeini. A quantitative assessment of Geant4 for predicting the yield and distribution of positron-emitting fragments in ion beam therapy. *Physics in Medicine & Biology*, 2024.

[80] K. Parodi, A. Mairani, and F. Sommerer. Monte Carlo-based parametrization of the lateral dose spread for clinical treatment planning of scanned proton and carbon ion beams. *Journal of Radiation Research*, 2013.

[81] F. Attanasi, A. Knopf, K. Parodi, H.Paganetti, T. Bortfeld, V. Rosso, and A. Del Guerra. Extension and validation of an analytical model for in vivo PET verification of proton therapy-a phantom and clinical study. *Physics in Medicine & Biology*, 2011.

[82] International Atomic Energy Agency (IAEA), Nuclear Data Services. Livechart-table of nuclides, 2025. URL `https://www-nds.iaea.org/relnsd/vcharthtml/VChartHTML.html`.

[83] S. Tanaka, T. Inaniwa, and S. Matsuba. Development of ripple filter composed of metal mesh for charged-particle therapy. *Physics in Medicine & Biology*, 2022.